

DISSERTATION

ENERGY STORAGE IMPROVEMENT THROUGH MATERIAL SCIENCE APPROACHES

Submitted by

Brandon Joseph Kelly

Department of Mechanical Engineering

In partial fulfillment of the requirements

For the Degree of Doctor of Philosophy

Colorado State University

Fort Collins, Colorado

Fall 2013

Doctoral Committee:

Advisor: Amy Prieto

Allan Kirkpatrick

Suren Chen

Prasad Dasi

ABSTRACT

ENERGY STORAGE IMPROVEMENT THROUGH MATERIAL SCIENCE APPROACHES

A need for improved energy storage is apparent for the improvement of our society. Lithium ion batteries are one of the leading energy storage technologies being researched today. These batteries typically utilize coupled reduction/oxidation reactions with intercalation reactions in crystalline metal oxides with lithium ions as charge carriers to produce efficient and high power energy storage options. The cathode material (positive electrode) has been an emphasis in the recent research as it is currently the weakest link of the battery. Several systems of cathode materials have been studied with different structures and chemical makeup, all having advantages and disadvantages. One focus of the research presented below was creating a low cost and high performance cathode material by creating a composite of the low cost spinel structured LiMn_2O_4 and the higher capacity layered structure materials. Two compositional diagrams were used to map out the composition space between end members which include two dimensional layer structured LiCoO_2 , LiNiO_2 , $\text{LiNi}_{0.8}\text{Co}_{0.2}\text{O}_2$ and three dimensional spinel structured LiMn_2O_4 . Several compositions in each composition map were electrochemically tested and structurally characterized in an attempt to discover a high performance cathode material with a lower cost precursor. The best performing composition in each system shows the desired mixed phase of the layered and spinel crystal structures, yielding improved performance versus the individual end member components. The surrounding compositions were then tested in order to find the optimum composition and performance. The best performing composition was $0.2\text{LiCoO}_2 \cdot 0.7\text{LiNi}_{0.8}\text{Co}_{0.2}\text{O}_2 \cdot 0.1\text{LiMn}_2\text{O}_4$ and yielded a specific capacity of 182mAh/g.

Another promising area of chemical energy storage is in the storage of hydrogen gas in chemical hydrides. Hydrogen gas can be used as a fuel in a variety of applications as a viable method for storing and transporting energy. Currently, the storage of the hydrogen is one of the major obstacles to its use as a fuel, and is traditionally done in high pressure cylinders or cryogenic storage tanks. Chemical hydrides allow storage of hydrogen in a solid form with higher volumetric hydrogen storage density than both traditional options. These chemical hydrides however are not performing close to their theoretical values and need further improvement in order to be viable in mobile applications. In this study two complex chemical hydride materials (Li_3AlH_6 and $\text{LiNa}_2\text{AlH}_6$) with high theoretical storage values were studied and doped with catalysts in an attempt to increase the hydrogen yield. The successful improvement of both Li_3AlH_6 and $\text{LiNa}_2\text{AlH}_6$ with 2% LaCl_3 catalyst was achieved improving the chemical hydrogen yield percent by 4.6% and 22.9% respectively.

ACKNOWLEDGEMENTS

It was only through the patience and support of many people that I have am able to finally reach the end of this degree. First I would like to thank my wife, Evin Kelly who is the only person who has seen the deepest lows and highest highs, and stood by me the entire way. My advisor Dr. Amy Prieto is one of the kindest people I have ever met, and welcomed me into her lab without hesitation as my previous lab dissolved. I really cannot express how grateful I am to her for her patience, guidance, and effort in helping me finish. I would also like to mention Dr. Sue James and Dr. Allan Kirkpatrick, who were there to listen to my concerns when my old lab was falling apart. They were instrumental in helping me transition to my new advisor and lab, and helped me through a very trying time. Thanks also to my other committee members Dr. Chen and Dr. Dasi for their patience. My lab mates old and new were great. I would like to mention specifically Madhu Channabasappa, who has been a great help in my work even after he moved to France! Finally, I would like to thank my family, who always kept the faith in me that I would be able to finish even when it didn't look very likely.

TABLE OF CONTENTS

ABSTRACT.....	ii
ACKNOWLEDGEMENTS.....	iv
LIST OF FIGURES.....	viii
Chapter 1: Introduction.....	1
Chapter 2: Lithium-ion Batteries Background, Literature Survey, and Methods.....	3
2.1 Purpose and Aim of Research.....	3
2.2 Lithium Ion Battery Introduction.....	3
2.2.1 Definitions.....	3
2.2.2 Design Considerations.....	6
2.2.3 Evolution of the Lithium Ion Battery.....	8
2.2.4 Cell Configuration.....	13
2.2.5 Recent Developments.....	17
2.2.6 Relevant Material Research Survey.....	20
2.3 Experimental Methods.....	34
2.3.1 Material Synthesis.....	34
2.3.2 Material Characterization.....	36
2.3.3 Lithium Ion Battery Processing and Testing.....	37
2.3.4 Electrochemical Testing.....	41

Chapter 3: Lithium Ion Battery Research	42
3.1 Lithium ion Battery Research Approach.....	42
3.2 Results/Discussion	47
3.2.1 Electrochemical	48
3.2.2 XRD Characterization	56
3.2.3 XPS Characterization	63
3.3 Lithium Ion Battery Summary	65
Chapter 4: Hydrogen Storage Materials Background and Research	66
4.1 Purpose and Aim of Research	66
4.2 Hydrogen Introduction	67
4.2.1 Definitions	67
4.2.2 Design Considerations.....	67
4.2.3 Current Storage Systems	68
4.2.4 Recent Developments.....	69
4.2.5 Relevant Material Research Survey	69
4.3 Hydrogen Storage Experimental Methods	71
4.3.1 Material Synthesis	71
4.3.2 Material Characterization	72
4.3.3 Hydrogen Storage Materials Testing.....	73
4.4 Research Approach	76

4.5 Results/Discussion	76
4.5.1 Characterization.....	76
4.5.2 Hydrogen Release.....	81
4.6 Hydrogen Storage Testing Summary	85
Chapter 5: Conclusion/Summary	86
References.....	87
Appendix 1: Lithium-ion battery reference figures	92
Appendix 2: Hydrogen storage reference figures	104

LIST OF FIGURES

Figure 1: Schematic showing components of lithium ion cell ¹	4
Figure 2: Discharge plot of LiMn ₂ O ₄ vs. Li/Li+	6
Figure 3: Battery energy density comparison ⁵	9
Figure 4: a) Schematic showing dendritic growth b) Schematic showing a layered anode ⁵	10
Figure 5: Cartoon of cycling transition metal oxide ¹²	11
Figure 6: Lithium cobalt oxide crystal structure ²	12
Figure 7: Cathode DSC comparison plot ²	13
Figure 8: Physical configurations of Li-ion batteries, a) Cylindrical b) Coin Cell c) Prismatic d) Thin and Flat polymer Li-ion ⁵	14
Figure 9: Dual sided anode and cathode coatings.....	15
Figure 10: Tightly wound electrodes in 18650 cells.....	16
Figure 11: Coating layout (not to scale)	17
Figure 12: Schematic of the Olivine structure ⁵	18
Figure 13: Lithium iron phosphate particle cartoon ¹⁹	19
Figure 14: MnO ₂ manganese centered oxygen octahedra structure (left) and LiMn ₂ O ₄ (right) with grey showing oxygen and black showing lithium ²	21
Figure 15: Cyclic voltammogram of LiMn ₂ O ₄ vs. metallic lithium ²¹	22
Figure 16: T-Cell configuration ⁸⁵	40
Figure 17: Compositional Diagram for Standard System.....	45
Figure 18: Compositional Diagram for Stabilized System.....	47
Figure 19: Standard System Specific Capacity Contour Plot (mAh/g)	49
Figure 20: Stabilized System Specific Capacity Contour Plot (mAh/g).....	50

Figure 21: Overlaid Specific Capacity Contour Plot (mAh/g)	51
Figure 22: Specific Capacity Plot for Composition b in the Standard System.....	52
Figure 23: Specific Capacity Plot for Composition f in the Stabilized System.....	52
Figure 24: Specific Capacity Plot for Composition 5 in the Stabilized System.....	53
Figure 25: Differential Capacity Plot for Standard System Composition b	54
Figure 26: Differential Capacity Plot for Stabilized System Composition f	55
Figure 27: Differential Capacity Plot for Stabilized System Composition 5.....	56
Figure 28: Rietveld Refinement of Standard Composition b.....	58
Figure 29: Rietveld Refinement of Stabilized Composition f	59
Figure 30: Rietveld Refinement of Stabilized Composition 5.....	61
Figure 31: Zoom of Low Angle Reflections in the Rietveld Refinement of Stabilized Composition 5.....	62
Figure 32: Cobalt XPS overlay.....	64
Figure 33: Ammonolysis set up (schematic courtesy of Dr. John Wilkes, Air Force Academy). 75	
Figure 34: XRD plot of Li_3AlH_6 with Ag, Al, and Zn catalysts.....	78
Figure 35: XRD plot of Li_3AlH_6 with La, Ce, Pr, Nd, and Y catalysts	79
Figure 36: XRD plot of $\text{LiNa}_2\text{AlH}_6$ with catalysts	80
Figure 37: SEM image of $\text{LiNa}_2\text{AlH}_6$	81
Figure 38: Thermal hydrogen release for Li_3AlH_6 compounds	82
Figure 39: Thermal hydrogen release of $\text{LiNa}_2\text{AlH}_6$	84
Figure 40: Synchrotron XRD Patterns of Samples Sent to ANLAPS, Converted to $\text{CuK}\alpha$ Wavelength	92
Figure 41: Cobalt Fit for Standard Composition b	95

Figure 42: Cobalt Fit for Stabilized Composition f	96
Figure 43: Cobalt Fit for Stabilized Composition 5.....	97
Figure 44: Manganese Fit for Standard Composition b.....	98
Figure 45: Manganese Fit for Stabilized Composition f.....	99
Figure 46: Manganese Fit for Stabilized Composition 5	100
Figure 47: Nickel Fit for Standard Composition b	101
Figure 48: Nickel Fit for Stabilized Composition f	102
Figure 49: Nickel Fit for Stabilized Composition 5.....	103
Figure 50: Sequential formation of $\text{LiNa}_2\text{AlH}_6$	104
Figure 51: XRD pattern of $\text{Li}_3\text{AlH}_6 + 2 \text{ mol\% Al}$	106
Figure 52: TGA plot of $\text{Li}_3\text{AlH}_6 + 2 \text{ mol\% Al}$	107
Figure 53: Post TGA XRD pattern of $\text{Li}_3\text{AlH}_6 + 2 \text{ mol\% Al}$	107
Figure 54: XRD pattern of $\text{Li}_3\text{AlH}_6 + 2 \text{ mol\% AlCl}_3$	108
Figure 55: TGA plot of $\text{Li}_3\text{AlH}_6 + 2 \text{ mol\% AlCl}_3$	108
Figure 56: Post TGA XRD pattern of $\text{Li}_3\text{AlH}_6 + 2 \text{ mol\% AlCl}_3$	109
Figure 57: XRD pattern of $\text{Li}_3\text{AlH}_6 + 2 \text{ mol\% AgCl}$	109
Figure 58: TGA plot of $\text{Li}_3\text{AlH}_6 + 2 \text{ mol\% AgCl}$	110
Figure 59: Post TGA XRD pattern of $\text{Li}_3\text{AlH}_6 + 2 \text{ mol\% AgCl}$	110
Figure 60: XRD pattern of $\text{Li}_3\text{AlH}_6 + 2 \text{ mol\% Zn}$	111
Figure 61: TGA plot of $\text{Li}_3\text{AlH}_6 + 2 \text{ mol\% Zn}$	111
Figure 62: Post TGA XRD pattern of $\text{Li}_3\text{AlH}_6 + 2 \text{ mol\% Zn}$	112
Figure 63: XRD pattern of $\text{Li}_3\text{AlH}_6 + 2 \text{ mol\% ZnCl}_2$	112
Figure 64: TGA plot of $\text{Li}_3\text{AlH}_6 + 2 \text{ mol\% ZnCl}_2$	113

Figure 65: Post TGA XRD plot of $\text{Li}_3\text{AlH}_6 + 2 \text{ mol\% ZnCl}_2$	113
Figure 66: XRD pattern of $\text{Li}_3\text{AlH}_6 + 2 \text{ mol\% ZnO}$	114
Figure 67: TGA plot of $\text{Li}_3\text{AlH}_6 + 2 \text{ mol\% ZnO}$	115
Figure 68: Post TGA XRD pattern of $\text{Li}_3\text{AlH}_6 + 2 \text{ mol\% ZnO}$	115
Figure 69: XRD pattern of $\text{Li}_3\text{AlH}_6 + 2 \text{ mol\% FeCl}_2$	116
Figure 70: TGA plot of $\text{Li}_3\text{AlH}_6 + 2 \text{ mol\% FeCl}_2$	116
Figure 71: Post TGA XRD of $\text{Li}_3\text{AlH}_6 + 2 \text{ mol\% FeCl}_2$	117
Figure 72: $\text{Li}_3\text{AlH}_6 + 2 \text{ mol\% FeCl}_3$	117
Figure 73: TGA plot of $\text{Li}_3\text{AlH}_6 + 2 \text{ mol\% FeCl}_3$	118
Figure 74: Post TGA XRD pattern of $\text{Li}_3\text{AlH}_6 + 2 \text{ mol\% FeCl}_3$	118
Figure 75: XRD pattern of $\text{Li}_3\text{AlH}_6 + 2 \text{ mol\% LaCl}_3$	119
Figure 76: TGA plot of $\text{Li}_3\text{AlH}_6 + 2 \text{ mol\% LaCl}_3$	119
Figure 77: Post TGA XRD pattern of $\text{Li}_3\text{AlH}_6 + 2 \text{ mol\% LaCl}_3$	120
Figure 78: XRD pattern of $\text{Li}_3\text{AlH}_6 + 2 \text{ mol\% CeCl}_3$	120
Figure 79: TGA plot of $\text{Li}_3\text{AlH}_6 + 2 \text{ mol\% CeCl}_3$	121
Figure 80: Post TGA XRD pattern of $\text{Li}_3\text{AlH}_6 + 2 \text{ mol\% CeCl}_3$	121
Figure 81: XRD pattern of $\text{Li}_3\text{AlH}_6 + 2 \text{ mol\% PrCl}_3$	122
Figure 82: TGA plot of $\text{Li}_3\text{AlH}_6 + 2 \text{ mol\% PrCl}_3$	122
Figure 83: Post TGA XRD pattern of $\text{Li}_3\text{AlH}_6 + 2 \text{ mol\% PrCl}_3$	123
Figure 84: XRD pattern of $\text{Li}_3\text{AlH}_6 + 2 \text{ mol\% NdCl}_3$	123
Figure 85: TGA plot of $\text{Li}_3\text{AlH}_6 + 2 \text{ mol\% NdCl}_3$	124
Figure 86: Post TGA XRD pattern of $\text{Li}_3\text{AlH}_6 + 2 \text{ mol\% NdCl}_3$	124
Figure 87: XRD pattern of $\text{Li}_3\text{AlH}_6 + 2 \text{ mol\% YCl}_3$	125

Figure 88: TGA plot of $\text{Li}_3\text{AlH}_6 + 2 \text{ mol\% YCl}_3$	126
Figure 89: Post TGA XRD of $\text{Li}_3\text{AlH}_6 + 2 \text{ mol\% YCl}_3$	126
Figure 90: XRD pattern of $\text{LiNa}_2\text{AlH}_6$	127
Figure 91: TGA plot of $\text{LiNa}_2\text{AlH}_6$	127

Chapter 1: Introduction

This dissertation is focused on improving the current methods of energy storage in transportation applications in an attempt to enable renewable energy technologies replace fossil fuels. At this point, the most attractive technologies are lithium ion batteries for primary energy storage, and hydrogen fuel cells for extended range. The critical areas limiting use of these technologies are addressed in this work. This appears in two forms in this work, direct electrochemical storage of electricity in lithium ion batteries, and the storage of hydrogen fuel for later conversion back into electricity in a hydrogen fuel cell. The underlying material issues are addressed for both lithium ion batteries and hydrogen fuel storage are outlined in the following chapters.

Chapter two is focused on lithium ion batteries. This chapter outlines the fundamentals and limitations of the technology, as well as a basic understanding of the function of the devices. The cathode material is shown to be the limiting component, and is the focus of the research in this work. A survey of the relevant literature is provided, leading into the approach for improving the cathode material. A system of diverse composite cathodes using carefully chosen components are synthesized using a sol-gel method and fixed synthesis conditions in an attempt to produce a low cost material with favorable electrochemical performance, and is covered in detail in chapter three. A combination of careful structural, electrical, and electrochemical characterization is combined with the electrochemical performance of these materials to map out the compositional space and show the most appealing composition regions.

Chapter four exposes the limits of current hydrogen storage technologies. The most promising of these technologies is then further scrutinized with a literature survey to determine its limiting factors. The survey shows that the method with the best potential is solid-state

storage of the hydrogen in complex chemical hydrides. The limiting factor for these materials is the inability to release all of the stored hydrogen in the material. Also, the rate at which the hydrogen can be inserted and released from the material is a large challenge in bringing these materials toward commercialization. Using techniques consistent with the literature survey, these complex chemical hydrides are synthesized and then doped with a variety of catalyst materials in an attempt to improve the hydrogen yield during release. These materials are characterized and tested for both thermal and ammonia assisted hydrogen release, highlighting which catalysts have a positive effect.

The final chapter provides a concise summary of the findings for both the lithium ion battery cathode materials and the catalyzed complex chemical hydrides. The implications of these findings are also illustrated. A direction for future work in both of these areas is suggested as well.

Chapter 2: Lithium-ion Batteries Background, Literature Survey, and Methods.

2.1 Purpose and Aim of Research

Energy storage is an important aspect of everyday life and is becoming increasingly important moving into the future. Improvements in energy storage need to be made in order to enable other important technologies to succeed. Examples of this include transportation improvements such as electric and hybrid vehicles, as well as full utilization of renewable energy technologies such as wind and solar. Many new technologies have been presented over the past century, each of which find use in specific applications. The specific focus of this research is creating low cost and high gravimetric energy density storage technologies, in the hope of enabling new transportation technologies to be practical and affordable.

2.2 Lithium Ion Battery Introduction

2.2.1 Definitions

To understand the lithium-ion (Li-ion) cell research presented in this work there are several terms that need to be understood. A Li-ion cell is an electrochemical cell that stores energy chemically through redox reactions. In this case the lithium ions serve as the charge carriers. Note that a Li-ion battery is actually a collection of multiple lithium-ion cells connected in either series or parallel, but it is common to refer to an individual Li-ion cell as a battery, and these terms are used interchangeably throughout this work. Lithium-ion batteries, like all batteries, have an anode, cathode, and electrolyte. The anode acts as the negative electrode, and during battery discharge it oxidizes and gives up electrons to the external circuit. The cathode is the positive electrode, and accepts the electrons while reducing during the discharge cycle. The

electrolyte is the medium through which the ions travel between the electrodes to maintain charge balance. These components are pictured schematically in the following cartoon (Figure 1), and details about each part of the battery are in the following section.

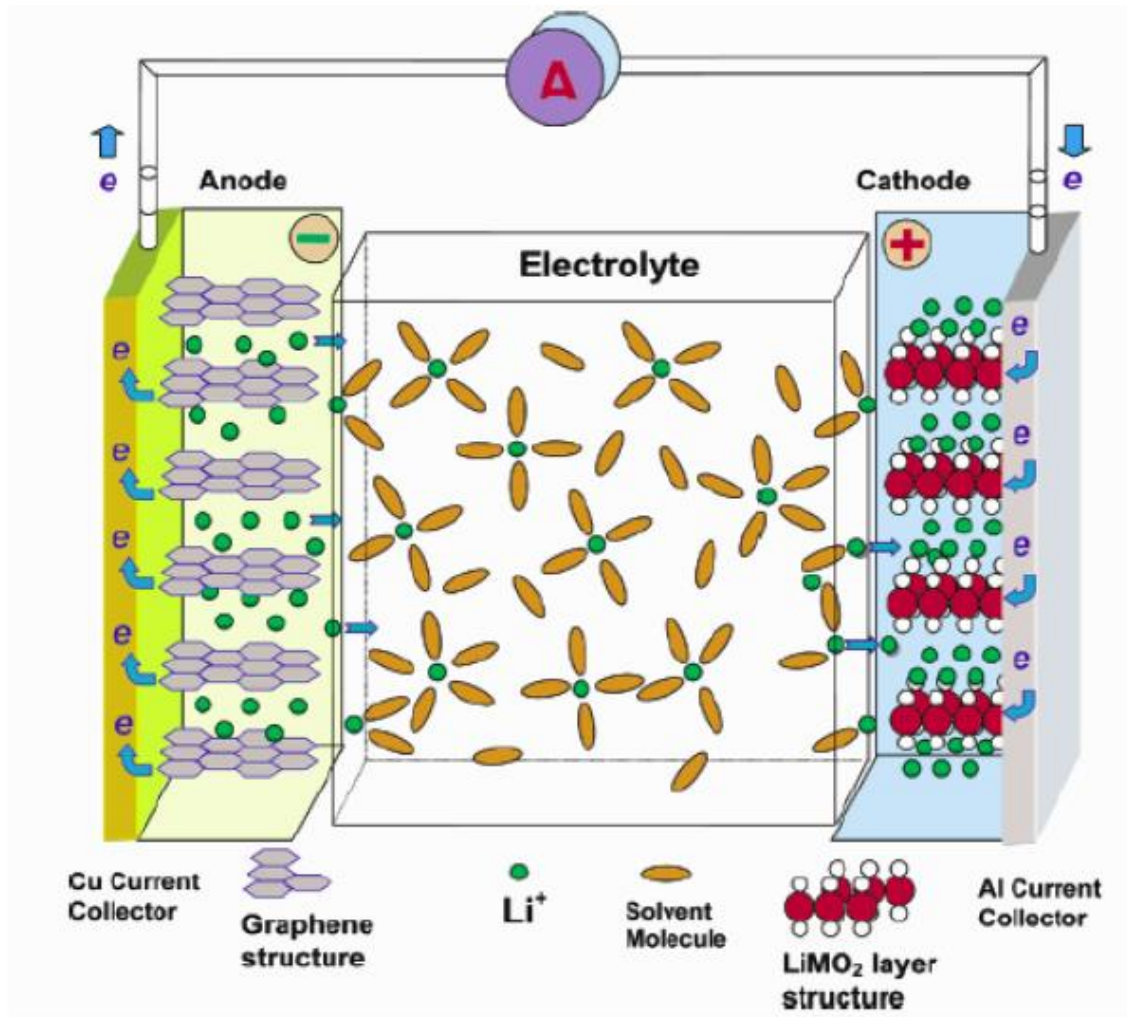


Figure 1: Schematic showing components of lithium ion cell ¹

The amount of energy stored in a cell is referred to as the capacity, and is typically discussed in units of ampere hours (Ah). The more useful term for battery performance in research is specific capacity. This is a measure of stored capacity per weight of active material (mAh/g), and excludes the weight of other parts of the electrode or packaging materials. Typical

values for the common cathode material (LiCoO_2) and the common anode material (MCMB carbon) are 140 mAh/g and 270 mAh/g respectively².

Charge and discharge rates of the battery are often in terms of "C-rate". This describes the magnitude of the current used in charging and discharging the cell relative to the total capacity of the battery. For example, when charging a 1 Ah capacity battery at 5 Amps it is being charged at a 5C rate. Typically initial charge and discharge rates are low in research, around C/15, and are increased after initial testing to help isolate reasons for performance, such as slow kinetics or low electrical conductivity. Rate capability can be addressed by increasing the surface area to aid ion transport, or by adding conductive carbon to increase electron transport.

Galvanostatic charge and discharge is the most common method for testing the cycling performance of each cell, and is done by cycling the cells at a constant current and measuring the voltage. The resulting data is plotted in a discharge plot, with the calculated specific capacity vs. voltage (Figure 2). These plots are very useful, and provide much more information than simply the total specific capacity. The shape of the profile can indicate the nature of the reaction, such as multiple redox couples, multiple insertion sites, and the type of reaction. For example a two phase reaction (reconstitution reaction) is very flat, where as a single phase solid solution type reaction the profile will have a larger slope to it³.

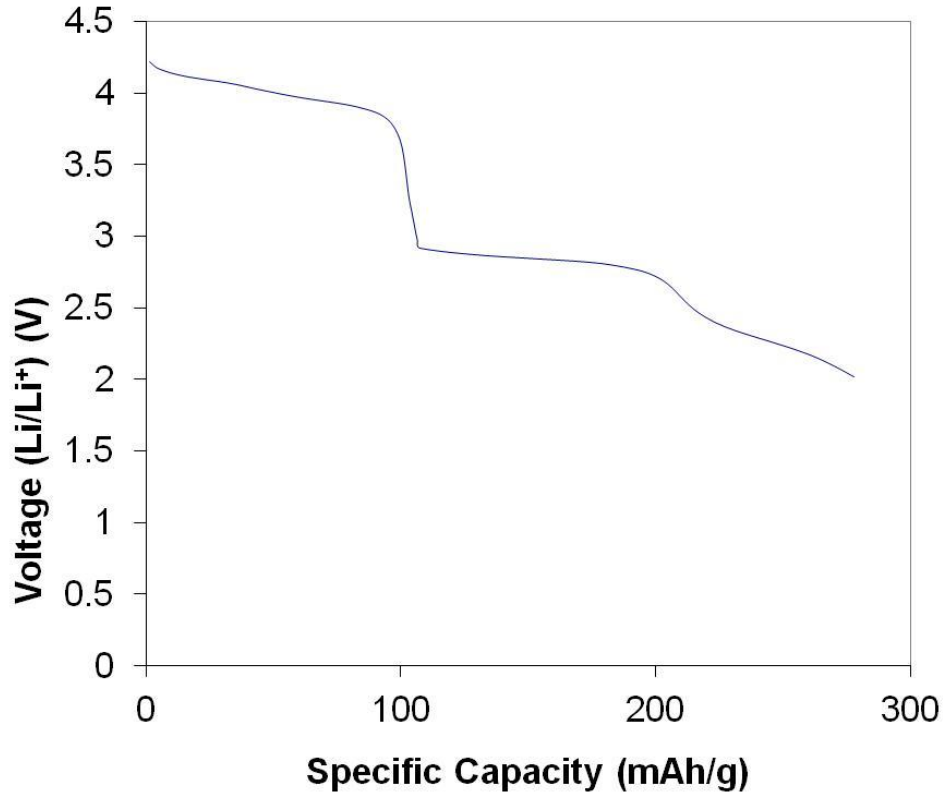


Figure 2: Discharge plot of LiMn₂O₄ vs. Li/Li⁺

2.2.2 Design Considerations

The positive electrode is often the area that gets the most attention during research because it is the most significant limitation to increasing the capacity of a battery to date. There is much room for improvement in existing cathode materials. Ideally the cathode will have a high free energy of reaction with lithium². This is what drives the reaction and makes the cell function. The cell needs to incorporate large quantities of lithium reversibly without structural change associated with the electrode material. A large change in lattice parameter upon cycling can affect the structural integrity of the electrode, causing poor cycling and a short battery life⁴. The cathode needs to have good ionic conductivity to allow the lithium ions to move quickly through the structure. Electrical conductivity is also very important because without electron

mobility, there will be no charge transfer and the reduction reaction cannot happen. High conductivity also means low resistance, which is important, as internal resistance will limit the power capabilities of the battery. The cost of raw materials as well as material synthesis processes needs to be low in order to have an affordable end product.

The anode needs to have a low electrochemical potential relative to the cathode; otherwise the power of the cell would be reduced. The desired characteristics of the anode are low cost, high electrical conductivity, reversible reactions with lithium, and low reactivity with the electrolyte. With similar ideal criteria, it is apparent that the cathode material is the limiting part of the battery as it has a much lower specific capacity and a higher cost than the common anode material MCMB carbon. The high cost of LiCoO_2 is mainly due to the high cost of cobalt.

What is commonly referred to as the electrolyte is actually a mixture of a solvent and a supporting electrolyte, typically a salt. The purpose of the supporting electrolyte is to help facilitate ion transport. The supporting electrolyte and solvent must be ionically conductive but not electrically conductive. The electrolyte needs to dissolve readily in the solvent. The electrolyte must not detrimentally react with the anode, cathode, or any other component of the cell, and more importantly, must not have a reduction or oxidation of its own that occurs in the operating voltage range. Low cost and an environmentally benign nature are also important with the electrolyte.

The separator serves the purpose of physically separating the two electrodes so that electrical contact is not made. The separator should be able, however, to transport the ions readily across its boundary. Typical separators are porous materials that are soaked in the liquid electrolyte. The performance of these separators under heat is very important as they often are

made of polypropylene or polyethylene polymers, and their melting could cause the battery to short.

2.2.3 Evolution of the Lithium Ion Battery

2.2.3.1 Advantages of lithium

Lithium-ion batteries today are used in a variety of applications for good reason. These batteries are very attractive for their high energy density and high cell potential. Energy density is similar to specific capacity, but it also accounts for the voltage of the cell, so it is a good measure of total energy of the cell per unit weight, and is typically represented as Wh/kg. With a nominal voltage greater than 3 V per cell and the highest energy density (Wh/kg) of any commercial rechargeable battery technology, Li-ion batteries are an easy choice in mobile electronics. In comparing different battery energy densities, both volumetrically and gravimetrically, this is very apparent (Figure 3). The following figure shows volumetric and gravimetric energy densities plotted against each other. A high volumetric energy density (energy per volume) and a high gravimetric energy density (energy per weight) are desirable in many applications, such as mobile electronics.

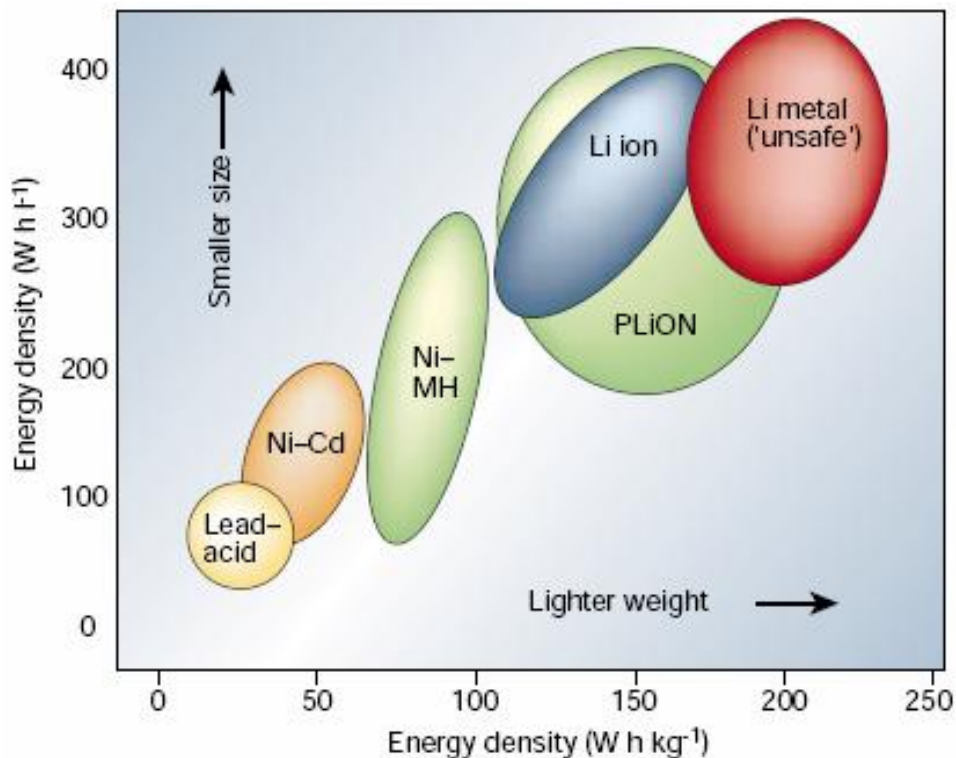


Figure 3: Battery energy density comparison⁵

Lithium was not chosen as the charge carrier by accident. With a very small atom size that is very willing to donate an electron, lithium batteries have the potential to provide high power with a small light footprint.

2.2.3.2 Early Attempts

Lithium-ion batteries have been developing for many years. Li metal batteries were demonstrated in the 1970s as primary (non-rechargeable) cells⁶. These first batteries quickly found their way into watches and medical devices. At this same point in time, inorganic materials were shown to interact with alkali metals reversibly⁷. These types of reactions are called insertion reactions, or intercalation reactions if it is in a layered structured material. This led to the first rechargeable Li systems.

In 1972 Exxon started making these batteries with TiS_2 as the cathode and a Li metal anode⁸. While the positive cathode worked well, the lithium metal anode was shown to have uneven dendritic growth during cycling. This can lead to failure as described later in the text. Lithium metal anodes are compared with layered carbon below (Figure 4).

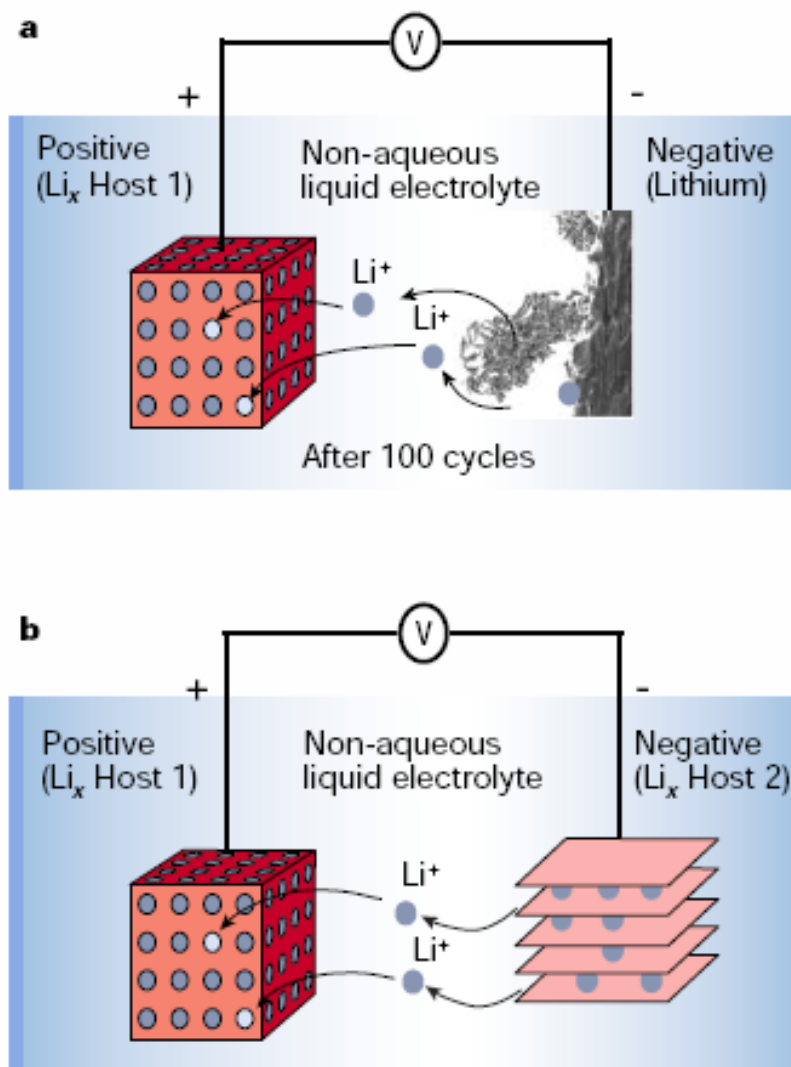


Figure 4: a) Schematic showing dendritic growth b) Schematic showing a layered anode⁵

Many solutions to this problem were proposed which included using ionic Li^+ as the charge transport mechanism instead of metallic lithium in a “rocking chair” Li-ion battery. This

was first demonstrated by Murphy et al in 1978⁵. Many new insertion compounds were developed, and a move toward oxides with a higher potential was made to compensate for higher potential anode materials⁹. Goodenough et al introduced a new group of materials Li_xMO_2 (where M is Co, Ni or Mn) still used today¹⁰. In 1991 the SONY Corporation commercialized these rocking chair batteries using a layered carbon anode and a LiCoO_2 cathode¹¹.

LiCoO_2 is in the family of cathode materials generically called the transition metal oxides. This material has a layered crystal structure and ideally charges and discharges with the structures shown below (Figure 5).

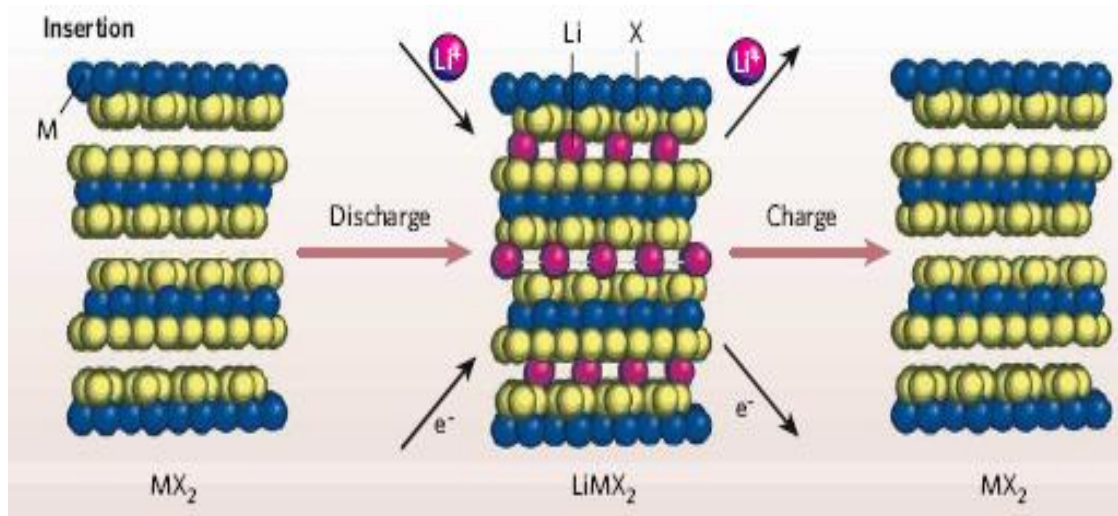


Figure 5: Cartoon of cycling transition metal oxide¹²

The atoms for this layered structure are arranged according to Figure 6.

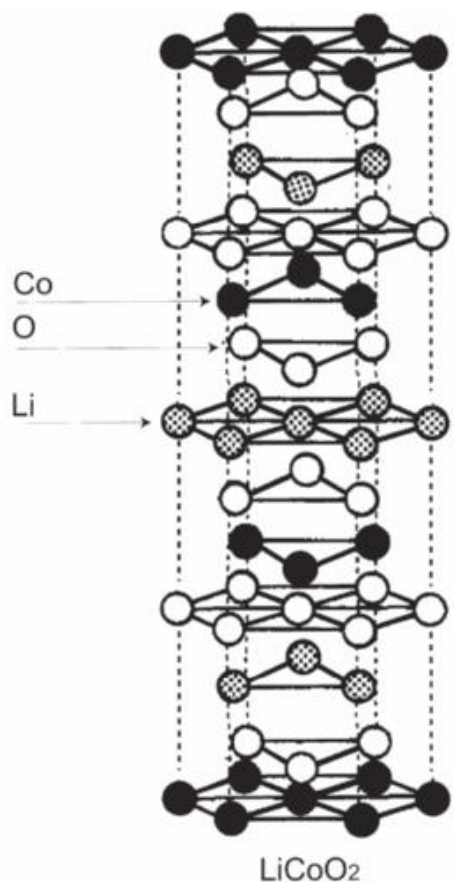


Figure 6: Lithium cobalt oxide crystal structure²

This particular type of insertion reaction is sometimes called an intercalation reaction, and is distinguished by the layered structure. The first batteries marketed, and the majority of those currently available, still use LiCoO₂ as a positive electrode². Lithium cobalt oxide is not difficult to synthesize and possesses high electrical conductivity. A practical specific capacity of 120 - 140 mAh/g is typical with this material⁵. LiNiO₂ is another example of this layered structure which has a higher specific capacity, but is not used as much due to a higher thermal instability². Doping LiCoO₂ with other metals while maintaining the layered oxide structure can increase the capacity and still maintain considerable thermal stability¹³.

One technique used to characterize the thermal stability of these cathodes is differential scanning calorimetry (DSC). This test heats the material and measures the heat flow of the material. The shape of the plot generated from DSC can yield very useful information such as phase changes, melting points, and decomposition temperatures. The following is a plot showing the results of one of these tests on transition metal oxides, with the peaks indicative of the exothermic reaction of the cathode material with the electrolyte when heated above about 210°C (Figure 7).

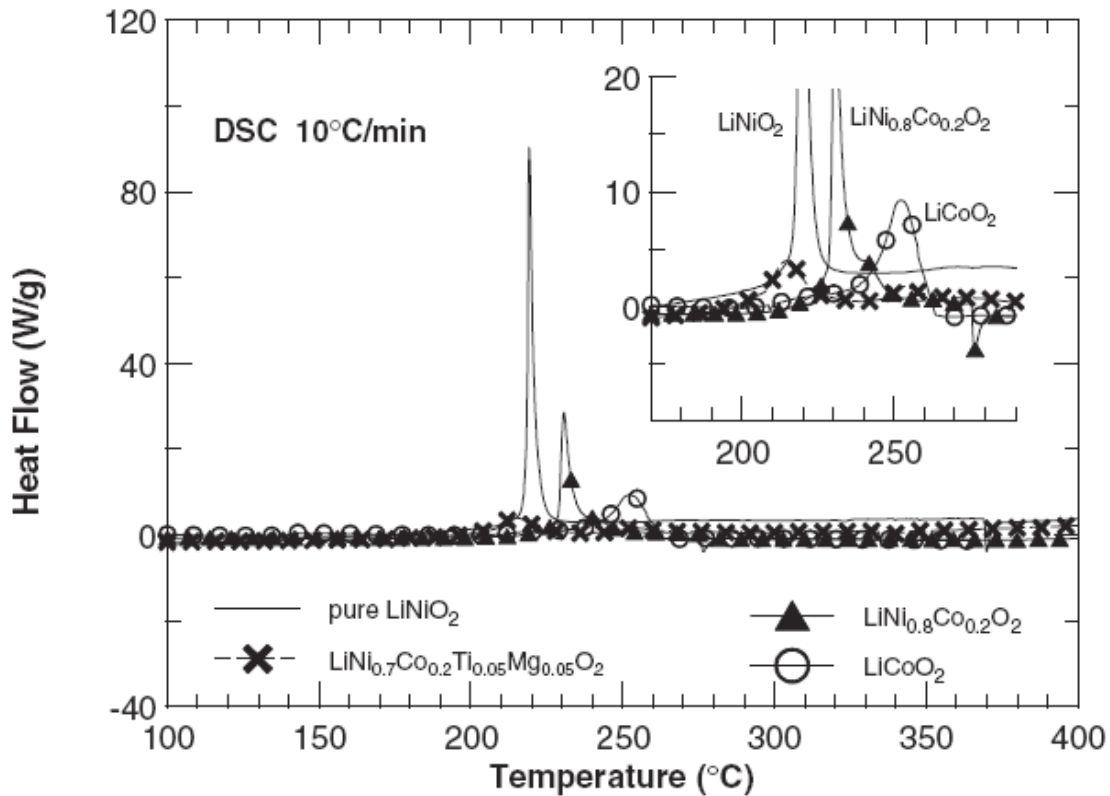


Figure 7: Cathode DSC comparison plot ²

2.2.4 Cell Configuration

The cell configurations described in this section are on a larger scale than the ones used to test in this research, but provide some perspective into what the next step for newly developed

battery materials to be commercialized. The coating characteristics described below are also desired in the lab scale batteries to give good cell performance. As mentioned before, generally the cathode material of the lithium ion batteries on the market today is LiCoO_2 . A layered MCMB carbon typically is used as the anode active material. A solution of 1M LiPF_6 dissolved in different ratios of propylene carbonate (PC), ethylene carbonate (EC), and dimethyl carbonate (DMC) makes up the common electrolyte. The physical separator is a porous sheet polymer composed typically of polyethylene and/or polypropylene that prevents shorting, but allows Li ions to flow unobstructed².

These components are put together in a variety of configurations for different applications as shown below (Figure 8).

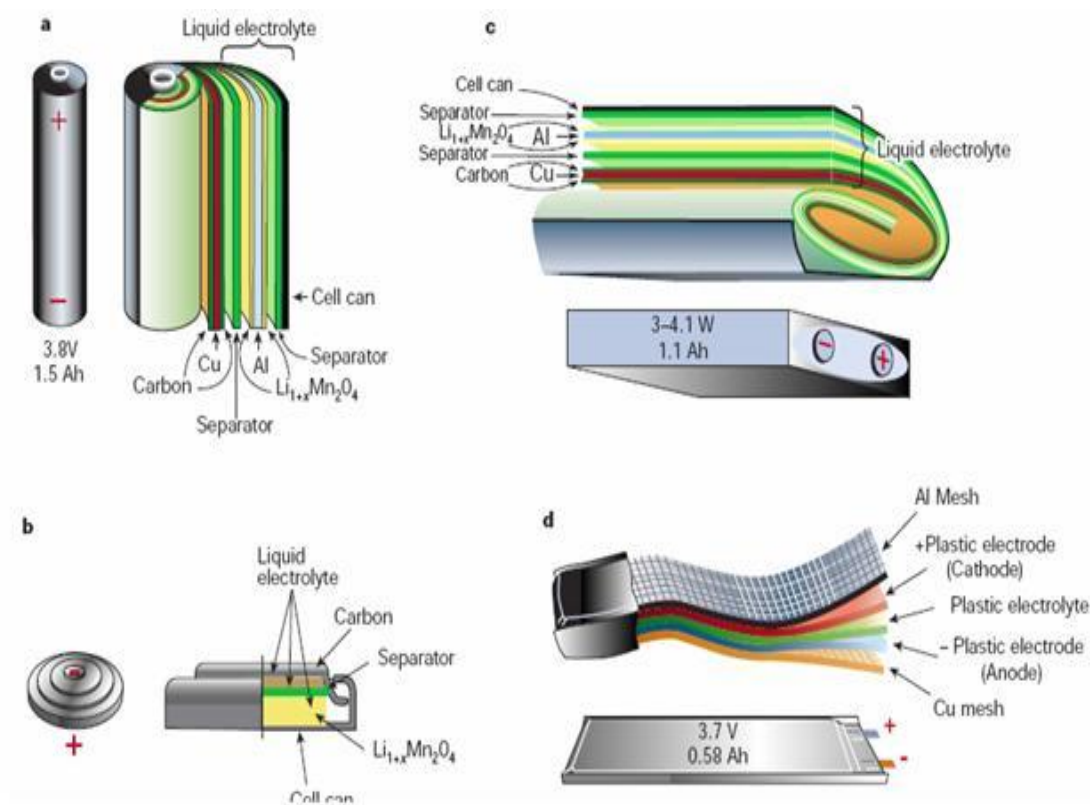


Figure 8: Physical configurations of Li-ion batteries, a) Cylindrical b) Coin Cell c) Prismatic d) Thin and Flat polymer Li-ion⁵

In Figure 8a, the wound 18650 cell is pictured schematically. The cathode is made of an aluminum substrate, which is coated with a mixture of active material (LiCoO_2), conductive carbon additive, and a polymer binder on both sides. The anode is made up of a copper substrate with MCMB carbon coated on both sides with the same polymer binder. Note that the substrates for both the anode and cathode electrodes serve as the current collectors as well. These coatings are uniform in thickness, well bonded to the substrate, and without major cracking flaws or pinhole defects. The following figure shows the electrodes removed from a commercial 18650, and are a great example of quality coatings free of cracks or pinholes (Figure 9).

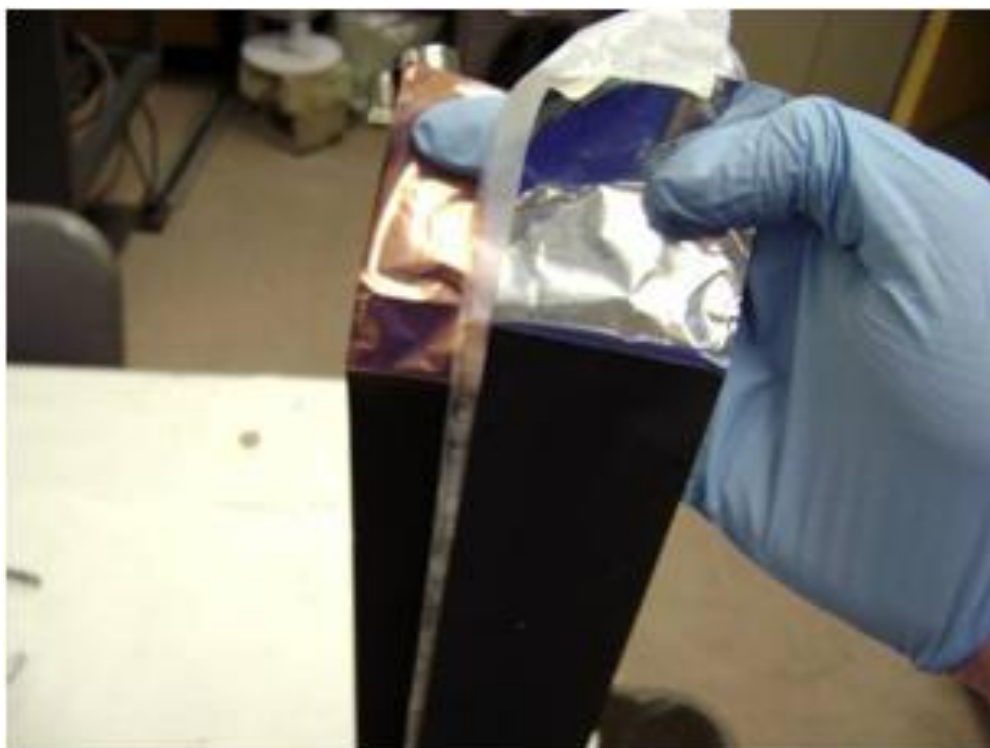


Figure 9: Dual sided anode and cathode coatings

The anode and cathode are tightly wound around each other with the physical separator in-between (Figure 10). Intimate contact is important to aid in diffusion, which is done with the

aid of a precision winding machine. The separator is wetted with a small amount of electrolyte necessary to facilitate ion transport.



Figure 10: Tightly wound electrodes in 18650 cells

It is interesting to note that each manufacture of these 18650 cells has subtle differences in their design, such as placement of the electrode lead. Similarities between all of them include the anode being slightly larger than the cathode, and the separator slightly larger than them both, to avoid shorting. The negative lead is attached to the case bottom, and the positive is attached to the case top through a safety valve. A thin layer of plastic is in-between the two for shorting prevention. A layout of a cell of one of the most common 18650s is shown below (Figure 11).

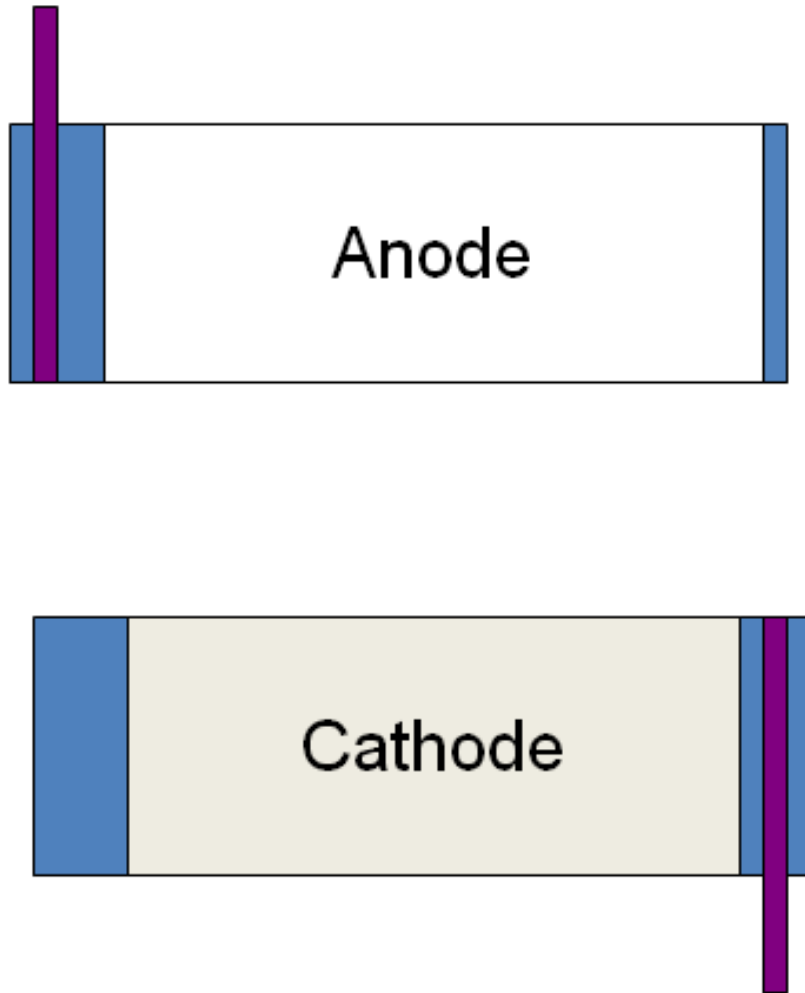


Figure 11: Coating layout (not to scale)

2.2.5 Recent Developments

There has been a movement in research from the aforementioned layered structure transition metal oxides toward cathode materials with three dimensional frameworks. There are several material groups with this three dimensional framework including olivine, nasicon, and spinel structure. One common olivine structured material is LiFePO_4 . This material has a theoretical capacity of roughly 170 mAh/g and has been shown to reach up to 165 mAh/g in practice¹⁴⁻¹⁵. The crystal structure is pictured schematically below (Figure 12).

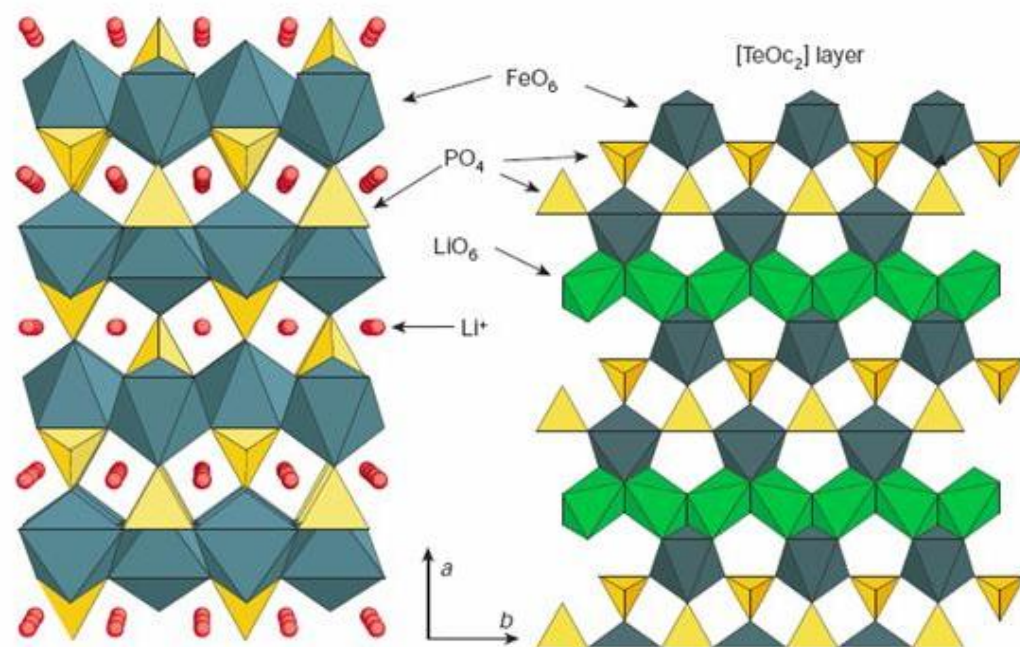


Figure 12: Schematic of the Olivine structure⁵

This figure shows LiFePO_4 structure projected on the $[001]$ plane, and the key is that the lithium ions can move along the $[010]$ and $[001]$ planes⁵. This cathode active material is thermally stable because its reactivity with electrolytes is very low¹⁶⁻¹⁸. Other benefits of this active material include low cost, low toxicity, and environmental friendliness¹⁹. One drawback of this material includes low electrical conductivity. This has been somewhat remedied by carbon coating the particles. Another drawback is the tendency of this material to form of two phases, a FePO_4 phase core and an outer LiFePO_4 phase shell seen as follows¹⁹⁻²⁰ (Figure 13).

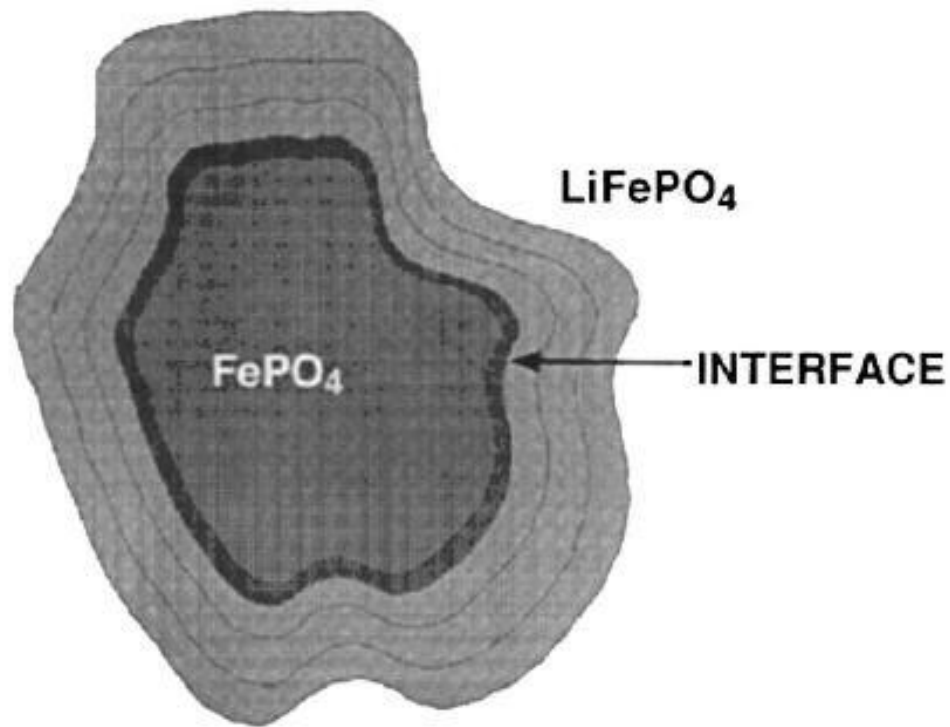


Figure 13: Lithium iron phosphate particle cartoon¹⁹

Research in producing these particles on the nanoscale has shown to partly remedy the situation. This material seems to have one of the highest potentials for commercial batteries in the future and is being pursued heavily.

There is a recent trend toward developing synthetic methods for controlled nanoscale morphologies of unlithiated cathode and anode materials to take advantage of high surface areas and potentially high rate capability. Many nanostructured materials such as silicon nanowires can be created with controlled morphologies, and have a very high theoretical capacity. These materials however suffer from a large expansion and contraction of the lattice upon cycling, and tend to pulverize themselves in just a few cycles. They also tend to have a low potential vs. Li and are more suitable for anode materials. Below is an introduction to the systems of materials

explored in this work. This includes a description of the material's structure, performance, and areas that need improvement.

2.2.6 Relevant Material Research Survey

2.2.6.1 LiMn₂O₄

2.2.6.1.a Basic Features

Lithium manganate has been one of the more researched materials over the last several years. Many attempts have been made to improve this material as it has several inviting attributes. For one, manganese compounds are naturally abundant and relatively inexpensive. Manganese is also an environmentally benign material and LiMn₂O₄ does not react exothermically with the electrolyte like LiNiO₂ or LiCoO₂. These exothermic reactions can lead to thermal runaway. During thermal runaway the exothermic reaction builds pressure in the cell and can cause it to rupture and ignite the flammable electrolyte solution.

The structure of LiMn₂O₄ is like that of the mineral spinel (MgAl₂O₄) and so it is said to have a "spinel" structure. This is a three dimensional framework cubic crystal structure based on λ -MnO₂ octahedra illustrated below (Figure 14), and has the space group symmetry Fd $\bar{3}$ m.

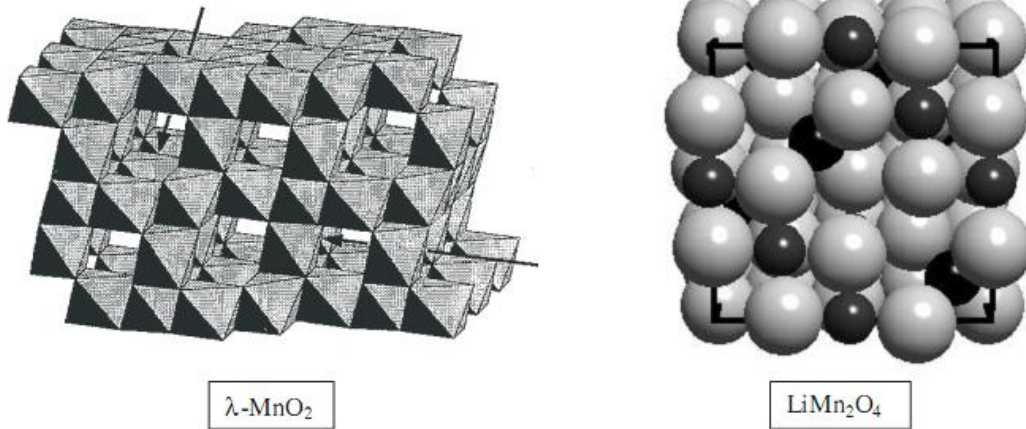


Figure 14: MnO_2 manganese centered oxygen octahedra structure (left) and LiMn_2O_4 (right) with grey showing oxygen and black showing lithium ²

This tunnel like structure allows lithium to move out of the structure without collapse. In this structure the Li occupies the 8a tetrahedral Wyckoff position while the Mn and O occupy the 16d and 32e octahedral sites respectively ²¹⁻²².

When tested using cyclic voltammetry between 2V - 4.5V, there are two 4V peaks separated by 150 mV associated with the insertion of Li into the 8a sites shown in Figure 15. The separate voltage of the second peak is proposed to be due to reordering of the lithium ions ²¹.

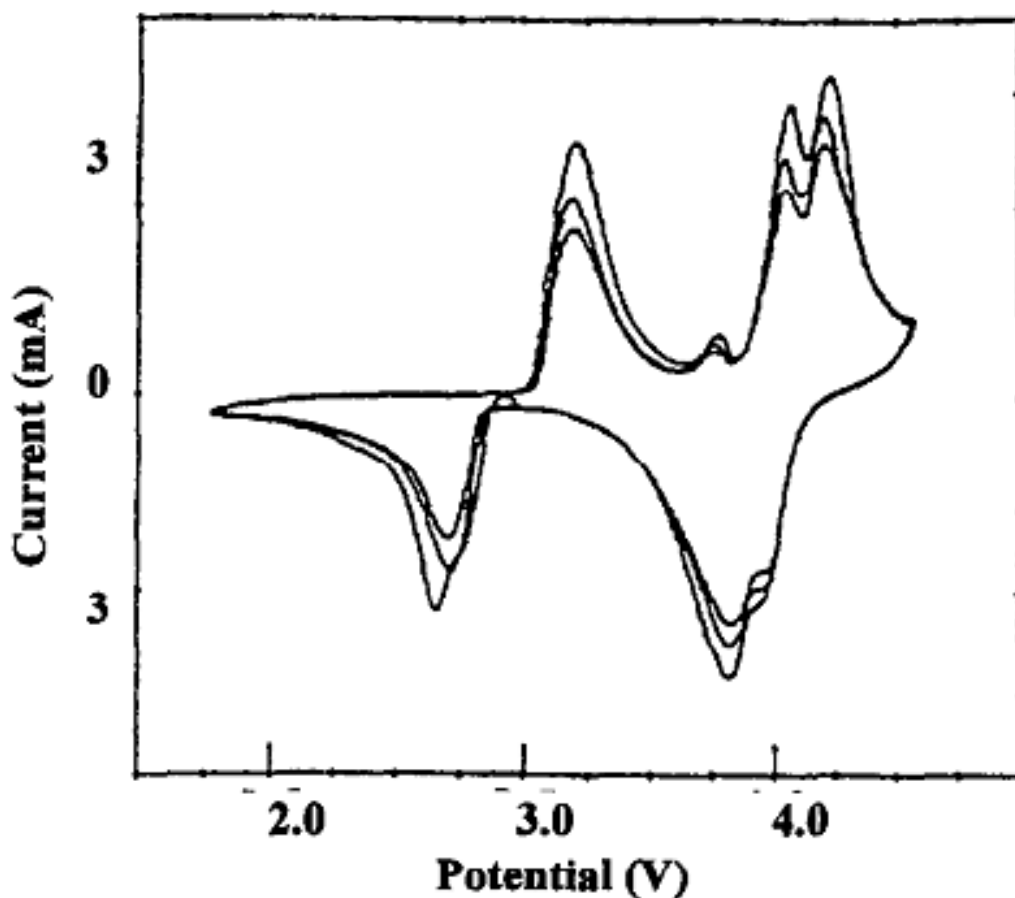


Figure 15: Cyclic voltammogram of LiMn_2O_4 vs. metallic lithium²¹

The 3 V redox is associated with insertion of Li into the 16a sites when $1 < x < 2$ in $\text{Li}_x\text{Mn}_2\text{O}_4$ ²¹, and commonly associated with a phase transformation from cubic to tetragonal caused by a Jahn-Teller distortion, which will be described later. The 3.8 V anodic peak seen in the above figure is still a subject of study. The typical specific capacity that can be expected from this material is 120 mAh/g at an average voltage of 4.0 V².

Several concerns with LiMn_2O_4 keep it from being the cathode material of choice, capacity fade being one of the biggest. Capacity fade refers to the gradual decrease in capacity of a battery upon repeated cycling. There are many different mechanisms in which capacity fade

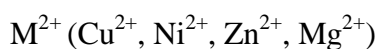
occurs in LiMn_2O_4 ²³. The first is the dissolution of Mn^{2+} into the electrolyte. LiMn_2O_4 has a mixed valence of $\text{Mn}^{3.5}$ when fully discharged. When charged, the Mn^{3+} ions undergo a disproportionation reaction producing Mn^{4+} and Mn^{2+} . The Mn^{2+} can dissolve irreversibly into the electrolyte, reducing the cathode capacity and degrading the carbon anode^{22,24}.

Another capacity fade mechanism is the aforementioned Jahn-Teller distortion, which is associated with the phase transition from the cubic structure to a tetragonal crystal structure in LiMn_2O_4 . This phenomenon is first explained in 1937 by H.A. Jahn and E. Teller²⁵. When the local concentration of Jahn-Teller active Mn^{3+} ions exceeds a critical level, local deformation occurs to stabilize the degenerative electronic state of these ions²⁶. This distortion can cause stress in the material, causing structural failure leading to disconnected and electrically inactive particles, reducing cell capacity over time^{2,21,27}. Several attempts have been made to address this specific issue in the literature²⁸⁻³². These attempts consist primarily of transition metal doping in an attempt to decrease the amount of Jahn-Teller active ions. There have also been attempts to improve the capacity fade by coating the material with different oxides^{23,33-36}. Doping of this material has also been attempted with many different metals to help improve the performance, with mixed results.

This material has a three dimensional cubic structure that has tunnels for lithium ions to travel through², which leads one to believe the structure will be stable upon cycling. Doping of LiMn_2O_4 with small amounts of M^{2+} and M^{3+} metals has been shown to occupy either the octahedral or tetrahedral sites forming ionic or covalent bonds³⁴. It is to be noted that the theoretical specific capacity for this material is 148 mAh/g when the redox reaction occurs between $\text{Mn}^{3+}/\text{Mn}^{4+}$ and only 1 Li^+ /molecule is available³⁴. Doping with metals of M^{3+} in high amounts can cause the capacity to decrease, as the $\text{Mn}^{3+} : \text{Mn}^{4+}$ ratio would decrease, leaving less

Mn^{3+} to be oxidized during the reaction, and thus reducing the capacity. Note that Mn^{4+} is not easily oxidized, and is considered electrochemically inactive. One possible way to increase the capacity is by doping the material with a higher oxidation state ion in an attempt to create more Mn^{3+} . In order to move forward and improve this material, previous attempts should be understood. A summary of the different attempts to improve this material follows.

2.26.1.b Cation Doping



Several different divalent metals have been doped into the parent spinel material with very interesting results. Doping with a divalent material will increase the average oxidation state of the Mn, reducing the Jahn-Teller active Mn^{3+} ions and the propensity of the material to go through a disproportionation reaction. However, this decreases the capacity of the 4V and 3V plateaus as there is less Mn^{3+} to oxidize.

Interestingly, Cu^{2+} has been doped in different amounts into the parent manganese spinel. This is shown to decrease the size of the 4 V plateaus however it creates a new plateau in the 5 V range. With an increasing dopant level up to $x = 0.5$ in $\text{LiCu}_x\text{Mn}_{2-x}\text{O}_4$, the theoretical 4 V capacity decreases to very low values, because when $x = 0.5$, the Mn is completely in an electrochemically dormant tetravalent state³⁷. The entire capacity at this level is from the Cu electrochemistry. The copper is shown to go through a $\text{Cu}^{2+}/\text{Cu}^{3+}$ redox reaction.

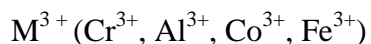
Similar results are reported for Ni^{2+} doped spinel. The same decrease in 4 V plateau is found with increasing dopant level for Ni up to $x = 0.5$ in $\text{LiNi}_x\text{Mn}_{2-x}\text{O}_4$. Nickel, however, undergoes a two electron transfer $\text{Ni}^{2+}/\text{Ni}^{4+}$ redox³⁷. Because this redox is a two electron process the theoretical capacity for an $x = 0.5$ sample is very close to that of an $x = 0$ sample. The 4 V

capacity should be eliminated with $x = 0.5$, however, upon cycling, a small 4 V plateau is observed³⁷. This means that there are still some Mn^{3+} ions in the structure. This could be due to the oxygen stoichiometry not being exact. The cyclability of this 5 V material is shown to have a 97 % retention after 25 cycles and a higher initial discharge capacity is observed³⁷. The Ni ions have been shown to reside partially in the 8a sites³⁷⁻³⁸. Ni^{2+} doping also decreases the lattice parameter with increasing dopant level³⁸. When dual substituted divalent metals are present, the voltage of the 5V plateaus is increased, but the capacity is decreased³⁷. With the addition of trivalent Al and Fe co-dopants, the 4 V capacity increased, and the 5 V capacity decreased.

Divalent Zn doped spinel samples show the normal 4 V discharge plateaus as well as an additional 5 V plateau upon initial charge and discharge with partial reversibility, however, they show very poor cyclability³⁹. The 5 V plateau is not attributed to an electrochemically active Zn ion. The Zn^{2+} ions occupy the 8a lithium sites and the displaced Li^+ is moved to the 16d sites³⁹. The 5V behavior is proposed to be the extraction of the lithium from the 16d sites. A large decrease in overall capacity is seen with this high level Zn dopant. In low amounts however, dual doped $\text{LiZn}_{0.01}\text{Ce}_{0.01}\text{Mn}_{1.98}\text{O}_4$ is shown to have a high capacity of 124 mAh/g for the 4 V redox peaks along with very good cyclability, coulombic efficiency, and capacity retention⁴⁰.

Magnesium ions are shown to have a very predictable behavior upon doping. Increasing the amount of Mg^{2+} dopant increases the average valence of the Mn ions. This leads to a lower capacity following the logic above. Upon testing, the actual specific discharge capacities closely follow the trend of the calculated ones³². The capacity retention seems very consistent, and does not decrease with cycling. Inhibition of the Jahn-Teller distortion is suggested to occur in spinel with a higher Mg^{2+} content, due to the increase in the $\text{Mn}^{4+}/\text{Mn}^{3+}$ ratio⁴¹.

Overall, doping with divalent metals has shown only limited success. A general trend of decreasing 4V capacity with the addition of a dopant is consistent in the different metals. There also is the appearance of a high 5V plateau in some cases, which opens a new class of high voltage cathode materials for exploration.



Many trivalent materials have been shown to increase the cyclability of manganese spinel. The metallic ions typically are electrochemically inactive, and have higher metal oxygen bond strengths than the Mn-O bond³⁸. This higher bond strength may increase the overall stability of the structure.

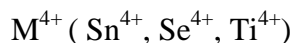
When doped with Cr^{3+} ions in small amounts manganese spinel is shown to increase the cyclability and stabilize the structure⁴²⁻⁴³. This dopant is shown to form stable undistorted homogeneously distributed MO_6 octahedra²⁸. A decreased initial capacity is found, however, very low fade is exhibited. The morphology of the sample was also not changed. When cycled to high voltage a 4.8 V plateau can be seen associated with the $\text{Cr}^{3+}/\text{Cr}^{4+}$ redox reaction⁴⁴. Structurally the Cr seems to have a strong preference for the octahedral sites, and when doped into the spinel, along with Mg^{2+} , similar results are found⁴⁴.

The Al^{3+} dopant has been found to be one of the best performing dopants in manganese spinel⁴³. It has been shown that Al^{3+} doping increases cyclability and can help to suppress the presence of Jahn-Teller distortion³⁰. The aluminum ions can be seen on both the 8a and 16d sites, with the later being the preferred site³⁰.

Manganese spinel doped with Co^{3+} forms a single phase in low concentrations and has some interesting effects on the material. This dopant decreases the lattice parameter³⁶. Cobalt

doped spinel is shown to have a high voltage discharge plateau that has been associated with the $\text{Co}^{3+}/\text{Co}^{4+}$ redox³⁶.

Iron-doped manganese spinels slightly increase the capacity retention, specific capacity, and lattice parameter⁴⁵ over pure LiMn_2O_4 ²². When added to two other dopants such as lithium, nickel, aluminum, or cobalt, a synergistic effect is seen, as even better capacity retention is achieved²². Overall, trivalent dopants tend to increase the cyclability of the material. This is typically at the cost of specific capacity, but better results are obtained with trivalent dopants than divalent dopants.



Tetravalent metallic dopants are the least common cation dopant for LiMn_2O_4 . This is because doping with a tetravalent metal will decrease the average valence of the manganese ions. This does not follow the same logic for decreasing the Jahn-Teller distortion and the disproportionation reactions mentioned before.

Sn^{4+} doping was attempted with promising results. The valence of the Sn^{4+} is shown to stay constant, making it an electrochemically inactive dopant⁴⁶. An increasing Sn content is shown to decrease the lattice parameter, and at low levels the tin doped $\text{LiSn}_{0.02}\text{Mn}_{1.98}\text{O}_4$ shows better capacity retention than LiMn_2O_4 undoped⁴⁶.

Se^{4+} shows a very interesting electrochemical properties when tested in the 3 V region. With the Jahn-Teller distortion still prominent during the cycling, the capacity fade in the doped samples is completely eliminated. This dopant actually shows a slight increase in specific discharge capacity with increasing number of cycles⁴⁷. The mechanism for this improved cycling is still unknown.

Tetravalent titanium ions have shown an increase in stability of the structure at low levels³⁴. Because titanium has a larger ionic radius than Mn^{4+} , at higher levels of doping it is thought to put a strain on the lattice, reducing the stability³⁴. There is a possibility to form a solid solution with one phase for the entire range of dopants, as LiTi_2O_4 is also spinel structured⁴⁸. The Ti ions do not always occupy the 16d sites, and can occupy the 8a sites³⁵.

2.2.6.1.c Anion Doping

Anion doping can also have an effect on the average valence of the manganese ions. One example of this is fluorine. When a parent LiMn_2O_4 is doped with F^- ions the average valence of the Mn ions is reduced. This can actually increase the Jahn-Teller distortion by creating a two phase composition consisting of a cubic phase and a orthorhombic phase⁴⁹. However, when excess lithium is also added, the cyclic capacity retention is increased⁵⁰. When dual doped with F^- and either Al^{3+} or La^{3+} , the cycling performance increases as well⁵¹⁻⁵³. Triple doped spinels with F^- , Li^+ , and Fe^{3+} , Co^{3+} , or Zn^{2+} , have also been shown to increase cyclability⁵⁴.

Another example of anion doping is sulfur. This is less studied than the aforementioned fluorine doping but it has interesting characteristics nonetheless. Sulfur doped spinel decreases the capacity of the 4 V plateau with increasing cycles. This is thought to be due to a weaker bond between the sulfur and manganese compared to the oxygen and manganese, leading to a weaker structure. The 3 V plateau, oddly enough, increases with cycling⁵⁵.

2.2.6.1.d Surface Modification

Modifying the surface of the LiMn_2O_4 particles can influence the electrochemical performance of material. Surface coatings can help with oxygen loss in active materials, which

can lead to reduced capacity. These surface coatings can also reduce interactions of the cathode material with the electrolyte.

The LiMn_2O_4 is coated with CoO , and then heated to form a solid solution $\text{LiCo}_x\text{Mn}_{2-x}\text{O}_4$ shell around the core. This has actually been shown to increase the initial discharge capacity as the cobalt participates in the redox reaction. The capacity retention is also improved as well as the possible C-rate of the material⁵⁶.

Coating the surface of pure LiMn_2O_4 with $\text{LiNi}_{0.5}\text{Mn}_{1.5}\text{O}_4$ is shown to suppress the onset of Jahn-Teller distortion in the 4 V region³¹. This distortion is proposed to be diffusion related and there is a buildup of Li ions on the surface of the material, decreasing the local average valence, and causing Jahn-Teller distortion. There is an associated stabilizing of the structure and increase in the capacity retention for coated samples⁵⁷.

2.2.6.1.e Stoichiometry Effects

Overlithiation

One way to try to combat the degradation mechanisms of the manganese spinels is to change the stoichiometry so that there is excess lithium. This can be described as $\text{Li}_{(1+x)}\text{Mn}_{(2-x)}\text{O}_4$. This is designed to increase the average oxidation state above 3.5 of the manganese²². Below 3.5 is where the Jahn-Teller distortion can become more evident and increasing the Mn^{4+} content of fully discharged spinel will reduce the amount of Mn^{3+} for the disproportionation reaction²¹. However, this will decrease the theoretical capacity of the material, because less than 100% of the Li will be removed when all the Mn is in the tetravalent state. This has been shown to decrease the initial capacity, but increase the cyclic performance and stability²².

Oxygen Stoichiometry

Oxygen deficiency in manganese spinel is reported to be one of the main reasons for poor cyclability at high temperature. This stoichiometry can be controlled with synthesis conditions including the heating atmosphere⁵⁸, heating temperature²⁴, and additional heating steps with added LiOH⁵⁹, as well as through Mg²⁺ doping⁵⁹. The oxygen deficiency can actually be seen with a small discharge plateau depending on the amount of deficiency at 3.2 V²⁴ as well as through regular XRD with Rietveld refinement⁵⁸. It is shown that this oxygen deficiency leads to high levels of Mn²⁺ dissolution into the electrolyte⁵⁹. The lowest levels of dissolution were found with a two step heating process, including additional LiOH added during a low temperature anneal, along with magnesium doping⁵⁹.

2.2.6.1.f LiMn₂O₄ summary

Many different dopants have been tested in an attempt to improve the cyclic performance of LiMn₂O₄. Several different cation and anion substitutions as well as different surface treatments and stoichiometry effects are shown to improve the cyclability of the material but sacrifice some capacity. A few of the substitutions have positive effects on the capacity of the material or introduce another high voltage plateau in the charge and discharge plots.

These small improvements in capacity, and mainly the cyclability improvements, make LiMn₂O₄ a good option for energy storage where cost is one of the major concerns. However, for applications where high energy density is the primary concern, or when a high discharge and charge rate is needed, other materials may be better options.

2.2.6.2 Layered Metal Oxides LiMO_2 ($M=\text{Ni, Mn, Co}$)

The most commonly used family of cathode materials in commercial applications are layered metal oxides, which have been extensively researched². These layered oxides vary in specific capacity as well as cyclability and safety with even slight changes in composition and structure⁶⁰. The most common cathode material for Li-ion commercial batteries is LiCoO_2 and it has a high theoretical specific of 273 mAh/g, but typically only realize around 140 mAh/g. This is due to oxygen pinning of the $\text{Co}^{3+/4+}$ redox couple, only allowing half of the lithium to be cycled⁶¹. There are many different approaches to improving the parent layered compounds such as LiCoO_2 and LiNiO_2 . A wide variety of intermediate solid solution compounds between these two materials exist and a few are described below.

2.2.6.2.a Cation Substitution

The substitution of the cation in these layered compounds has yielded several successful compounds such as $\text{LiNi}_{0.8}\text{Co}_{0.15}\text{Al}_{0.05}\text{O}_2$ and $\text{LiNi}_{0.3}\text{Co}_{0.3}\text{Mn}_{0.3}\text{O}_2$ ⁶². Addition of a additional cation can many effects on the electrode, including a tuning of the redox potential⁶¹. This has been taken advantage of by several groups in attempts to provide high capacity cathodes.

An example of this is in the cathode material $\text{Li}[\text{Li}_{0.2}\text{Cr}_{0.4}\text{Mn}_{0.4}]\text{O}_2$ explained by Ammundsen et al⁶³, and originally proposed in a system of chromium and manganese oxides by Storey et al⁶⁴. Chromium is an exciting active ion as it is stable in both the Cr^{3+} and Cr^{6+} oxidation states, and has the potential for a 3 electron transfer redox reaction. A trend of increasing capacity and decreasing cyclability with increasing chromium content is observed⁶⁴. The best performing aforementioned composition is explained in detail, with the manganese ions predominantly in the Mn^{4+} state, a reversible redox couple is observed in the chromium from Cr^{3+} to Cr^{6+} , including migration of the chromium ions from octahedral to tetrahedral sites

respectively with each cycle⁶³. This composition is essentially a solid solution of Li_2MnO_3 and LiCrO_2 , both of which are not viable cathode materials by themselves, but perform well in this combination⁶⁵. Even with the complex Cr-ion movement, this material yields an initial discharge capacity approaching 200mAh/g, but decreases to a stable 170mAh/g upon cycling at a C/2 rate. Interest in this material faded however partially due to the toxic nature of hexavalent chromium, and a high irreversible capacity loss after first cycle, and oxygen loss⁶⁶.

A large portion of research has been focused on various compositions of layered oxide materials containing nickel, manganese, and cobalt (NMC)⁶⁷⁻⁶⁹. These studies have yielded several compositions with relatively high capacities, but often suffer from low cyclability and a high irreversible capacity loss between first charge and discharge. Stabilizing of this reaction has been attempted with surface modifications and over-lithiation discussed in the following sections.

2.2.6.2.c Lithium Stoichiometry

Many attempts have been made to overlithiate cathode materials, that is having more than one lithium per formula unit. In NMC materials, this is essentially a solid solution of Li_2MnO_3 and various compositions of $\text{LiNi}_x\text{Co}_{1-x}\text{O}_2$. In some cases these approaches can yield impressive capacities⁶⁹

A less common approach to these materials is a decrease in lithium such as in $\text{Li}_{2/3}\text{Ni}_{1/3}\text{Mn}_{2/3}\text{O}_2$ explored by Paulsen⁷⁰. This material is prepared by a sodium ion exchange, and yields a surprising capacity of 171mAh/g at very low C-rates and does not have an exothermic reaction with the electrolyte at elevated temperatures. However, the performance dwindles with increasing rates. Materials with low conductivity (ionic or electric) become less

efficient with increasing C-rate, and when combined with ohmic heating the capacity of these materials suffers significantly. Depending on the material, these losses can be permanent due to structural degradation of the electrodes or decomposition of the electrolyte.

2.2.6.3 Mixed Structure Cathode Materials

The concept of combining multiple different cathode materials to improve performance is not brand new. This has been attempted previously with different systems of materials for different reasons, yielding mixed results. Park et al specifically tried integrating spinel structured and layered materials, but used the high voltage nickel substituted version of lithium manganate ($\text{LiMn}_{1.5}\text{Ni}_{0.5}\text{O}_4$) mixed with layered $\text{LiMn}_{0.5}\text{Ni}_{0.5}\text{O}_2$ and Li_2MnO_3 cathode materials. This research showed a high reversible capacity of 250 mAh/g, but this is over a very wide voltage range of 4.95-2V⁷¹.

A similar study by Johnson et al involving composite cathodes with layered Li_2MnO_3 and spinel structured LiMn_2O_4 is reported⁷². This study tested the composite electrodes over the same large potential window as Park et al, with similar specific capacity, however the average voltage of the cell is less with no high voltage $\text{LiNi}_{0.5}\text{Mn}_{1.5}\text{O}_4$ component. Both Park and Johnson show a significant low voltage spinel component associated with Jahn-Teller distortion. This work exhibited significant capacity fade.

These previous works provided some of the inspiration for the work in this dissertation. In eliminating the high voltage components such as Li_2MnO_3 and $\text{LiMn}_{1.5}\text{Ni}_{0.5}\text{O}_2$, a more stable electrode with a uniform discharge profile and small operating potential window is sought in this work. This work still takes advantage of the high capacity layered structures and the structural stability and high ion mobility of the spinel component consistent with recent works⁷¹⁻⁷², as well

as its inherent low cost by high manganese content. The addition of LiCoO_2 as an end member in this work provides a new approach and new insight into the area of composite cathodes.

2.2.6.4 Summary

Chosen for its small atomic radius and high electropositivity, lithium can be used in batteries to produce high voltage and lightweight cells. Lithium ion batteries have developed out of early attempts with lithium metal primary batteries. Reversible secondary cells were next to follow with a lithium metal anode and TiS_2 cathode. Problems with dendritic growth of the lithium metal anode lead to the use of layered transition metal oxides (LiMO_2) as the cathode material with a graphitic carbon anode. High cost and reactivity at high temperatures lead to development of other materials such as spinel structured LiMn_2O_4 and olivine structured LiFePO_4 . These materials have been extensively researched and can be improved with a variety of techniques including doping, coating, and sizing of particles. Recent developments in the use of composite cathode materials have shown promise and serve as inspiration to this work. The integration of spinel and layered structures has the potential to yield high specific capacity and rate capabilities, and this work provides a contribution to the literature through the use of different end members in the composite compositional diagram, focusing on a more stable potential window through the elimination of high voltage components.

2.3 Experimental Methods

2.3.1 Material Synthesis

Synthesis of the active cathode material varies greatly depending upon what composition and type of material is used. Techniques such as the sol gel, co-precipitation, and solid state

mixing are common. All of these techniques require post mixing heating to get the desired phase and burn off unwanted components of the precursors.

2.3.1.1 Sol-Gel Synthesis

This is a common synthesis technique and was the primary method used in the battery work. In this method the acetate precursors were chosen because they are soluble in water. The precursors were all dissolved in water and mixed in the liquid phase, which ensures good mixing, and is one of the advantages to this technique over solid state synthesis. Once all the precursors were mixed well and completely dissolved, a chelating agent was dissolved in a separate beaker and added. For this work citric acid was used, and dissolved in a separate beaker, then added to the solution in a 3:1 molar ratio. The solution was continuously stirred at 80°C heat and the water was evaporated overnight leaving a Gel like product. This product was then heated at low temperature (400°C) for 12hr to remove the organic components, leaving a homogeneous powder mixture of the precursor. This mixture was then ground by mortar and pestle and reheated to 800°C at a 3°C/min ramp rate for a 12hr dwell in air to form the crystalline phases. Note that this temperature is lower than that needed during the aforementioned solid state synthesis. The final product yields a uniform distribution of homogeneous small particles.

The temperature chosen to synthesize these materials was based on a combination of conditions found in the literature. A Li-Mn-O phase diagram proposed by Paulsen et al shows that at lower temperatures (around 800°C) for these compounds the cubic spinel phase LiMn_2O_4 is most stable, and at higher temperatures (near 1000°C) other phases such as the rocksalt phase Li_2MnO_3 , layered phase LiMnO_2 , as well as tetragonally distorted spinel $\text{Li}_2\text{Mn}_2\text{O}_4$ can form⁷³. This has been confirmed by other researchers in attempts to synthesize LiMnO_2 ⁷⁴. Layered LiCoO_2 by sol-gel method have been reported between 700-800°C⁷⁵⁻⁷⁶ and mixed cation layered

materials ($\text{LiNi}_{0.3}\text{Co}_{0.3}\text{Mn}_{0.3}\text{O}_2$ for example) typical synthesis is around 900°C , but is dependent on synthesis type^{67,77-79}. LiNiO_2 typically requires an oxygen atmosphere during heating⁶⁰. A few composite layered and spinel papers report synthesis at 900°C by co-precipitation method^{71,80}. By looking at these previous reports, a synthesis temperature of 800°C was chosen for the synthesis of the composite cathode materials in this work hoping to promote the growth of multiple phases.

2.3.2 Material Characterization

2.3.2.1 X-Ray Diffraction (XRD)

In order to make sure the desired phase is achieved, X-Ray Diffraction (XRD) was used. This analysis measures the distance between the planes of the crystal by varying the angle at which X-rays are incident on the sample while measuring the intensity of the X-Rays on the other side. Bragg's law of diffraction is the governing rule for this technique. This technique is also useful to determine crystallinity of the phase, if there are multiple phases present, and if there are impurities present. Broad peaks can also be representative of small particle size.

In determining the structure of the material for this work several techniques are used. First, the XRD data is performed on a Scintag X2 with a CuK_α wavelength of 1.5406 \AA . This data can be converted into a different format and imported into EVA software. This software allows users to enter in the elements present and search a database for previously reported materials that match both the location and intensities of recorded peaks. This is also a good way to qualitatively observe shift in peaks from expected standard value. The relative intensity and location of the peaks can be observed and compared to values from the database. The joint committee on powder diffraction standards (JCPDS) database also provides lattice parameter

data for the standard. Detailed structural analysis is done by applying the Rietveld structural refinement method. In this least squares refinement method a model is fitted to the raw diffraction data. This model includes background subtraction, instrument parameters, crystalline phases present with spacegroup and Wyckoff position of the atoms in each phase. This technique is exceptionally useful in this research in identifying the phases present, and determining a proper structural model for the material. The global fit parameter χ^2 is useful in comparing models, but if used incorrectly can be misleading. A good reference for understanding rietveld modeling and parameters used to compare them is published by Toby et al from the Advanced Photon Source at Argonne National Laboratory⁸¹.

2.3.2.2 X-Ray Photoelectron Spectroscopy (XPS)

XPS can be used to determine surface composition and electronic state of a material. Using photo-ionization, the material is bombarded with monochromatic X-rays, causing the ionization and emission of a core electron. The energy of this emitted photo-electron is measured, and using conservation of energy, it is used to identify the different elemental composition and electronic state of the material⁸². This can be a very useful technique in battery research and is used in this work because the electronic state of the material can give insight into what redox reactions are occurring when cycled.

2.3.3 Lithium Ion Battery Processing and Testing

2.3.3.1 Electrode Processing

Once the material was synthesized and the desired phase has been verified through XRD, the particle size is controlled by sieving the material to 45 μ m. Controlling the particle size is important for many reasons. Large particle size makes electrical conductivity increase as inter-

particle contact is better, however it decreases ionic conductivity. This is due to a larger distance for the ions to travel to leave the particle. Sieving all active materials to the size range eliminates that variable and allows the testing results to be more consistent. Once the material is sieved, it is made into an electrode in one of the following two ways.

2.3.3.1.a Solid Rolling

This a quick method of making electrodes during this research. This method is primarily used because it consistently produces quality electrodes. This method also allows for a small amount of active material to be used, conserving material.

In this method the three electrode components (active material, carbon, and a polymer binder) are weighed out in a 75%, 20%, and 5% respectively ratio and homogenously mixed. The carbon and active material are dry powders and the polymer binder (PTFE) is dispersed in water. Once the powders are mixed, the polymer solution is weight out and added to the powders mixture. These components are stirred together and then the water is dried off. Once dry, the mixture is rolled out manually using a rolling pin and electrode disks are punched out of the newly created electrode sheet. The carbon aids in the electrical conductivity of the electrode, while the polymer binder holds everything together and can act as a stress reliever during cycling as the lattice expands and contracts with lithium insertion. These electrodes upon completion are without visible defects such as cracks and are kept within a certain weight range for consistency.

One disadvantage to this method is that it is time and labor intensive in rolling out the electrodes. It is also difficult to maintain consistent weights of the electrodes as thickness is not easily controlled.

2.3.3.1.b Slurry Coatings

The second method for producing cathodes resembles closely what is done in industry. In this method a varying ratio of active material, carbon, polymer binder, and solvent are homogeneously mixed into a slurry. This ratio is dependent on the active material that is used, as different active materials have different specific surface areas, which require different amounts of the liquid components to achieve the proper viscosity. In industry, the goal is to make the highest percentage active material possible, while still maintaining coating quality (binder content and coating loading), and sufficient electrical conductivity (carbon content). The percentage of each component in the slurry is very tightly controlled to have the highest amount of active material per volume possible, while still maintaining coating quality and good conductivity. Increasing the tap density of the cathode material is an area of research focused on particle morphologies in order to improve volumetric energy density⁸³. This slurry is tape cast onto an aluminum foil using a doctor blade or coating machine. Often coatings are then calendared to improve adhesion and finish. Ideally the cathodes will be as thin as possible to make movement of the ions and electrons as fast as possible, however, thin coatings mean low loadings, and low total amount of energy storage per square inch of coating. It also important to make sure there are no pinholes or flaking in the coating as the charge carriers can be lost.

This leads to a very dynamic process of balancing coating thickness, ratio of components, slurry viscosity, and coating adhesion, which is why coating is often referred to as more of an art than a science, and requires patience. One large advantage of coating and punching out small disk electrodes in preliminary research is the potentially very thin coatings for good conductivity, and the consistency of the weight of the electrodes as doctor blade height is easily controlled. This allows for consistency between different electrodes in initial cycling and rate testing. This

was the method used for all final cycling data in this research. This method of electrode preparation is consistent with those proposed by Marks et al⁸⁴.

2.3.3.1.c Electrochemical Half Cell Assembly

The electrodes are assembled in a “T-cell” configuration for testing. The electrode is placed on an aluminum cylinder, and then a small membrane and a Celguard 2400 polymer separator are set on top of the electrode which is inserted into the plastic T (Figure 16).

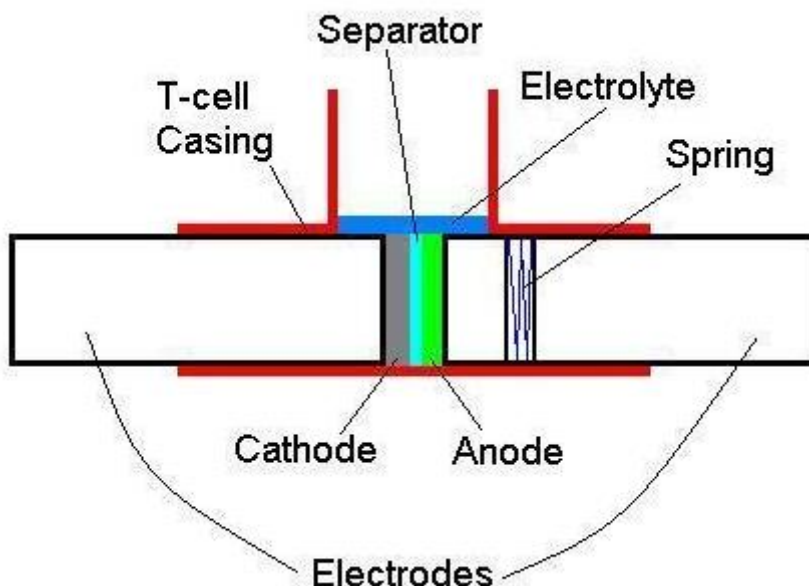


Figure 16: T-Cell configuration⁸⁵

A plastic nut is fastened over the aluminum rod to create an airtight seal. This is then dried and put in an inert atmosphere Argon glove box with an oxygen level less than 1ppm.

Once inside the glove box the negative electrode is assembled. A piece of lithium foil is punched out and cold-welded to a stainless steel current collector. Another polymer separator is place over the electrode and then inserted into the other side of the T. A spring is used to apply

pressure, forcing the two electrodes in contact with one another. One more plastic sealing nut is secured over the negative electrode.

Approximately 1 ml of 1M LiPF₆ electrolyte in a 1:1 ethylene carbonate to dimethyl carbonate solvent mixture is dropped in through the third opening in the T. This is just enough to wet the separators and allow for a little to pool at the top for absorbing over time. A sealed plastic nut is fixed on top and the T cell is ready for testing after a rest period.

2.3.4 Electrochemical Testing

The T-Cell configuration is a two electrode cell, in which the counter electrode is also the reference electrode. The cells are connected to an Arbin BT2000 galvanostat and tested in the desired voltage range at a current density of about 0.08 mA/cm². Galvanostatic cycling is a testing technique in which the potential is measured and a constant current is applied to the working electrode⁸⁶. In the case of this research the cells were tested between 4.5-2V.

The materials tested in this work were synthesized twice, the second time using higher purity precursors. This was done to ensure the composition is as close as possible to the stoichiometric values determined in the compositional diagrams. The capacities found during the first and second synthesis were very similar, and when comparing trends of the two compositional diagrams, the similarities speak to the repeatability of this work. Two compositions overlapped from the two systems, and averaged less than 10% difference. This is similar to what is expected in this type of research, with typical differences in repeated compositions between 5 and 10mAh/g. The majority of this error is believed to be due to the accuracy of the weighed out precursor values during material synthesis.

Chapter 3: Lithium Ion Battery Research

3.1 Lithium ion Battery Research Approach

This research was focused on creating a cathode material for lithium ion batteries that has a lower raw material cost than current commercial options, but offers increased specific capacity. A low cost and high performance cathode material does not exist today, however there are low cost cathode materials and high performance materials independently. By synthesizing a compositional combination of the low cost materials and the high performance materials, a lower cost and higher performance option is sought out. In order to combine desired characteristics, these materials should have similar crystal structures to reduce intra-phase stress, similar redox potentials vs. Li, and compatible synthesis conditions. If these criteria are met, this may enable homogeneous synthesis, structural integration with low stress and high stability, and good electrochemical performance. Four different materials were chosen that fit this criteria, and their individual strengths and weaknesses are as follows.

LiNiO₂

Strengths: This material has a layered type crystal structure and has symmetry following the $R\bar{3}m$ space group. The layered structure allows planar movement of lithium ions in and out of the material. The main attraction is a high theoretical capacity.

Weaknesses: Oxygen atmosphere synthesis and high precursor cost are major weaknesses of this material. Thermal stability is also an issue for this material and it can be a safety hazard when the battery is fully charged at elevated temperature.

LiCoO₂

Strengths: This is the most common cathode material for lithium ion batteries. It has a reasonable discharge capacity and shares the same crystal structure as the aforementioned LiNiO₂. Decent cycle life is also a benefit of this material.

Weaknesses: Cobalt is an expensive material, and so the cobalt precursors are expensive. Though this material has a high theoretical capacity, it only realizes about half of it because of an oxygen pinning, and low structural stability at high potentials.

LiNi_{0.8}Co_{0.2}O₂

Strengths: A solid solution of the above two materials, this composition has the same layered structure, a higher specific capacity, greater stability, and does not require an oxygen atmosphere during synthesis.

Weaknesses: With both Ni and Co precursors for this material, the precursor cost is high.

LiMn₂O₄

Strengths: This material has a stable 3 dimensional cubic structure, and belongs to the Fd $\bar{3}$ m space group. This is a different crystal structure than the previous 3 materials, however it has a similar oxygen sub-lattice. It has also been shown that manganese can be successfully doped into the layered structure described above. The three dimensional nature of this material is stable, and the lithium insertion and removal is through tunnels in the crystal. Lithium manganate also has much less expensive and more naturally abundant precursors, and will lower the cost of the composite as more is added. This material is easily synthesized with many different solid-state techniques and in different conditions.

Weaknesses: The specific capacity of this material is lower than all of the other materials mentioned. This material is also known to exhibit a phase change from cubic to tetragonal called Jahn-Teller distortion. This transition can be seen when cycling with a 3V redox couple, and is detrimental as it can cause capacity fade. This material is also known to degrade over time due to dissolution of Mn^{2+} into the electrolyte.

The crystal structure of the chosen materials in this research fit these criteria as they are formed under similar conditions, and have a similar oxygen sub-lattice. In order to map out and explore the different combinations of these materials and look for an optimized composition, ternary compositional diagrams are used. The first of which includes LiNiO_2 , LiCoO_2 , and LiMn_2O_4 . The first two materials have a layered type crystal structure and have symmetry following the $R\bar{3}m$ space group. These materials are chosen specifically because LiNiO_2 has a high specific capacity, and LiCoO_2 has good cycling stability. They also have redox couples that are at a similar potential vs. lithium. In combination, these materials have been shown to have improved performance over the individual end members. The third material, LiMn_2O_4 has a stable 3 dimensional cubic structure, and belongs to the $Fd\bar{3}m$ space group.

Taking these selected materials, ternary compositional diagrams are constructed. The first of which is called the standard system and can be seen in Figure 17. This system is very basic and easy to read, and essentially as one follows toward each corner of the diagram the amount of Ni, Co, and Mn varies directly.

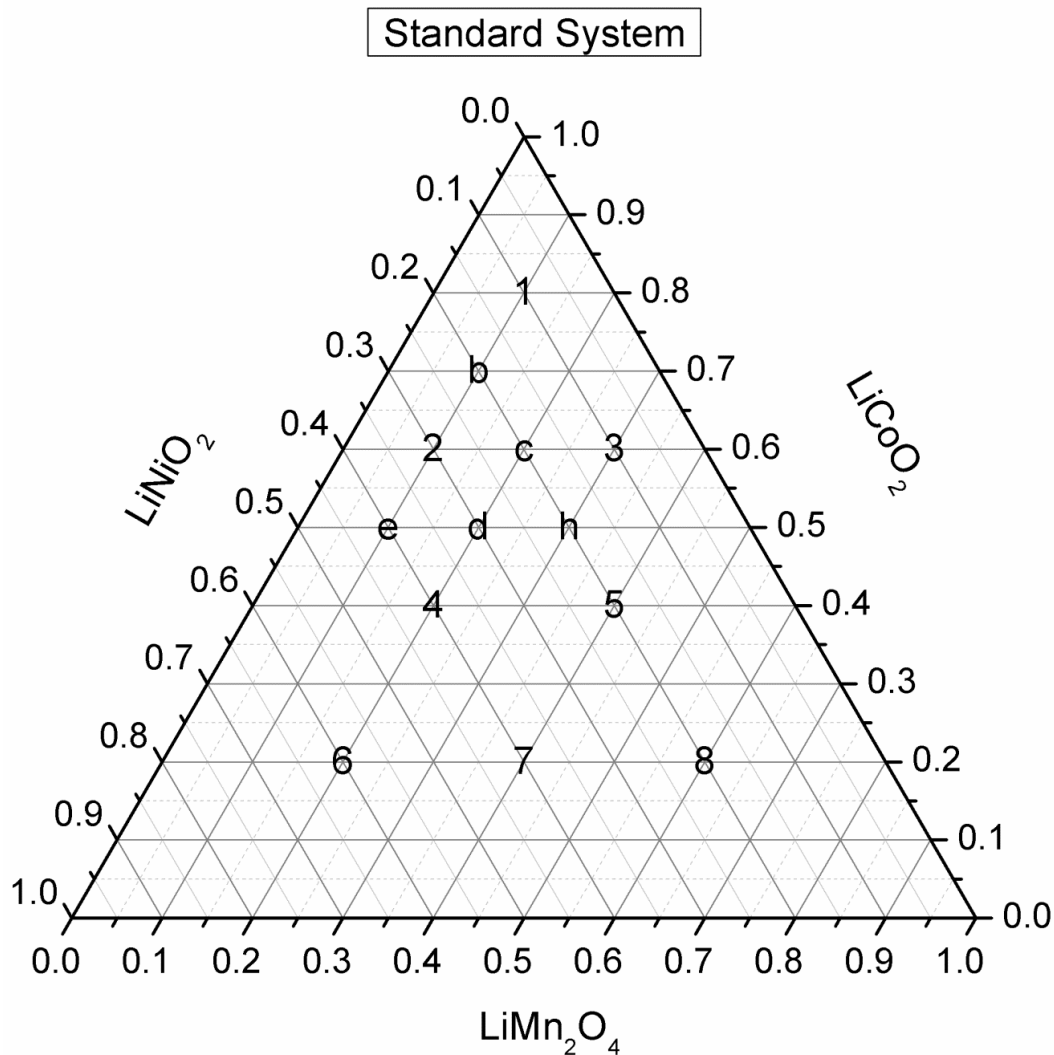


Figure 17: Compositional Diagram for Standard System

Note that the bottom right corner is LiMn_2O_4 , so there is more manganese in each sample than a one to one ratio. The numbers on the interior of the diagram are the initial compositions explored in this work. When these samples were tested electrochemically, the sample with the highest specific capacity was found to be number 2. With this information, compositions around that sample were tested, but only ones that contain all three components. This means points that would lie on the straight line between two of the three compounds were not explored

as they would not serve the purpose of this work. The compositions explored are represented by letters on the diagram, in this case b, c, d, e, and h.

The second compositional diagram follows the same basic format as the first one, and shares both LiCoO_2 and LiMn_2O_4 as end members, but the third end member is changed. For this diagram the third component chosen is $\text{LiCo}_{0.2}\text{Ni}_{0.8}\text{O}_2$. This replaces LiNiO_2 because its synthesis conditions are more similar to the other two members, and does not require an oxygen environment. This system is called the stabilized system because in the region of the diagram close to that component the nickel compounds should still form. Basically you can create all three end members for this compositional diagram under the same conditions, so it was dubbed the stabilized system, and is shown below in Figure 18.

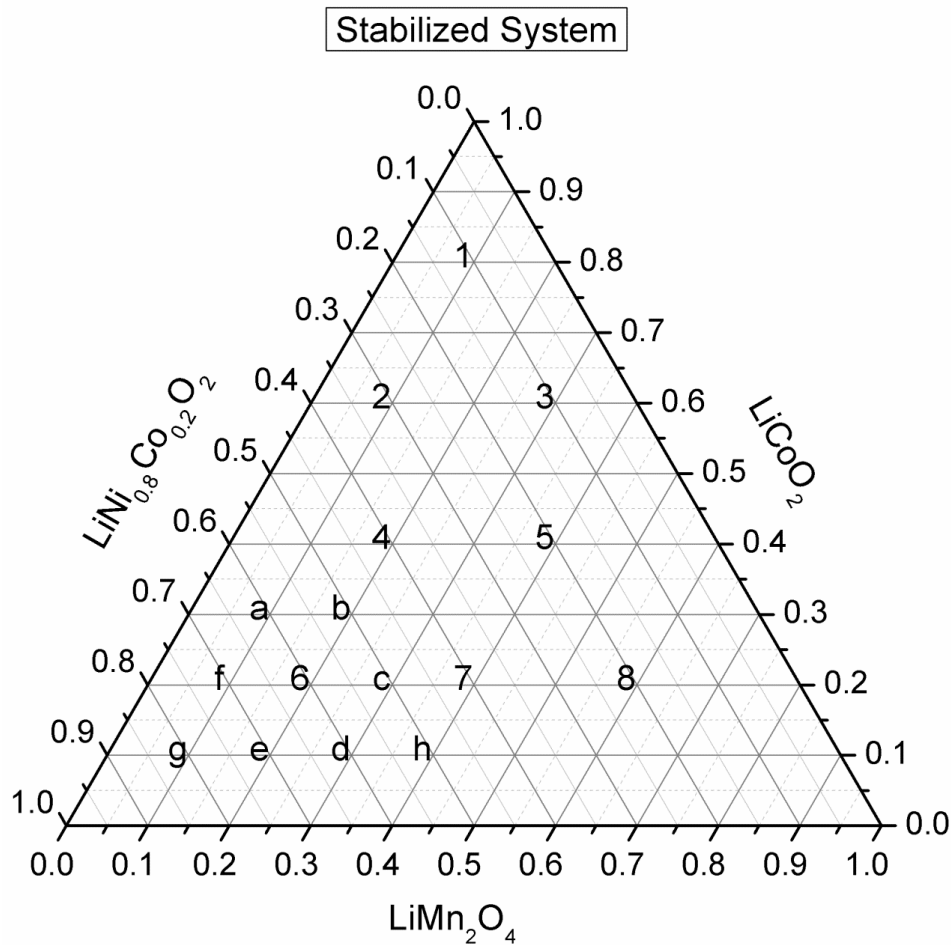


Figure 18: Compositional Diagram for Stabilized System

The initial eight compositions synthesized and tested are also numbered on the diagram 1-8, with the highest specific capacity member being 6 in this case. Letters a-h are the subsequent 8 compositions tested around this point to try and find a higher capacity composition.

3.2 Results/Discussion

The results for this section are extensive, and contain many compositions from two different systems of materials, so for clarity only the compositions of interest are included in the following text, and the remainder can be found in appendix 1 for reference.

3.2.1 Electrochemical

The electrochemical testing of these samples was conducted in a t-cell two electrode configuration using coin type electrodes. The samples were cycled galvanostatically and the specific discharge plots were used to initially characterize and evaluate the samples, and a table of these values can be found in appendix 1. These plots show voltage as a function of specific capacity. Specific capacity is actually a calculated value based on the constant current of the setup, time at that current, and the weight of the active material in the cathode. These plots are useful in that they show the discharge capacity of the material and how much of it occurs at each voltage. The voltages where the plot has a very small slope represent the redox couple that is active during that part of the cycle. It can be difficult to see at what voltage the redox couple occurs with gradually sloping profiles, so by plotting 1/derivative of the specific discharge profile the redox couples can be represented as spikes, which are much easier to pick out. This type of plot is described in detail the literature and is called a differential capacity plot⁸⁷⁻⁸⁸.

In order to visualize how the composition affects the specific capacity of these compounds contour plots were made overlaid on top of the ternary diagrams. For the standard system the squares represent the samples tested (Figure 19).

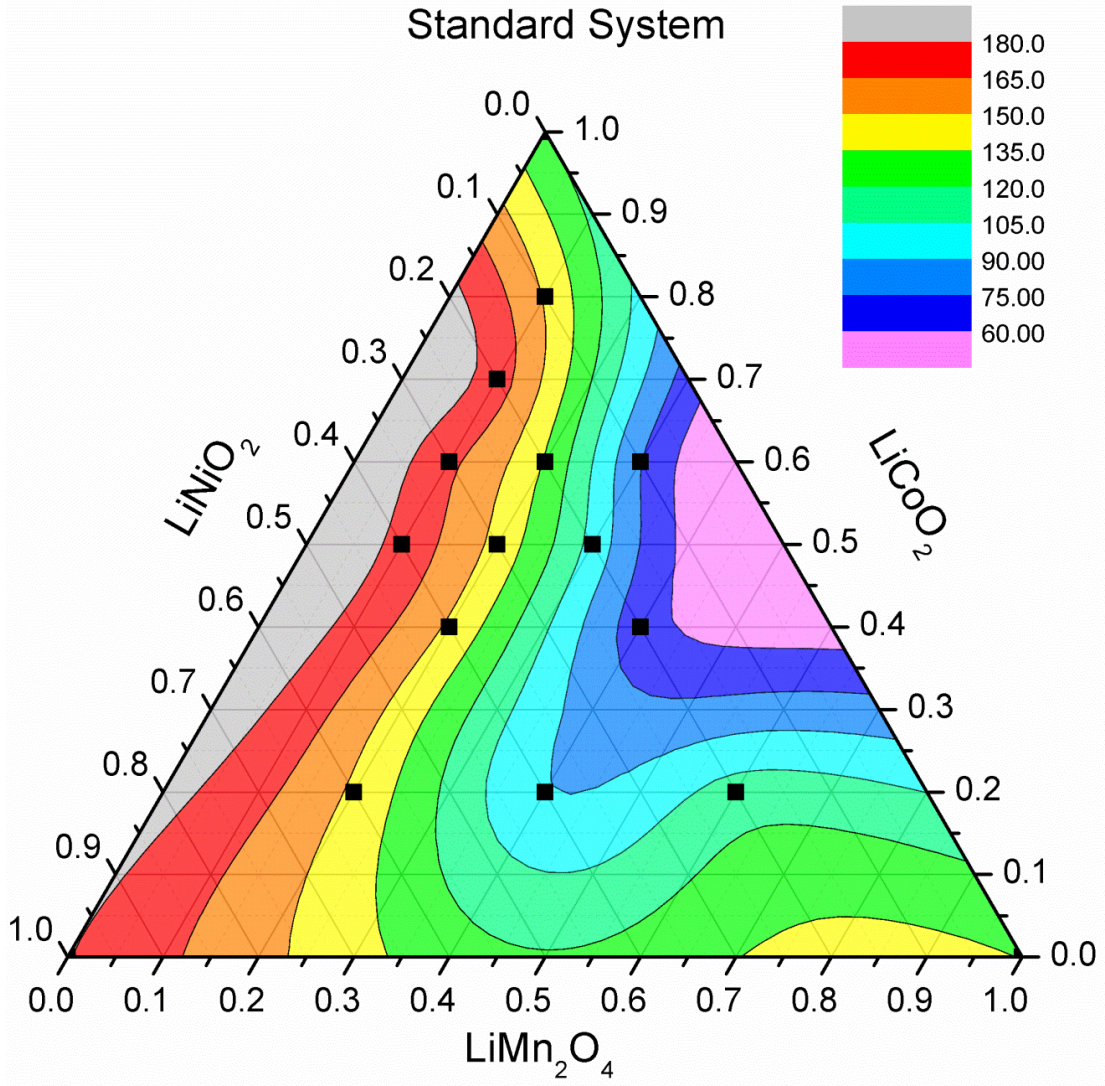


Figure 19: Standard System Specific Capacity Contour Plot (mAh/g)

A similar diagram was created for the stabilized system, however stars represent the compositions tested (Figure 20).

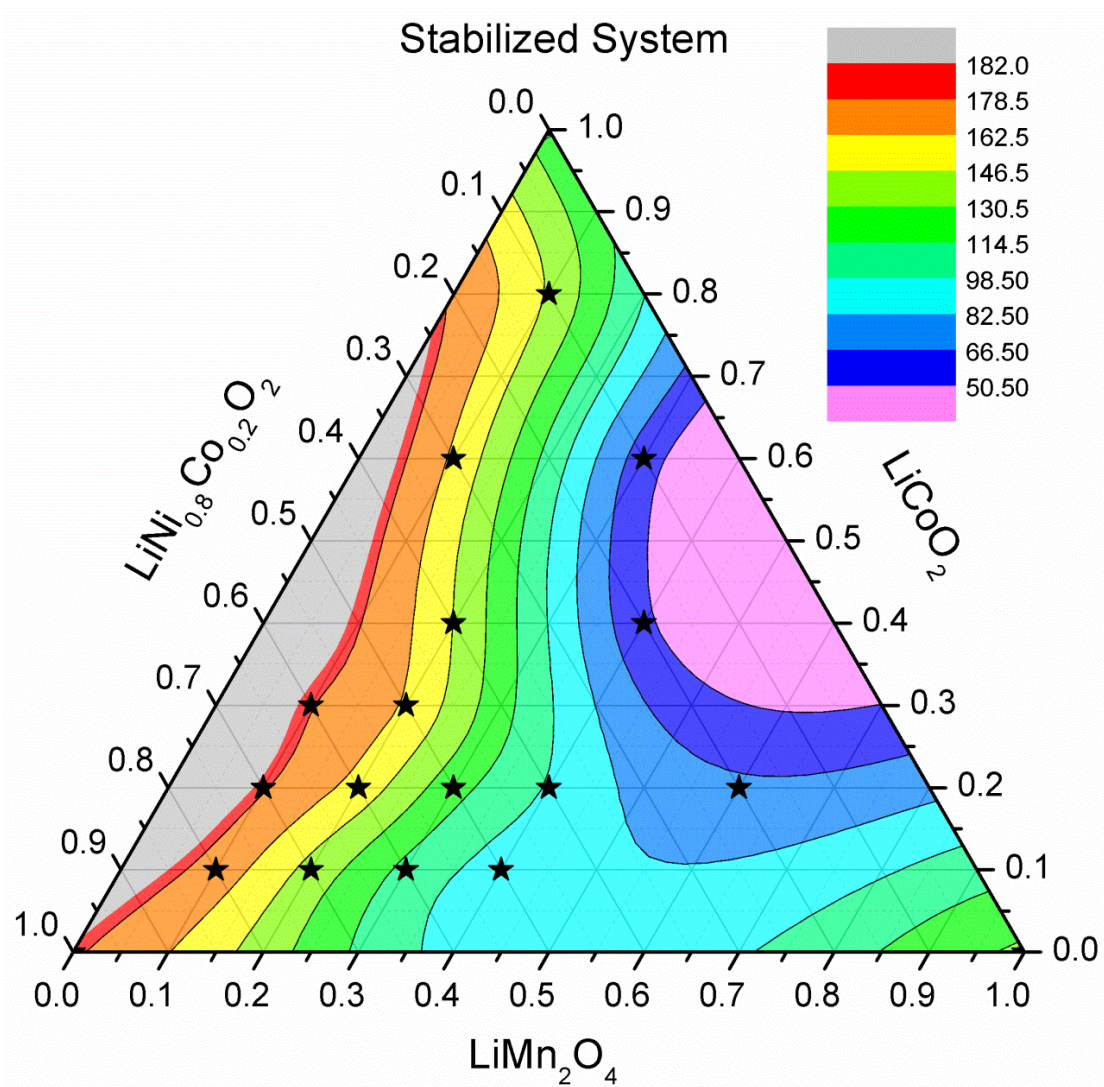


Figure 20: Stabilized System Specific Capacity Contour Plot (mAh/g)

To further compare these results the compositions for the stabilized were converted into the standard system format and then overlaid on top of the standard diagram. The same markers were used on this plot to indicate what compositions are tested and where they are on the composition map (Figure 21). Note that two of the compositions overlap coincidentally.

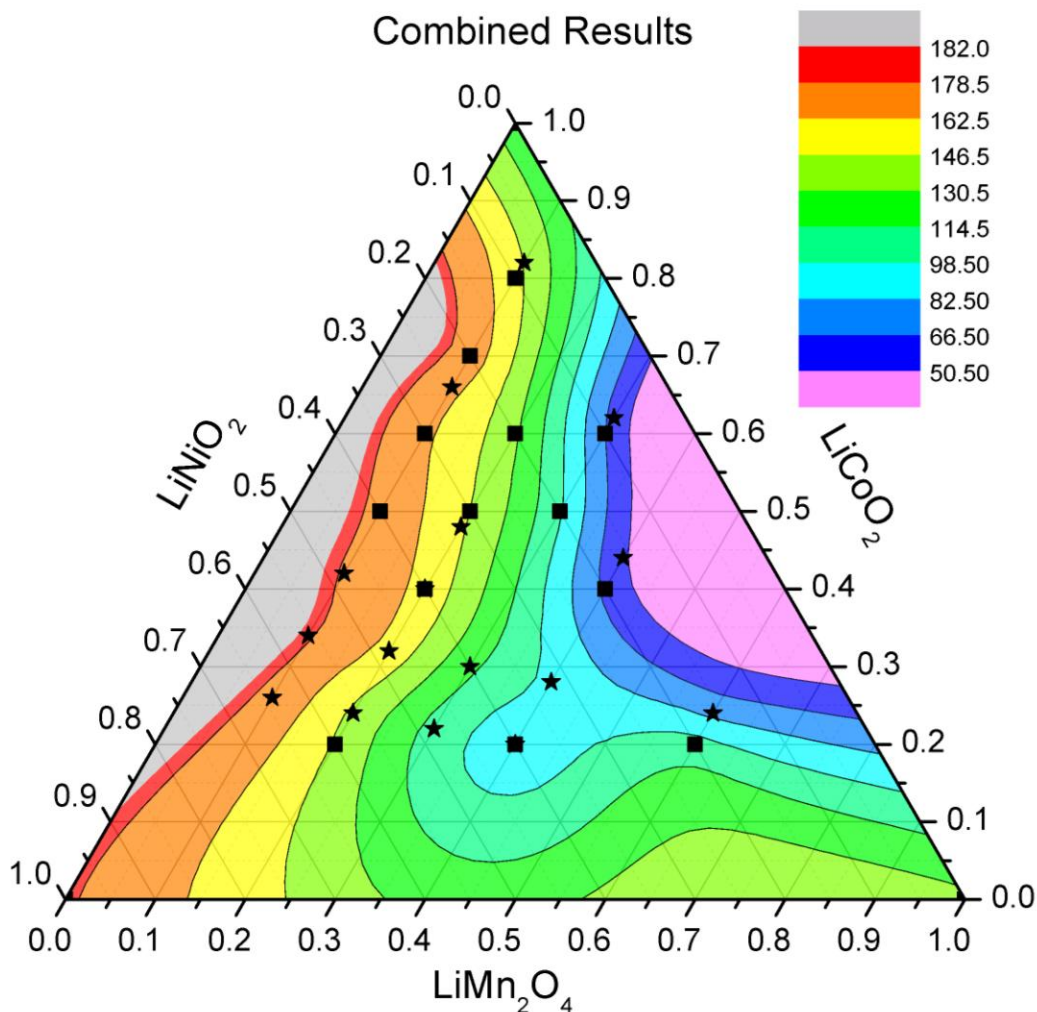


Figure 21: Overlaid Specific Capacity Contour Plot (mAh/g)

The specific capacity plots for the highest specific capacity compositions for both the standard and stabilized system are given below in Figure 22 and Figure 23 respectively. For comparison of the profiles, the lowest specific capacity compound specific capacity plot is also shown in Figure 24.

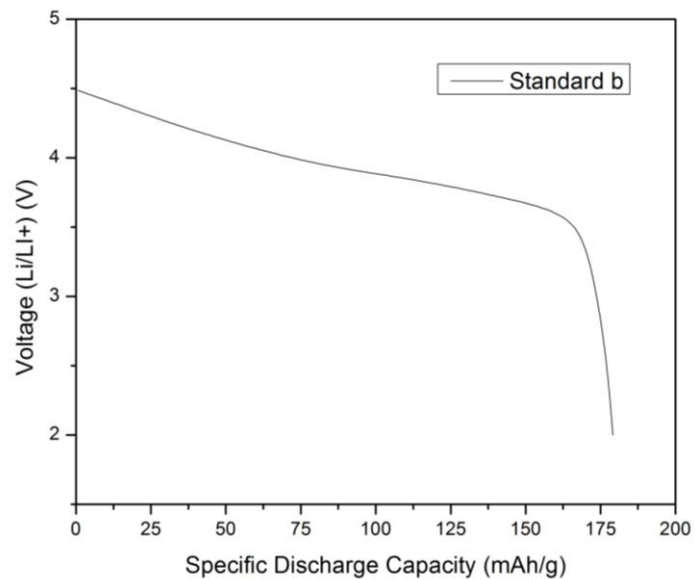


Figure 22: Specific Capacity Plot for Composition b in the Standard System

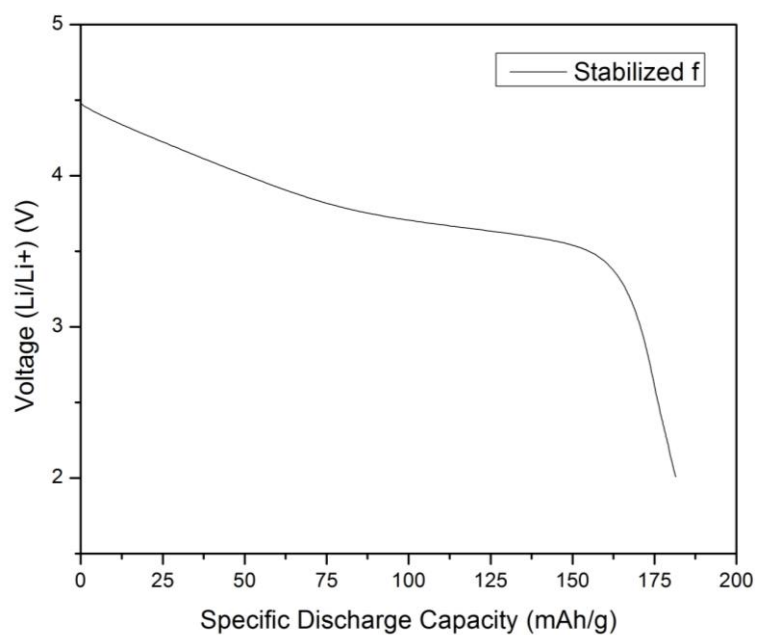


Figure 23: Specific Capacity Plot for Composition f in the Stabilized System

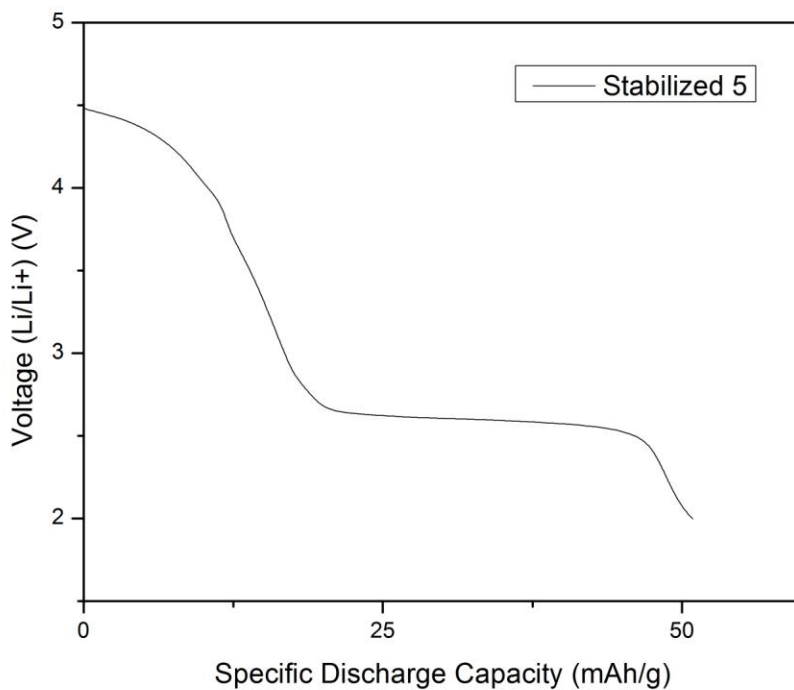


Figure 24: Specific Capacity Plot for Composition 5 in the Stabilized System

Note that Figure 24 has a much different profile than both Figure 22 and Figure 23, with two distinct plateaus at potentials characteristic of Jahn-Teller distorted LiMn_2O_4 . To point out more clearly where the redox reaction is occurring for each of these compounds a differential capacity plot is included below (Figure 25-Figure 27).

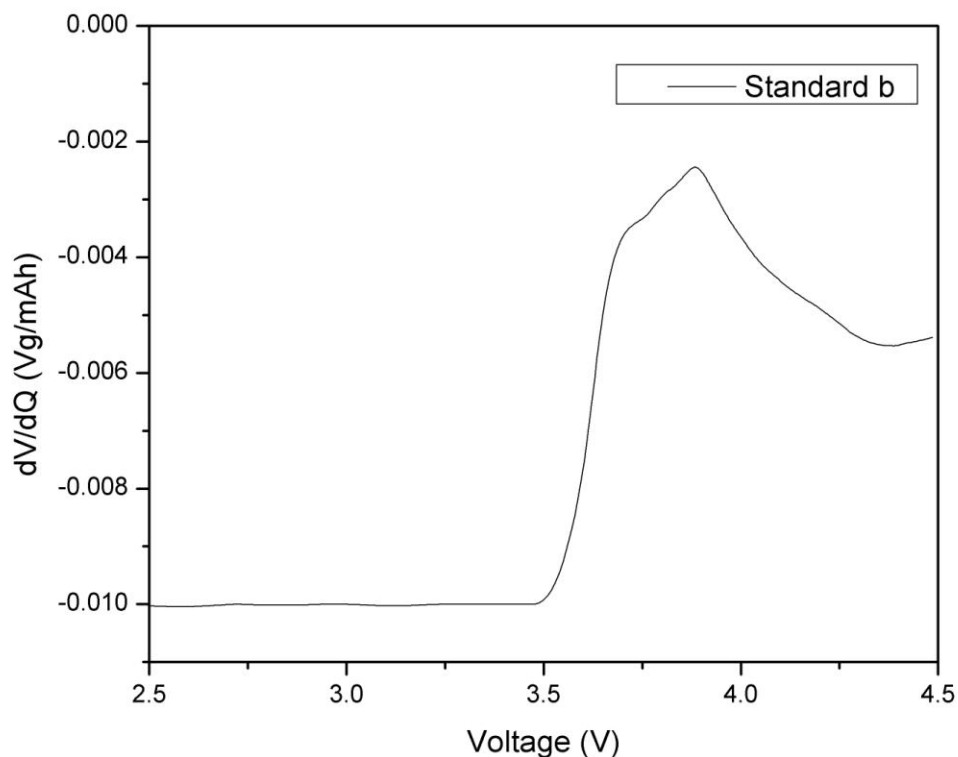


Figure 25: Differential Capacity Plot for Standard System Composition b

The above figure shows peaks around 3.7 and 3.9 V vs Li/Li^+ , but also shows the start of another peak at 4.5 V, which is actually characteristic of extraction of Li_2O from the rocksalt structured Li_2MnO_3 . This phase was not anticipated, however due to careful characterization and high resolution data, it is actually identified in the following in the synchrotron XRD performed and illustrated in the following section.

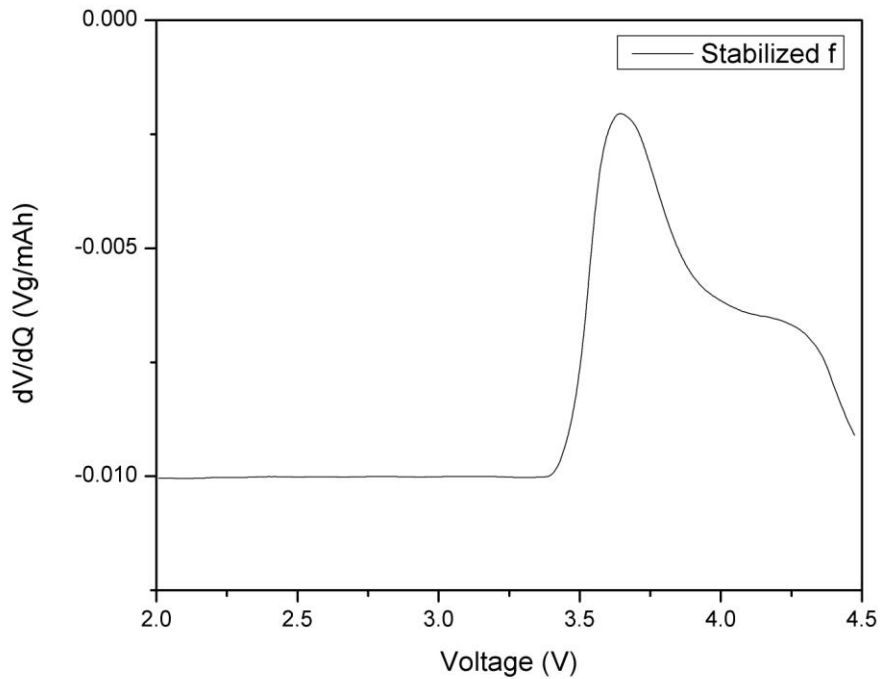


Figure 26: Differential Capacity Plot for Stabilized System Composition f

This differential capacity plot is very characteristic of a layered NMC material with reactions occurring between 3.7 and 4.2V vs Li/Li⁺.

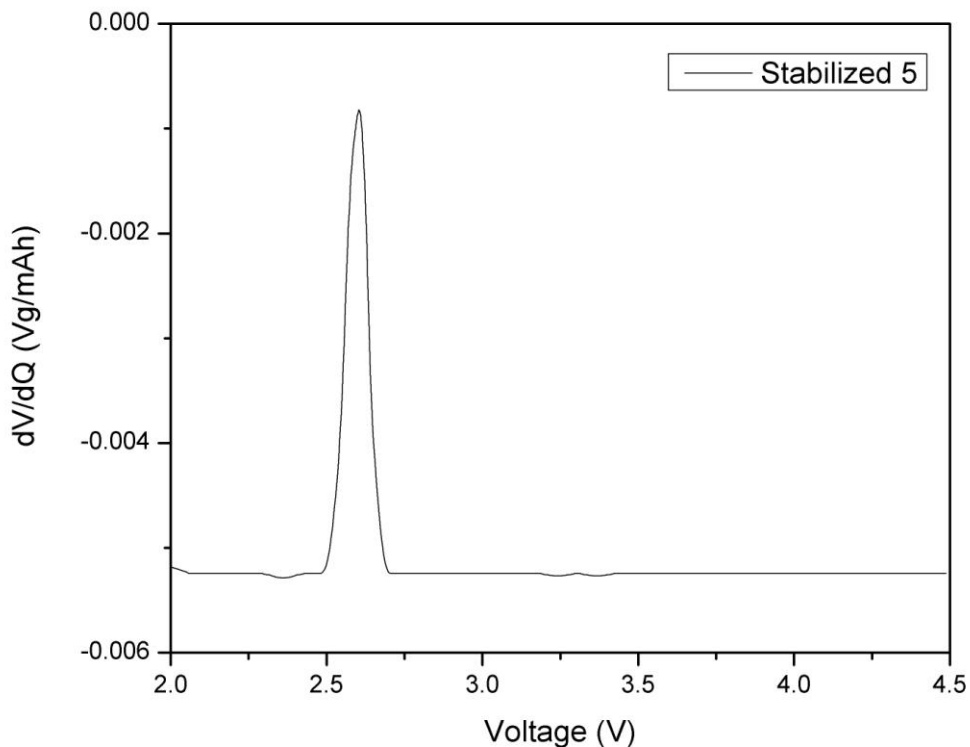


Figure 27: Differential Capacity Plot for Stabilized System Composition 5

Note that the very apparent and sharp peak at about 2.6V, which shows that nearly all of the capacity for this cell is coming from Jahn-Teller distorted lithium manganate. These electrochemical results can actually be explained based on the crystal structures found in the following section.

3.2.2 XRD Characterization

Initial powder diffraction on a lab scale powder diffractometer was performed in order to identify initial phases present and to ensure initial phase formation post synthesis. Samples identified for further structural refinement are sent to Argonne National Labs Advanced Photon Source (ANLAPS) for high-resolution synchrotron powder diffraction. The high resolution and low noise data that is obtained by synchrotron XRD makes identifying split peaks and low

intensity peaks missed by the lab scale diffractometer possible. High quality data is critical to obtaining the most structural information possible through Rietveld refinement. The standalone scans for the compounds sent to ANLAPS converted to $\text{CuK}\alpha$ wavelength can be seen in Figure 40 in appendix 1 for reference. They are converted to $\text{CuK}\alpha$ in this plot for easy comparison to typical scans in the literature for these compounds. The scans used in the Rietveld refinements remain in the specific wavelength of the powder diffraction line at ANLAPS.

The Rietveld refinement done in this work begins by comparing the raw scan with the standards for the likely phases present. Using these phases, a basic structural model is created. Instrument parameters are refined starting with a file provided by ANLAPS on a standard LaB_6 sample from the specific beamline used for the samples in this work. Locking these down helps to ensure the peak shape and position is due to structure not equipment. When fitting the data the phase with the highest symmetry is always tried first, because a lower symmetry phase has more peaks and can often overlap the higher symmetry phase making it difficult to extract the contributions from each. These refinements are given below.

The first refinement is of standard system composition b. After an initial Le Bail fit it is apparent that this composition is actually composed of 3 phases. The majority of the large intensity peaks are characteristic of the layered phase, which is evident by the 10 and 19.7 degree peaks, which are unique to this phase. The spinel phase differentiating peak around 8 degrees is evident and so that phase is added to the model. These first two phases are the layered and spinel phases that are anticipated from the end members of this system. The third phase is the rocksalt phase that is characteristic of Li_2MnO_3 . With the high-resolution data obtained from ANLAPS the shoulders of the 11.7 degree and 16.5 degree peak are attributed to this phase, so this phase is also added to the model. The plot showing the three models applied to the raw data is shown

below in Figure 28. Red dots are the raw data, black lines represent the model, and the blue line represents the difference. Blue lines are for the layered phase peaks, red lines are for the rocksalt phase, and green peaks are for the spinel phase.

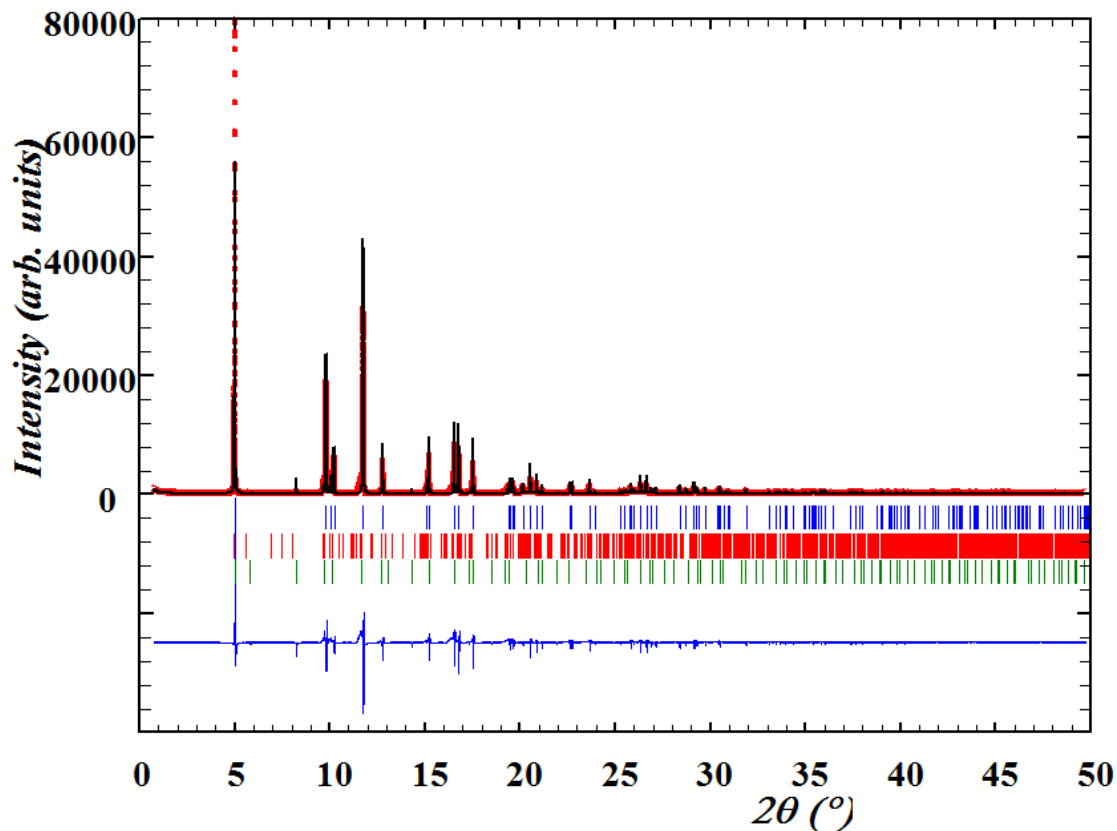


Figure 28: Rietveld Refinement of Standard Composition b

With three phases, one of which being a low symmetry phase, a full atomic refinement is not feasible on this material. The Le Bail fit identified all of the peaks with only minor discrepancies illustrated by the blue line at the bottom of the plot, and yielded a global $\chi^2=24.2$. This is not a bad value considering the complexity of the sample. For reference, samples that have good crystallinity and one phase can often be refined to a χ^2 of around 10.

The second refinement is of stabilized composition f. This refinement included the R-3m layered phase as none of the characteristic spinel and rocksalt phase peaks were present at 8 and 6 degrees respectively after the initial Le Bail fit. With only one phase identified the atoms are assigned at the standard Wyckoff positions for this layered material initially, which is Li at 3a, Ni Mn and Co at 3b, and O at 6C. A disorder model is then applied following the model suggested by Lu et al which suggests that the lithium and nickel can have partial occupancy the 3b and 3a Wyckoff positions respectively⁶⁷. This model provides a better fit for this material, but only contained a small percentage of each disordered ion. The plot for this material is in Figure 29. The peaks for the layered phase are represented in blue. The global χ^2 for this fit is 13.2.

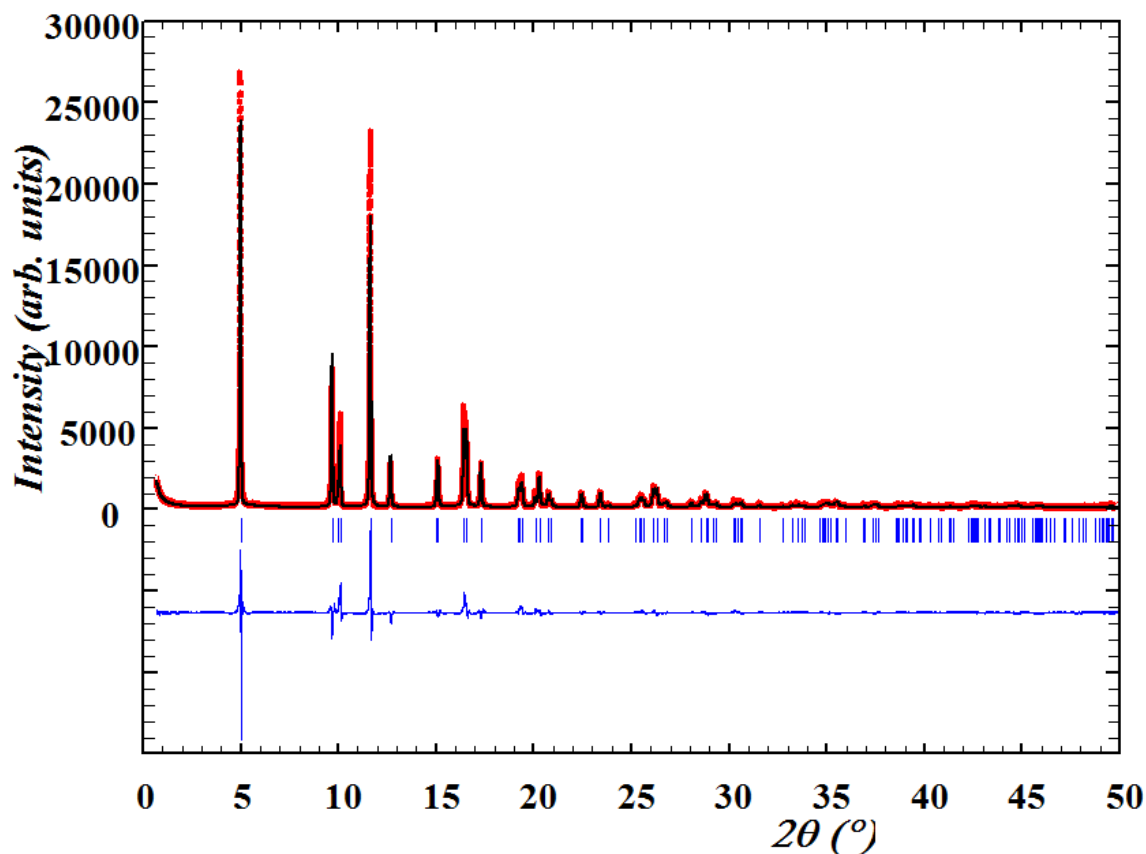


Figure 29: Rietveld Refinement of Stabilized Composition f

A summary of the refinement parameters is given below in Table 1.

Table 1: Refinement Results for Stabilized System Composition f

Phase	Element	Site	x	y	z	Occupancy
R $\bar{3}m$ Layered	Li1	3a	0	0	0	.082
	Li2	3b	0	0	.5	.001
	Ni1	3b	0	0	.5	.026
	Ni2	3a	0	0	0	.001
	Mn	3b	0	0	.5	.027
	Co	3b	0	0	.5	.027
	O	6c	0	0	.24	.167

The final refinement is for stabilized composition 5. This refinement is interesting as it is of one of the worst performing samples, and is needed to identify what makes the good compositions perform at a higher level. Contrary to the previous two samples, this material seemed to be dominated by the spinel phase. In addition to this difference, the rocksalt phase shows a much stronger presence with a higher intensity of the 6 degree peak. The overall refinement is seen below in Figure 30, with the rocksalt phase peaks in blue and the spinel phase peaks in red.

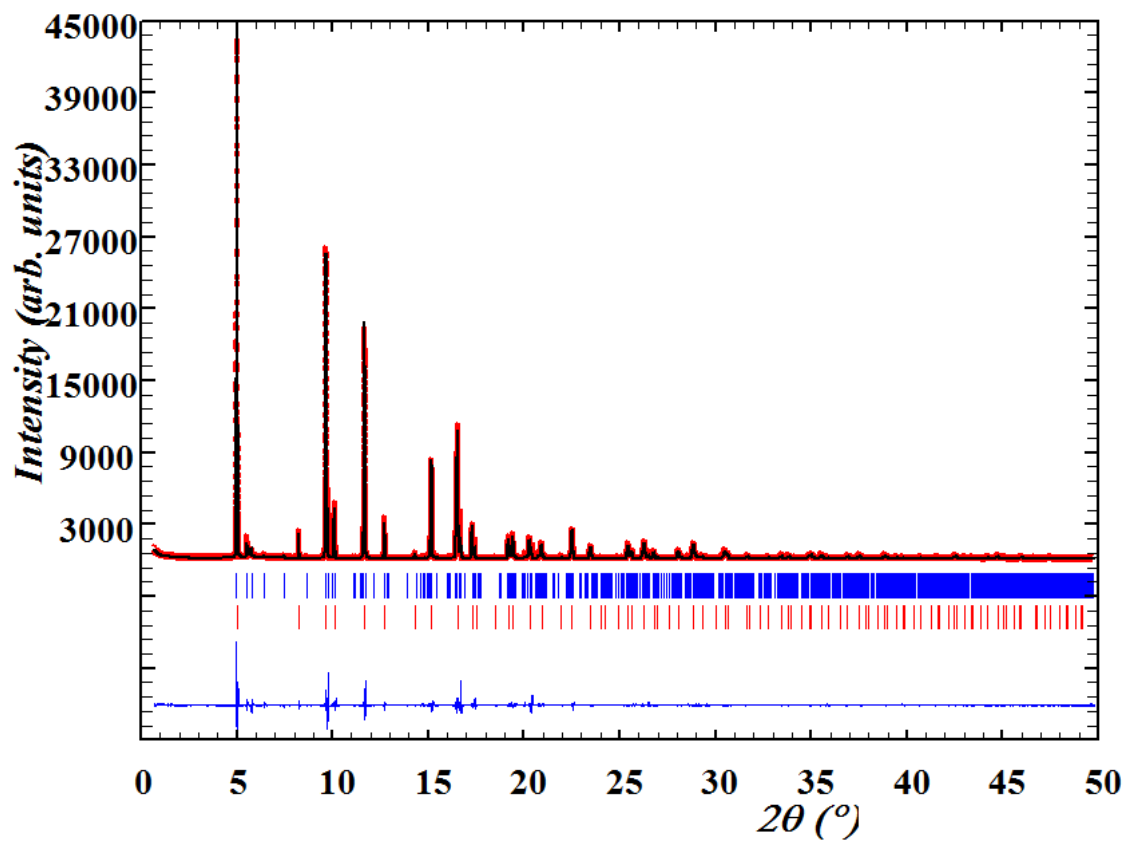


Figure 30: Rietveld Refinement of Stabilized Composition 5

A zoom of the peaks between 4.7 degrees and 10.7 degrees shows clearly the 6 degree peaks characteristic of the rocksalt phase, as well as a split primary peak at 5 degrees (Figure 31).

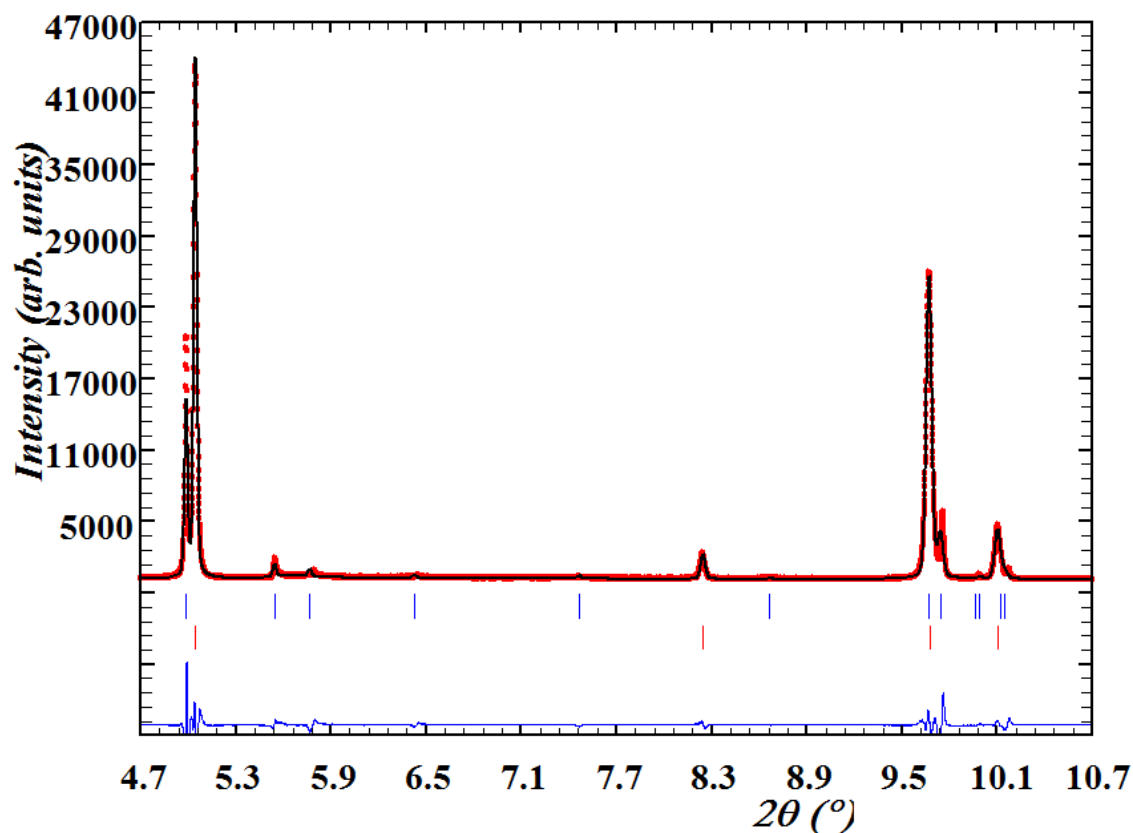


Figure 31: Zoom of Low Angle Reflections in the Rietveld Refinement of Stabilized Composition 5

Note that atomic refinement was not performed on this sample for the same reasons as the first sample. The global χ^2 for this fit is 8.3. When this is correlated to the differential capacity for this material it follows the logic that if the Li_2MnO_3 and LiMn_2O_4 phases are both present, the average oxidation state of the Mn in the spinel phase would be dominated by Mn^{3+} since all the manganese in the rocksalt phase is likely to be Mn^{4+} . Abundance of the Jahn-Teller active Mn^{3+} can potentially explain the large percentage of the total capacity occurring at the 3V redox reaction, as is evident in Figure 27. The remaining Co and Ni are likely in the spinel phase, and the redox reactions for those ions are not seen as their redox couples in this structure occur above 4.5V vs Li/Li^+ . Disorder has been seen for transition metal doped spinel before, so partial

occupation of the tetrahedral sites in the spinel by the cobalt and nickel ions could explain the low capacity.

3.2.3 XPS Characterization

The next step in understanding what makes factors make the high capacity materials perform well is understanding what redox reactions are present. By developing good models for the structure with the Rietveld refinements, these same compounds that are reported in the previous section were characterized using high resolution XPS. These scans showed the binding energies for each of the elements present in the material. By doing a spectral deconvolution, the relative amount of each oxidation state for Mn, Ni, and Co is found using known possible oxidation states for each metal and binding energies from the literature^{23,89-90}. The plots showing the deconvolution of the XPS peaks can be seen below in appendix 1 Figure 41-Figure 49.

An overlay plot of the XPS patterns for cobalt ion for the same samples described in the XRD section show only a very slight shift in binding energy with varied composition (Figure 32). In this plot the green line corresponds to sample stabilized 5, the blue line is stabilized f, and the red is standard b.

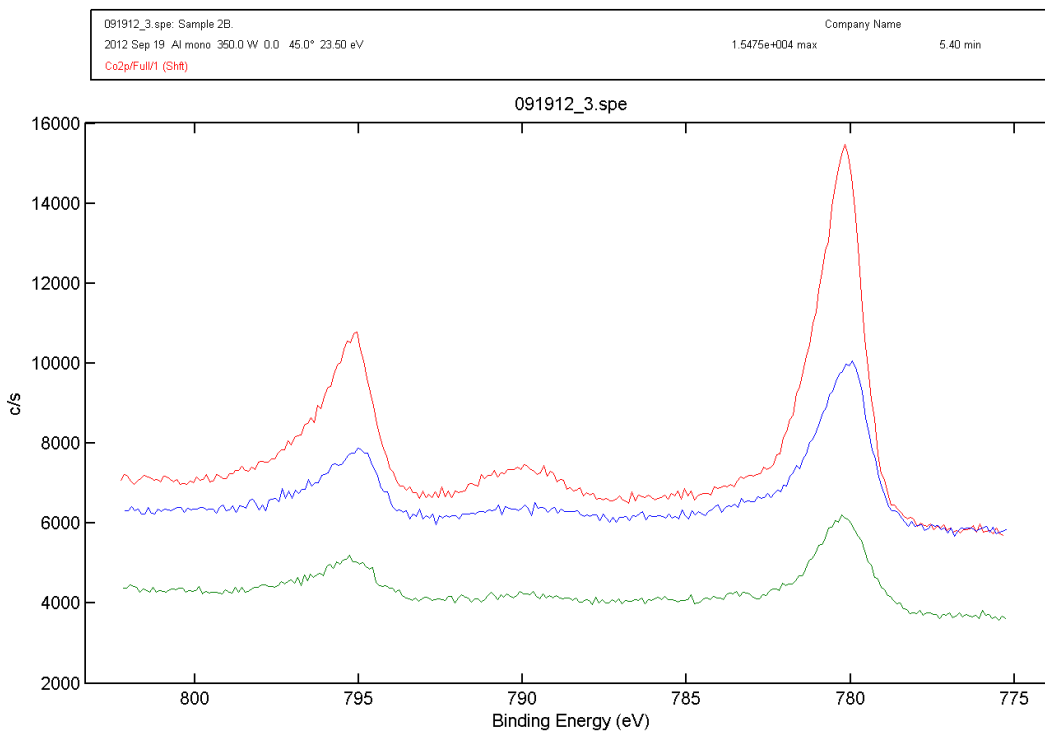


Figure 32: Cobalt XPS overlay

The spectral deconvolution for each element does not show a large change in apparent percentage of each oxidation state from between the different compositions (Figure 41-Figure 49). All samples seem to be mixed valence in nature based on the broad nature of the major peaks, spanning the binding energy range of multiple oxidation states. This is consistent with what would be expected from the compositions and phases of each compound.

3.3 Lithium Ion Battery Summary

Two compositional diagrams were used in an attempt to find a high capacity cathode material with a lower precursor cost. These materials were tested galvanostatically in a half cell configuration to determine their specific capacities. These specific capacities were mapped on the compositional diagrams using contour plots to show trends based on composition. They were also characterized using XRD, XPS, and differential capacity plots to determine the crystal structures, oxidation states, and apparent redox couple potentials vs Li to determine the major mechanisms causing these trends.

When comparing the compositions across the two compositional diagrams used in this work, the trends in specific capacity are very similar. Compositions closer to the layered end members of the diagrams have a higher specific capacity. The crystalline phases present in these materials seem to follow the same trend with higher capacities having a higher percentage of the layered structure. A rocksalt structure typical to Li_2MnO_3 appears in the both the compositional diagrams at varying compositions as well. The worst performing sample is dominated by spinel structure, and exhibits a massive Jahn-Teller distortion indicative low 3V peak in the differential capacity plot.

Chapter 4: Hydrogen Storage Materials Background and Research

4.1 Purpose and Aim of Research

The second energy storage technology addressed in this work is the storage of hydrogen fuel in solid-state chemical hydrides. Hydrogen is a very energy dense material and can provide an excellent method of storing and transferring energy. This energy storage method first requires the creation of hydrogen gas generally through electrolysis or the refinement of fossil fuels⁹¹. This fuel can then be converted back into electrical or mechanical energy by combustion in an engine or through conversion to water in a fuel cell. The storage of the hydrogen is the limiting factor at this point. The main ways that hydrogen is stored today is in pressure vessels and cryogenic tanks, both of which have low energy storage densities relative to gasoline. There are two major categories of hydrogen storage researched today including adsorption materials, absorption materials. Both of which have their own issues depending on the specific media and composition as detailed later in this section.

One of the more promising material groups are the complex chemical hydrides. The reason they are promising is they have high volumetric and gravimetric storage densities. They suffer, however, from low efficiency due to not releasing all of the stored hydrogen. If this is remedied however, this class of materials could become a viable solution to hydrogen storage⁹². Because of this large upside, this was the issue addressed in this work. The purpose and aim of this research was to increase the amount of hydrogen released from the complex hydrides in an attempt to increase the viability of hydrogen as a fuel.

4.2 Hydrogen Introduction

4.2.1 Definitions

There are a couple of terms and metrics used in this work that are typical to the hydrogen storage field, and are not necessarily intuitive. Hydrogen storage capacity is a term used to describe the amount of hydrogen stored per weight of storage media, and is measured in weight percent $\frac{g H_2}{g H_2 + g \text{ sample}}$. A different metric used is storage density, which is measured in Hydrogen atoms per unit volume, commonly H atoms/cm³. These are very valuable in determining the actual viability of a storage method, as they are independent of storage media type, and provide a direct comparison of performance⁹³.

4.2.2 Design Considerations

Hydrogen storage metrics for mobile applications are quite similar to those used in batteries, however they differ in that acceptable values have been laid out by the US Department of Energy in order to determine if a technology is viable, and to give researchers clear goals⁹⁴⁻⁹⁵. The majority of these goals are system level, including the storage container, valves, and any temperature control necessary to enable the storage technology.

In this work the storage material itself is the focus, not the supporting hardware, so the same general metrics are used, but they are applied to the material alone, which is consistent with other literature in this area. These metrics include both gravimetric and volumetric storage density, hydrogenation and dehydrogenation rates, total number of cycles to failure, and cost⁹⁶. This work focused on improving the realized gravimetric storage capacity as described in the previous section.

4.2.3 Current Storage Systems

The storage of the hydrogen fuel is a difficult task and currently is done using high pressure or cryogenic tanks, neither of which is viable in mobile applications. High pressure hydrogen storage vessels need to be several times larger in order to carry a comparable amount of fuel to a gasoline equivalent, and can be dangerous because of risk of explosion as the storage pressure ranges from 5-10kpsi. These pressure vessels are typically an advanced carbon fiber composite material, and require internal temperature monitoring while being filled. There also is an appreciable amount of energy lost in the act of compressing this gas⁹⁶.

Cryogenic liquid hydrogen tanks are large, heavy, and require constant power to maintain the cryogenic conditions. Though its density is greater than that of compressed hydrogen gas, it still requires more volume than gasoline for equivalent energy, excluding the external systems necessary to maintain the environment. A 20°C environment is necessary to maintain hydrogen as a liquid, and as the liquid boils, it is vented to atmosphere to prevent excess pressure build up, and is lost. It also requires a large amount of energy to produce the liquid hydrogen initially, roughly 3 times that of 10kpsi compressed hydrogen⁹⁶.

Storage of the hydrogen with high surface area adsorption materials is another area of study. Adsorbing of the hydrogen gas on the surface of materials with a high surface area occurs under pressure at elevated temperature, and then releasing the hydrogen by increasing the temperature of the material⁹⁷⁻⁹⁸. The materials also require storage at low temperatures (77°K) in order to limit the slow release of hydrogen.

Storing hydrogen in the bulk material has a higher theoretical storage capacity, and has many forms⁹². Absorption materials such as metal, complex, and chemical hydrides decrease the

amount of pressure needed for hydrogen storage, and increase the storage density per volume, however these materials are not optimized as with a wide variety of issues from release temperature to stability and inefficiency.

4.2.4 Recent Developments

There has been a lot of research recently using metal hydrides, in which the hydrogen absorbs into the crystal lattice of the metal, creating primary bonds with the material and forming a new phase. The hydrogen gas is then released by increasing the material temperature, or by chemical reaction of the hydride with another material such as water or ammonia. One of the more promising examples of metal hydrides is MgH_2 . This material has relatively high theoretical gravimetric and volumetric storage densities of 7.6 wt% H_2 and 110 $\text{kg H}_2/\text{m}^3$ respectively^{91,99}.

4.2.5 Relevant Material Research Survey

4.2.5.1 Alanates

Alanates, also referred to as complex aluminohydrides, are very attractive as hydrogen storage materials because of their relatively high gravimetric hydrogen density¹⁰⁰. The background of the three alkali alanates relevant to this work is discussed in this section. These compounds are nonmetallic with calculated band gaps ranging from around 2.5 to 5eV. The thermal dehydrogenation of these compounds has been shown to be stepwise in nature¹⁰⁰.

4.2.5.1.a LiAlH_4

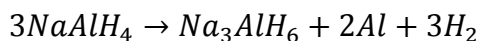
LiAlH_4 is one of the most attractive of the alanates as it has the lowest molecular weight. The thermal dehydrogenation process for this compound as an example of the stepwise nature is as follows Equation 1-3¹⁰¹⁻¹⁰².

Equation 1**Equation 2****Equation 3**

Though this material has a high theoretical gravimetric hydrogen storage density, it suffers from slow kinetics and a high temperature of desorption¹⁰³⁻¹⁰⁴. Several groups have tried to overcome these kinetics through use of catalysts¹⁰⁵⁻¹⁰⁸. The most prevalent catalysts are TiCl₃ and AlCl₃. These have been shown with moderate success in lowering the temperature at which hydrogen is released from the compound¹⁰⁹, and slightly increasing the yield of hydrogen from the material¹⁰⁸. The intermediate compound Li₃AlH₆ is widely researched as a hydrogen storage material. A variety of catalysts have been used to try to improve the hydrogen release of this material as well¹¹⁰⁻¹¹³.

4.2.5.1.b NaAlH₄

This compound is similar to LiAlH₄ in many ways. It has a relatively high theoretical hydrogen storage capacity of 7.5wt%, only lower because of the different alkali metal atomic weight. NaAlH₄ and also has a stepwise thermal dehydrogenation process and it goes as follows^{101,114}.

Equation 4**Equation 5****Equation 6**

Slow kinetics also plague this material, not allowing it to realize its full theoretical capacity. The effect of catalysts has also been attempted with some success using NaAlH₄ and Na₃AlH₆ and using a variety of catalysts including Al₃Ti¹¹⁴, Ti¹¹⁵⁻¹¹⁶, Zr¹¹⁷, LaCl₃^{105,109}, TiF₃ and TiCl₃¹¹⁸. Another compound in this family that has been studied is LiNa₂AlH₆, which has an attractive theoretical capacity, but suffers from the same slow kinetics as the other alanates. This material has been shown to be synthesized using mechanochemical synthesis as well¹¹⁹.

4.3 Hydrogen Storage Experimental Methods**4.3.1 Material Synthesis**

The synthesis method used on all samples in the hydrogen storage research described in this dissertation was mechanochemical synthesis. This is a relatively new technique that is very popular in the literature. This method uses a high intensity ball mill to violently shake a stainless steel vial sealed with an o-ring and screw cap. The vial contains the precursor material for the compound and stainless steel balls of varying sizes. The kinetic energy of the balls is transferred to the material as it is mixed and with time the phase new phase forms. All compounds in this research started with either LiAlH₄ or NaAlH₄, and were then milled with a stoichiometric amount of either LiH and/or NaH in order to form the final phase. The amount of ball milling

time varied for each desired phase, from 3hr for Li_3AlH_6 to 56hr for $\text{LiNa}_2\text{AlH}_6$. Compounds were checked by XRD periodically during the synthesis in order to verify formation, and were only milled for a maximum of 1hr at a time to avoid overheating. Catalysts were weighed out and added in 2 mol% to the parent material and milled for 30 min to thoroughly mix the compounds.

4.3.1.a Inert Atmosphere Material Handling Considerations

Synthesis of these hydrogen storage materials was primarily done through the mechanochemical synthesis method described above. All handling of the materials was done inside of an inert Argon glove box and with great caution, as exposure to moisture or oxygen can lead to fire. The hydride precursors arrived in sealed ampoules as powders, and were then transferred into the box and weighed in appropriate ratios. The powders were placed inside the stainless steel canister inside the glove box and then transferred out into the mixer mill. In order to characterize these materials, they were transferred back into the glove box after each time interval or experiment, and transferred into the appropriate container such as a Kapton film sealed zero background XRD sample holder.

4.3.2 Material Characterization

Scanning Electron Microscopy (SEM)

Electron microscopy is a very valuable technique and can be used for a variety of things. In this work it was used to show morphology and particle size of the samples. SEM bombards the sample in vacuum with electrons using a raster technique, and then measures the intensity of the induced electron cascade at each point, forming an image. This has an advantage over optical microscopy as much higher resolutions are possible. This higher resolution is possible

because the wavelength of light is much larger than the wavelength of an electron, yielding higher possible resolution in electron microscopy.

X-Ray Diffraction (XRD)

This is the same technique described earlier in section 2.3.2.1, and is also used to verify what crystalline phases are present in the material. Special precautions were needed in order to use this technique on these hydrogen storage materials, as they are pyrophoric. The samples were loaded onto a zero background single crystal silicon sample holder sealed with Kapton foil. This allows the sample to be run without exposure to oxygen or moisture.

4.3.3 Hydrogen Storage Materials Testing

Two distinct methods were used in testing the amount of hydrogen released from the storage materials. The more common method is thermal release of the hydrogen, and this method is used for both adsorption and absorption materials. This method was performed in this work as more of a check to compare with other published catalyst results. The second method is ammonolysis, which is the reaction of these materials with ammonia, which chemically releases the hydrogen. The effect of catalysts with this release method is not as apparent in the literature, and is explored in this work. These methods are described in more detail below.

4.3.3.a Thermal Hydrogen Release

Arguably the most common method of hydrogen release for hydrogen storage materials is thermal hydrogen release. In this method, the storage material is heated to a given temperature, and the hydrogen release is either measured as a weight loss or as a pressure increase. This can be done using thermal gravimetric analysis techniques (TGA), in which the sample is loaded onto a balance, which is lowered into a furnace, and the weight of the sample is continuously

measured over increasing time and temperature. The chamber is purged with helium most commonly, and the entire device can be placed in an Argon glove box. If this is not available, it is possible to seal the sample in a hermetically sealed DSC (differential scanning calorimetry) pan with a small pin hole in it, and then place the pan quickly onto the balance and start the test. The initial small hydrogen release maintains a small positive pressure in the pan preventing further oxygen exposure, allowing transfer into the furnace without ruining the sample. This however is not ideal as there is a small amount of initial exposure to air and the TGA requires you to weigh the pan first, then transfer it into the glove box, seal in the sample, and again place the pan with sample on the balance. This is the method that was available and was used in this work.

4.3.3.b Ammonolysis Hydrogen Release

This method of releasing hydrogen has several distinct advantages and disadvantages. Metal and complex hydrides can be reacted with ammonia gas to release the hydrogen from the storage media. This reaction occurs at room temperature and atmospheric pressure, which are huge advantages for mobile applications over thermal hydrogen release. The disadvantage is the added cost and weight of the ammonia gas itself, as well as the check valves necessary for introduction. Ammonia also poisons fuel cell membranes, so it must be separated from the hydrogen gas, which is easily done with an ammonia trap. A schematic illustrating how this method was used in testing the materials in this work can be seen in the following figure.

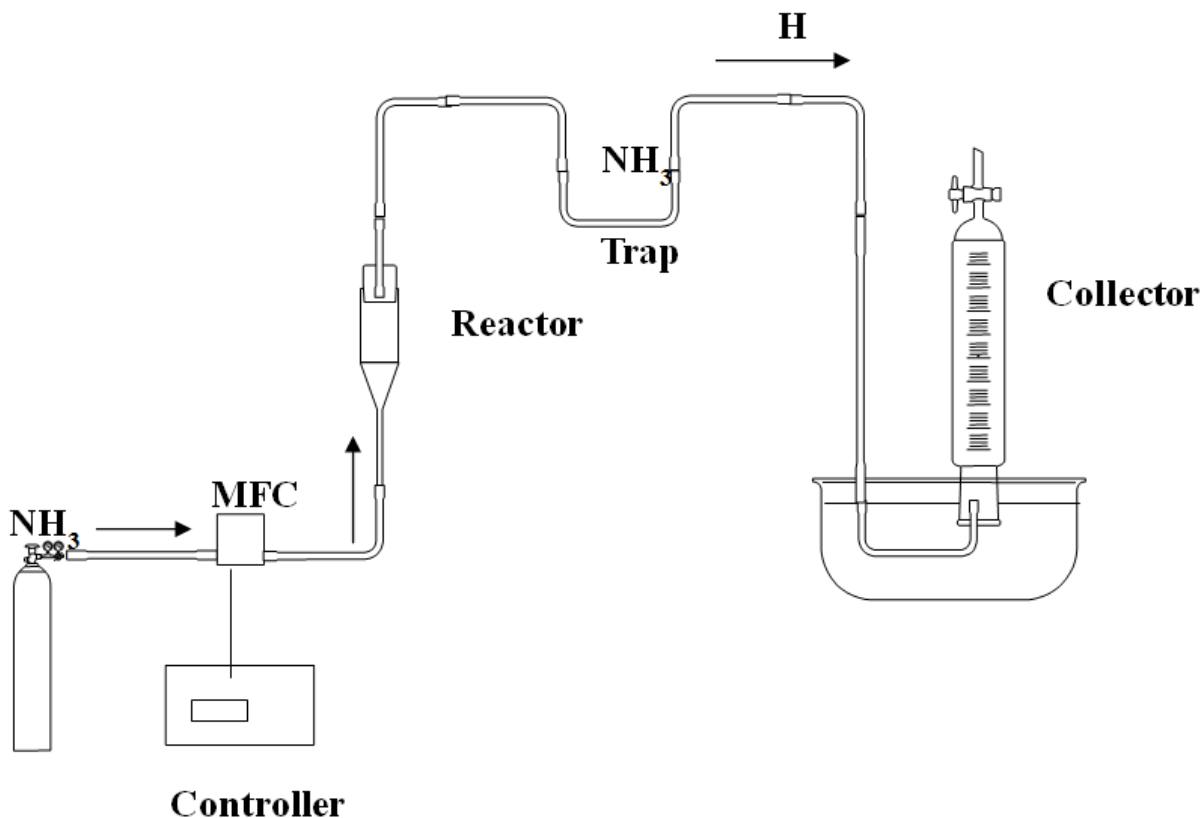


Figure 33: Ammonolysis set up (schematic courtesy of Dr. John Wilkes, Air Force Academy).

By measuring the temperature of the water bath, the atmospheric pressure, and the volume displaced in the collector, the moles of hydrogen can be calculated using the vapor pressure of water at the given bath temperature using the ideal gas law, $PV=nRT$. The vapor pressure from the water column is found from a table based on its temperature, and subtracted from the atmospheric pressure. Volume is the displaced volume of water in the water column, and the temperature is measured with a thermocouple. The number of moles of sample is calculated by knowing the molar percentage of each compound, and their molecular weight, and the measured weight of the sample. The ratio of $n_h/n_{h\text{theoretical}}$ based on chemical formula without the 2% catalyst gives the percent yield. This percent yield is useful in comparing the different catalysts performance verses the parent compound alone, and takes into account the difference in molecular weights of the catalyst materials. This is reported later in section 4.5.2.

The reaction that occurs during chemical hydrogen release is different than that given above in the previous section. An example of this is shown below in Equation 7.

Equation 7



Note that some of the hydrogen released is from the ammonia and not only from the storage material, so direct comparisons between the two dehydrogenation methods would be misleading, but relative amount of hydrogen release with the catalyst is still valid.

4.4 Research Approach

The primary goal of this research was to increase the amount of hydrogen released from a set of metal hydrides to make them more feasible for transportation applications. A set of dopants were added to the parent compounds and ball milled together to see if they act as catalysts in the release of the hydrogen for both thermal and ammonolysis types of hydrogen release. These catalysts were chosen by selecting previously reported catalysts, and then selecting like compounds in the same group. For example, LaCl_3 is reported by Xueping et al as a catalyst for LiAlH_4 for thermal release, so it is reproduced and tested with ammonolysis and TGA for Li_3AlH_6 , and then the rest of the lanthanide series chlorides were attempted. The best performing catalysts were then applied to $\text{LiNa}_2\text{AlH}_6$ as this material takes several weeks to synthesize.

4.5 Results/Discussion

4.5.1 Characterization

After the parent material was synthesized and the phase was identified using X-ray Diffraction (XRD), 2 mol% of the dopant materials were manually mixed with the parent

materials in 0.5g batches and milled for 30 minutes. This material was then characterized using XRD to identify new phases, and to avoid exposure to atmosphere the samples were placed in a holder and covered with a Kapton film consistent with previous work on hydrides¹²⁰. Stacked XRD plots showing the catalyst peaks indicated with an asterisk for Li_3AlH_6 are seen in Figure 34 and Figure 35.

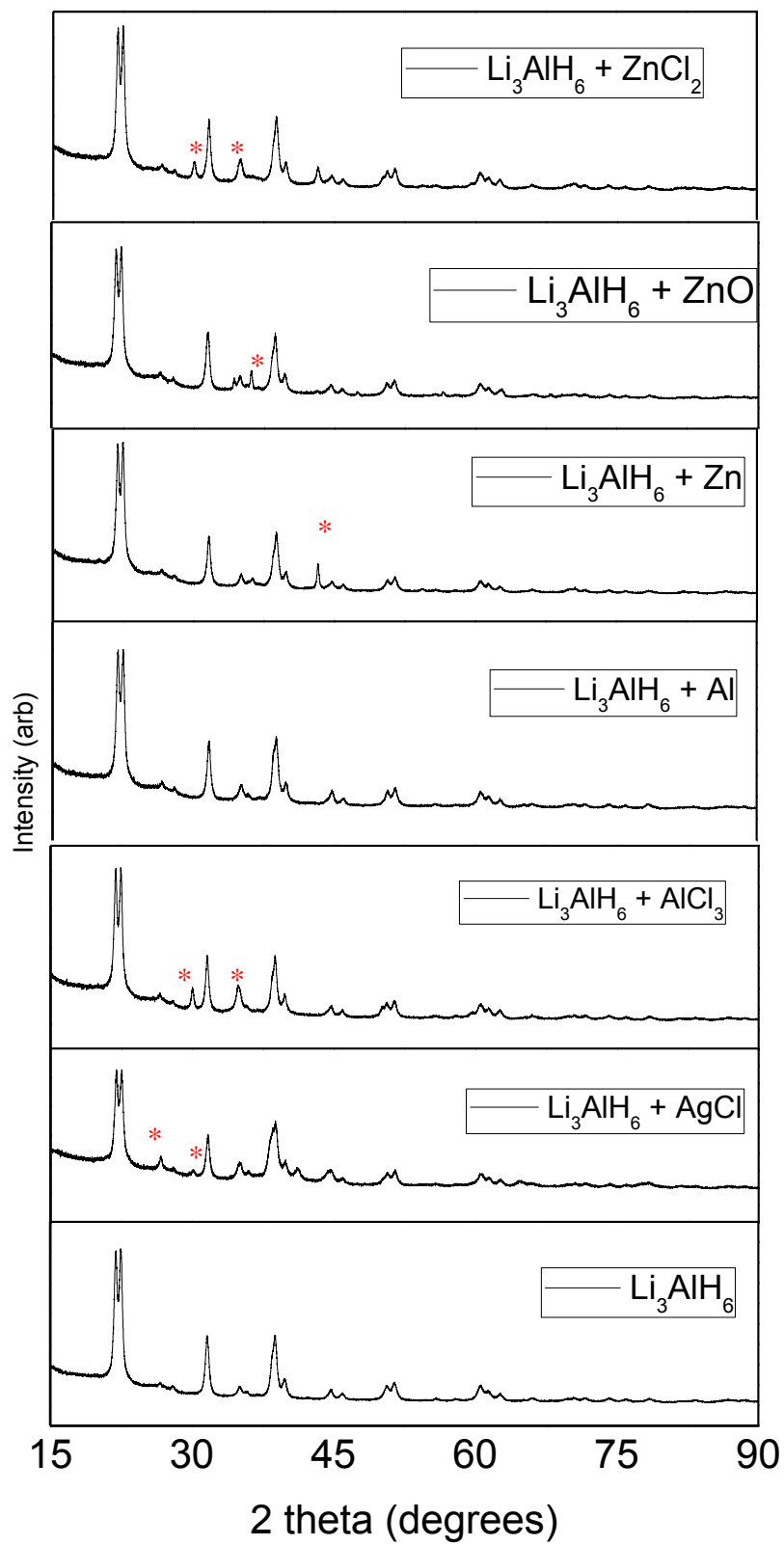


Figure 34: XRD plot of Li_3AlH_6 with Ag, Al, and Zn catalysts

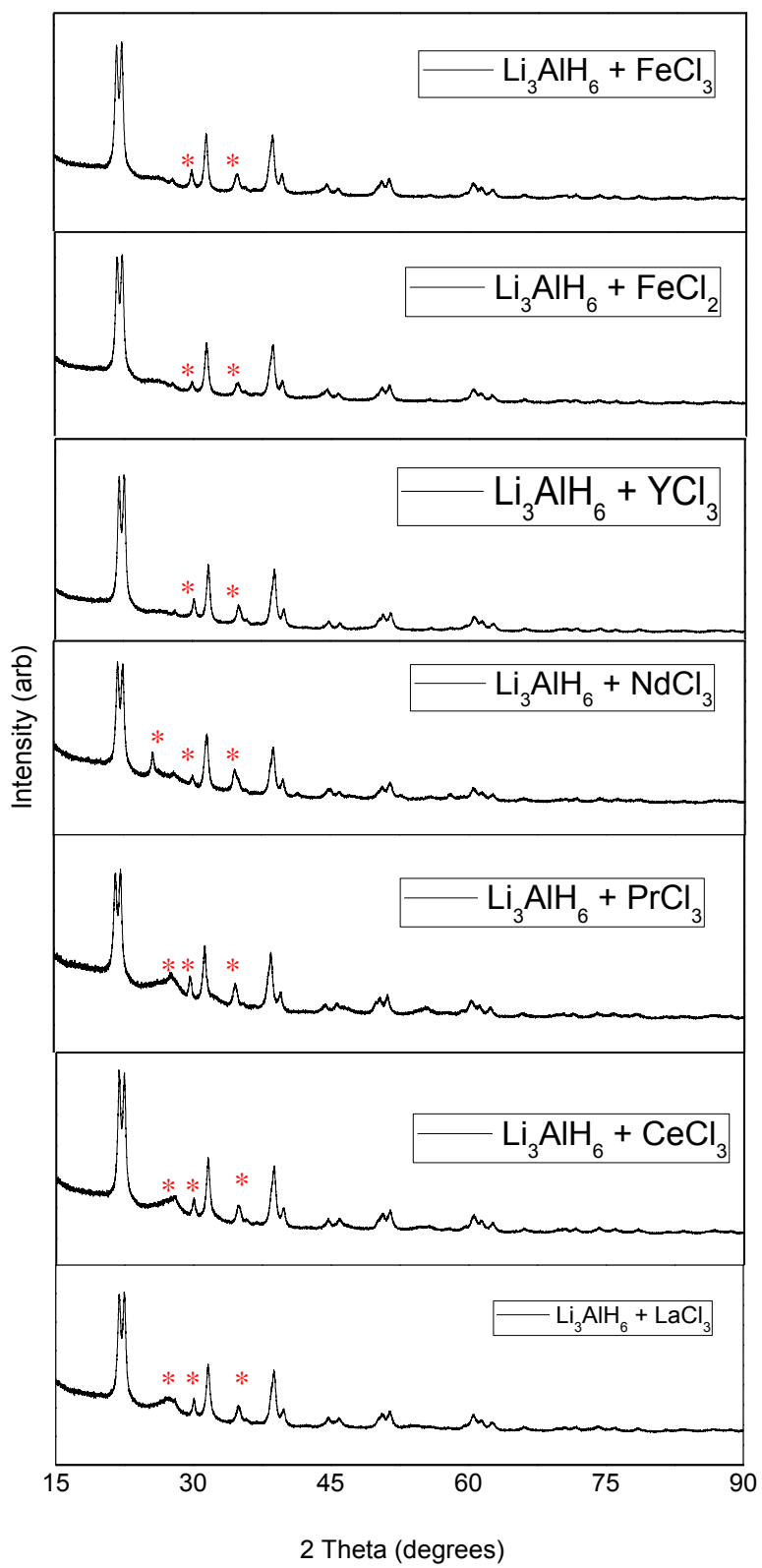


Figure 35: XRD plot of Li_3AlH_6 with La, Ce, Pr, Nd, and Y catalysts

The $\text{LiNa}_2\text{AlH}_6$ compound was synthesized in steps, and characterized at each point. The transformation from Li_3AlH_6 to $\text{LiNa}_2\text{AlH}_6$ can be seen in the appendix (Figure 50). The finished compound and its doped parts are seen in Figure 36.

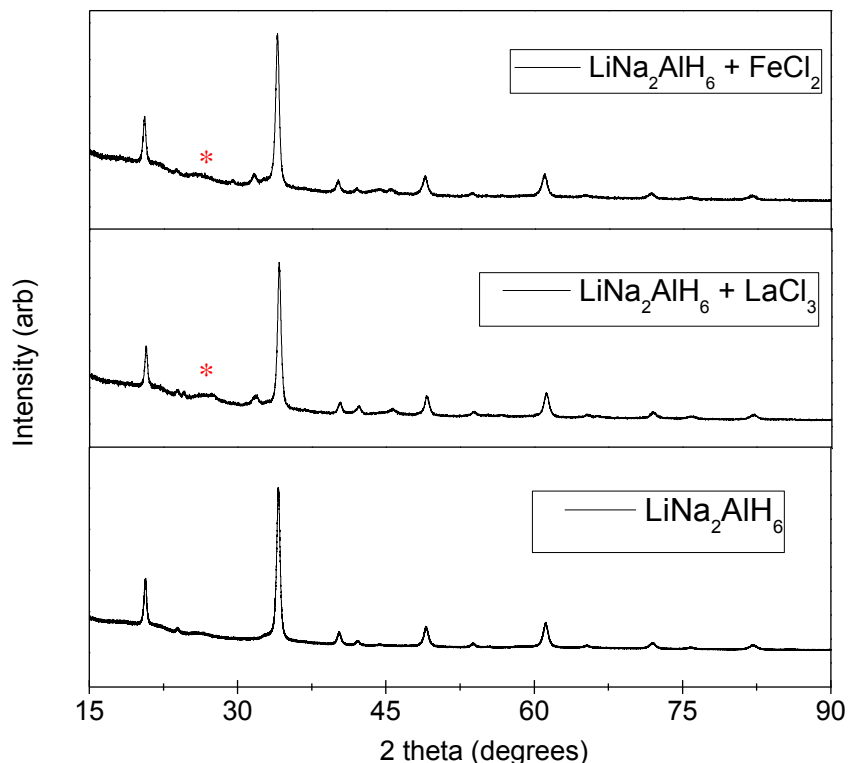


Figure 36: XRD plot of $\text{LiNa}_2\text{AlH}_6$ with catalysts

The materials are also analyzed with a SEM for surface morphology. Special care is taken during the transfer from sealed container into nitrogen purged stage to minimize oxygen exposure. Images of these powders also are difficult to obtain at high magnification as the samples are not good electrical conductors and would charge, blurring the image. No noticeable difference was evident in material with and without catalyst at the low magnifications that were able to be used seen in. They were not coated with a conductive compound as it would change the morphology of the surface that is trying to be observed. A representative image is shown below in Figure 37.

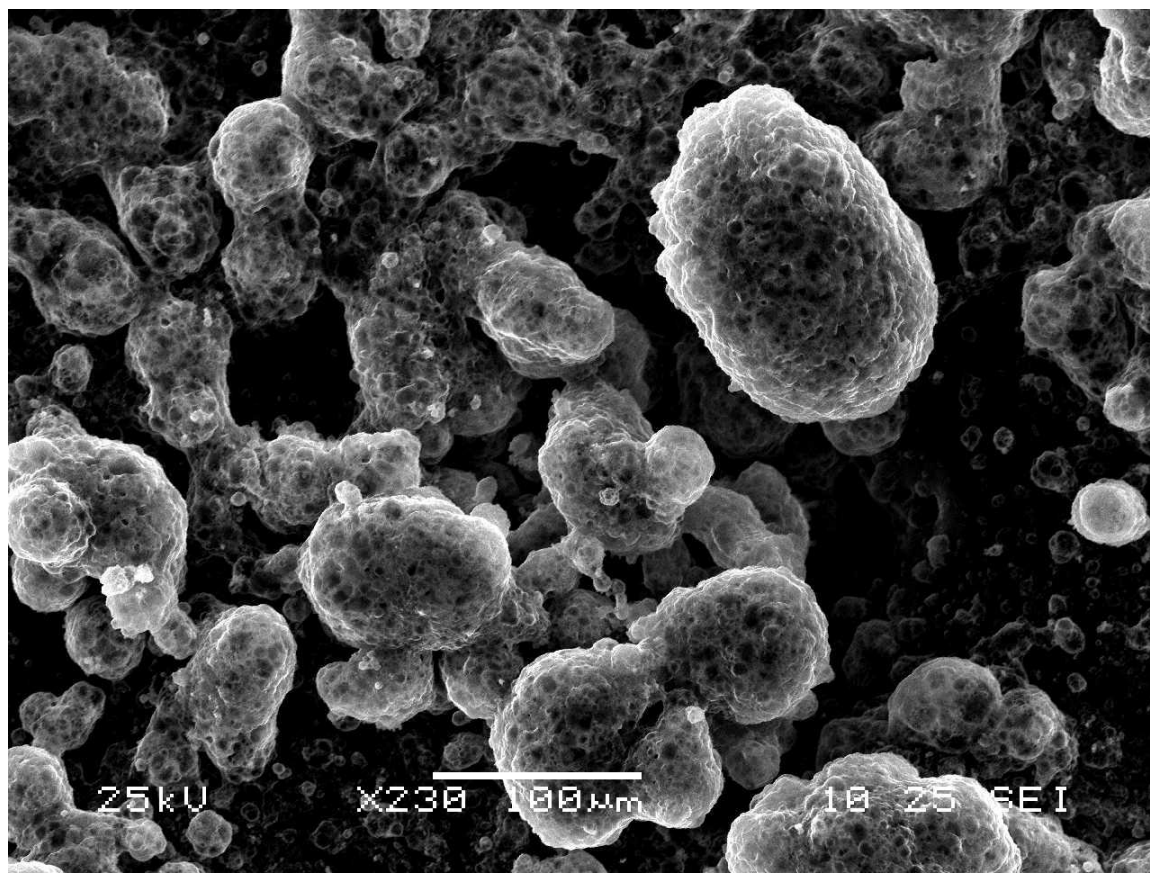


Figure 37: SEM image of LiNa₂AlH₆

4.5.2 Hydrogen Release

The hydrogen release from these compounds was determined by two methods. The first method is the most common, which is thermal release. Thermal gravimetric analysis (TGA) is then used to determine the percentage hydrogen release upon heating and the temperature that it occurs. In order to do this and limit air exposure, the sample is placed in an aluminum DSC (differential scanning calorimetry) pan in the argon glove box and then hermetically sealed. The pan has a 75 micron hole that is laser cut into the top to allow for the release of the hydrogen. In order to stay within the melting limits of the aluminum pan, the sample is then heated under argon in a Thermal Analysis Q500 under argon purge up to 450 °C. The first compounds that were synthesized were the Li₃AlH₆ compounds, and the thermal hydrogen release of those

compounds is summarized in Figure 38. Individual plots of these compounds can be found in appendix 2 for further reference.

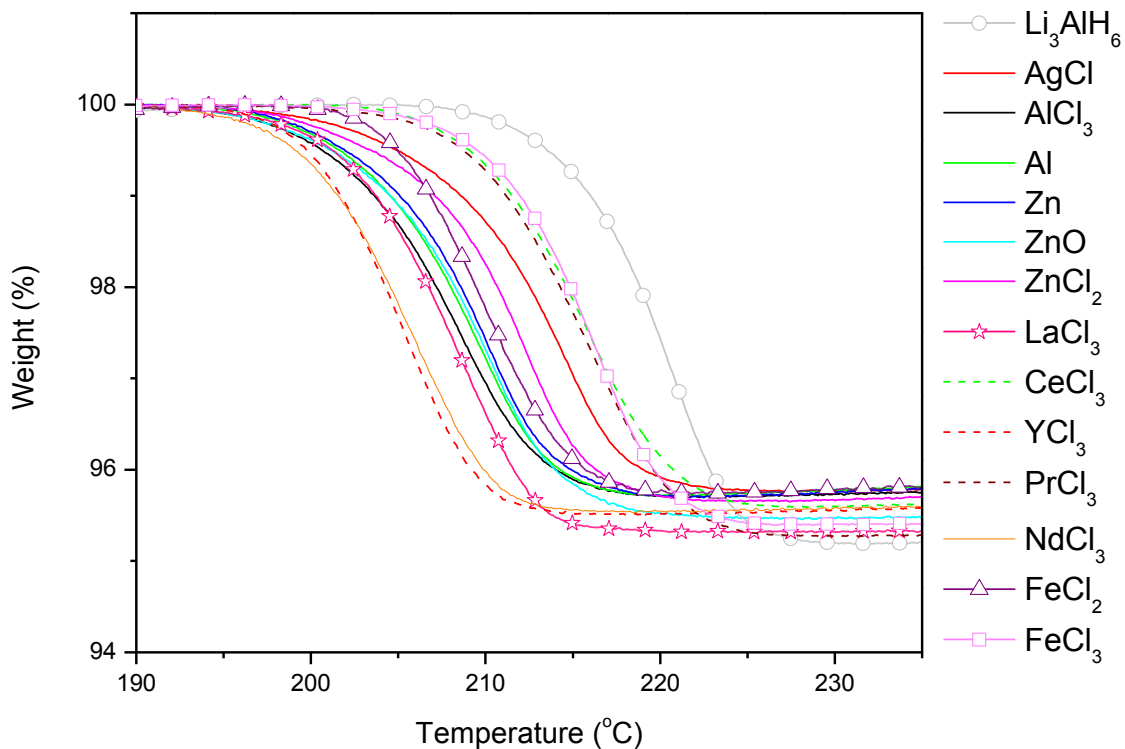


Figure 38: Thermal hydrogen release for Li_3AlH_6 compounds

The dopants have very little to do with the amount of hydrogen that is thermally released, but it does effect the temperature that it is released at and the range varies by 20°C .

These compounds were also tested using ammonolysis. In this experiment 0.1g of sample was placed in a reaction vessel and exposed to ammonia with a mass flow controller at a 15 sccm. The hydrogen gas released is then collected in a water column while excess ammonia is caught in a trap. The volume of hydrogen produced measured and the percent yield is then calculated. These results can be seen in Table 2.

Table 2: Li₃AlH₆ Ammonolysis Results

Sample	nH (mol)	nHydride (mol)	nH theoretical (mol)	nH/nHydride	Yield (%)
Li ₃ AlH ₆	0.00196	0.0019	0.01111	1.06	17.7%
Li ₃ AlH ₆ + Al	0.00187	0.0019	0.01119	0.98	16.7%
Li ₃ AlH ₆ + Zn	0.00064	0.0019	0.01124	0.33	5.7%
Li ₃ AlH ₆ + LaCl ₃	0.00227	0.0017	0.01017	1.31	22.3%
Li ₃ AlH ₆ + CeCl ₃	0.00168	0.0018	0.01059	0.93	15.8%
Li ₃ AlH ₆ + NdCl ₃	0.00075	0.0017	0.01024	0.43	7.3%
Li ₃ AlH ₆ + PrCl ₃	0.00034	0.0017	0.01047	0.20	3.3%
Li ₃ AlH ₆ + YCl ₃	0.00044	0.0018	0.01061	0.25	4.1%
Li ₃ AlH ₆ + AlCl ₃	0.00175	0.0018	0.01091	0.96	16.0%
Li ₃ AlH ₆ + ZnCl ₂	0.00019	0.0018	0.01079	0.10	1.7%
Li ₃ AlH ₆ + FeCl ₂	0.00223	0.0019	0.01133	1.18	19.7%
Li ₃ AlH ₆ + FeCl ₃	0.00044	0.0018	0.01065	0.25	4.1%

The ammonolysis results show that the dopants can play a large role in the amount of hydrogen released when exposed to ammonia. The best performing dopants were applied to the LiNa₂AlH₆ compound, and the thermal hydrogen release and ammonolysis results are shown in Figure 39 and Table 3, respectively.

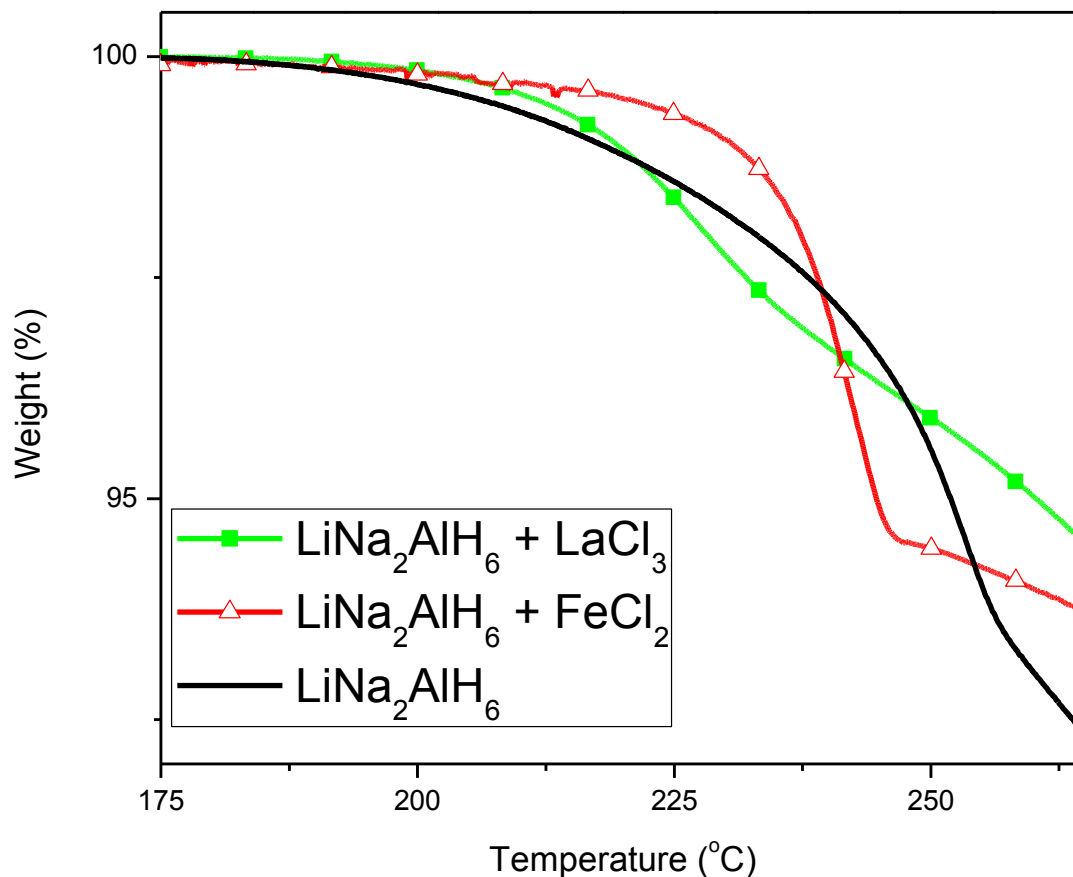


Figure 39: Thermal hydrogen release of LiNa₂AlH₆

Note that the plot only shows the first transition, as the Na compounds are known to decompose past this temperature and can give a false impression of a very large weight loss due to hydrogen loss. Typical dehydrogenation is stopped at 270 °C in the literature^{95,121} and is what is reported here. The increase in hydrogen release is not seen in the thermal release of hydrogen as illustrated above, though the release temperature is decreased.

Table 3: LiNa₂AlH₆ Ammonolysis Results

Sample	nH (mol)	nHydride (mol)	nH theoretical (mol)	nH/nHydride	Yield (%)
LiNa ₂ AlH ₆	0.00348	0.0012	0.00728	2.87	47.8%
LiNa ₂ AlH ₆ + LaCl ₃	0.00475	0.0011	0.00673	4.15	70.7%
LiNa ₂ AlH ₆ + FeCl ₂	0.00324	0.0012	0.00707	2.70	45.9%

The LaCl₃ doped sample shows the highest amount of hydrogen released per mol during ammonolysis of any of the LiNa₂AlH₆ compounds, which is also seen above in the Li₃AlH₆ compounds.

4.6 Hydrogen Storage Testing Summary

The effect of the best catalysts was seen during the ammonolysis hydrogen release process. When the LaCl₃ doped samples were tested under these conditions, a significant increase in the amount of hydrogen per weight was present. SEM images above did not show an obvious difference in surface morphology when these dopants are added, suggesting that there is a different mechanism present for the increased hydrogen release. Marashdeh et al propose a mechanism for the role of Ti as a catalyst in NaAlH₄ where the Ti adsorbs to the surface of the material and then exchanges with the Na, which de-stabilizes material and allows for a lower energy hydrogen release¹¹⁵. This could be the mechanism for a larger amount of hydrogen in this case as well, as the La could potentially exchange with the Na and Li, creating LiCl and NaCl, and de-stabilizing the hydrogen containing compound allowing for more hydrogen release.

Chapter 5: Conclusion/Summary

This work focused on improving two distinct types of energy storage. The first of which is improving the cathode material in lithium ion batteries. A high specific capacity cathode material with low precursor cost was sought out using compositional diagrams of compatible existing cathode materials with individual desired properties. A composite structured cathode material was found with better performance than the individual end members. This material was characterized and found to have a predominantly layered crystal structure, which seems to correspond to the higher capacity regions of the compositional diagram. With the composition and performance map generated from this work, changes in synthesis temperature would be a useful follow up to try to tune the structures in the composite cathode materials. This could result in less disorder and an even higher capacity cathode material. The next steps toward a viable new cathode material would be extended cycling and safety testing.

The second energy storage technology studied was the storage of hydrogen fuel in complex chemical hydrides. The hydrides chosen in this work have a high theoretical hydrogen storage density, but are unable to release all of the stored hydrogen. A series of catalysts were used in this work to try and improve the yield of these chemical hydrides. LaCl_3 doped samples have an improved yield over un-doped samples. A good follow up to this work would be determining the effect of this catalyst on the rehydrogenation of these materials.

References

- (1) Goodenough, J. B.; Abruna, H. D.; Buchanan, M. V. *Basic Research Needs for Electrical Energy Storage. Report of the Basic Energy Sciences Workshop on Electrical Energy Storage, April 2-4, 2007*, 2007.
- (2) Linden, D.; Reddy, T. *Handbook of batteries*; McGraw-Hill New York, 2002.
- (3) Huggins, R. *Advanced Batteries: Materials Science Aspects*; Springer Verlag, 2008.
- (4) Mosby, J. M.; Prieto, A. L. *Journal of the American Chemical Society* **2008**, *130*, 10656.
- (5) Tarascon, J.; Armand, M. *Nature* **2001**, *414*, 359.
- (6) Ikeda, H.; Saito, T.; Tamura, H. *Vol. I, Cleveland* **1975**, 384.
- (7) Van Gool, W.; Division, N. A. T. O. S. A. *Fast Ion Transport in Solids: Solid State Batteries and Devices*; North Holland Pub. Co., 1973.
- (8) Whittingham, M. *Science* **1976**, *192*, 1126.
- (9) Thackeray, M.; Johnson, P.; de Picciotto, L. *Materials Research Bulletin* **1984**, *19*, 179.
- (10) Mizushima, K.; Jones, P. C.; Wiseman, P. J.; Goodenough, J. B. *Materials Research Bulletin* **1980**, *15*, 783.
- (11) Nagaura, T.; Tozawa, K. *Progress in batteries and solar cells* **1990**, *9*, 209.
- (12) Armand, M.; Tarascon, J. **2008**.
- (13) Castro-García, S.; Castro-Couceiro, A.; Señari's-Rodri'guez, M.; Soulette, F.; Julien, C. *Solid State Ionics* **2003**, *156*, 15.
- (14) Wu, S.; Hsiao, K.; Liu, W. *Journal of Power Sources* **2005**, *146*, 550.
- (15) Sauvage, F.; Baudrin, E.; Gengembre, L.; Tarascon, J. *Solid State Ionics* **2005**, *176*, 1869.
- (16) Padhi, A. *Thesis (PhD). The University of Texas at Austin, Source DAI-B 58/07, p. 3870, Jan 1998, 183 pages.* **1998**.
- (17) Balakrishnan, P.; Ramesh, R.; Prem Kumar, T. *Journal of Power Sources* **2006**, *155*, 401.
- (18) Fisher, C.; Hart Prieto, V.; Islam, M. *Chemistry of Materials* **2008**, *20*, 5907.
- (19) Padhi, A.; Nanjundaswamy, K.; Goodenough, J. *Journal of the Electrochemical Society* **1997**, *144*, 1188.
- (20) Delmas, C.; Maccario, M.; Croguennec, L.; Le Cras, F.; Weill, F. *Nature materials* **2008**, *7*, 665.
- (21) Thackeray, M. M. *Progress in Solid State Chemistry* **1997**, *25*, 1.
- (22) Göktepe, H.; Şahan, H.; Patat, Ş.; Ülgen, A. *Ionics* **2009**, *15*, 233.
- (23) Gummow, R.; Kock, A.; Thackeray, M. *Solid State Ionics* **1994**, *69*, 59.
- (24) Takahashi, M.; Yoshida, T.; Ichikawa, A.; Kitoh, K.; Katsukawa, H.; Zhang, Q.; Yoshio, M. *Electrochimica Acta* **2006**, *51*, 5508.
- (25) Jahn, H. A.; Teller, E. *Proceedings of the Royal Society of London. Series A, Mathematical and Physical Sciences* **1937**, *161*, 220.
- (26) Goodenough, J. B. *Annu. Rev. Mater. Sci.* **1998**, *28*, 1.
- (27) Aricò, A.; Bruce, P.; Scrosati, B.; Tarascon, J.; Van Schalkwijk, W. *Nature materials* **2005**, *4*, 366.

- (28) Capsoni, D.; Bini, M.; Chiodelli, G.; Massarotti, V.; Azzoni, C. B.; Mozzati, M. C.; Comin, A. *Physical Chemistry Chemical Physics* **2001**, *3*, 2162.
- (29) Capsoni, D.; Bini, M.; Chiodelli, G.; Mustarelli, P.; Massarotti, V.; Azzoni, C. B.; Mozzati, M. C.; Linati, L. *The Journal of Physical Chemistry B* **2002**, *106*, 7432.
- (30) Capsoni, D.; Bini, M.; Chiodelli, G.; Massarotti, V.; Mustarelli, P.; Linati, L.; Mozzati, M. C.; Azzoni, C. B. *Solid State Communications* **2003**, *126*, 169.
- (31) Chung, K. Y.; Ryu, C.-W.; Kim, K.-B. *Journal of the Electrochemical Society* **2005**, *152*, A791.
- (32) Thirunakaran, R.; Kalaiselvi, N.; Periasamy, P.; Babu, B.; Renganathan, N.; Muniyandi, N.; Raghavan, M. *Ionics* **2001**, *7*, 187.
- (33) Bellitto, C.; Bauer, E.; Righini, G.; Green, M. *J. Phys. Chem. Solids* **2004**, *65*, 29.
- (34) Pistoia, G.; Antonini, A.; Rosati, R.; Bellitto, C.; Ingo, G. *Chem. Mater* **1997**, *9*, 1443.
- (35) Krins, N.; Hatert, F.; Traina, K.; Dusoulier, L.; Molenberg, I.; Fagnard, J.; Vanderbemden, P.; Rulmont, A.; Cloots, R.; Vertruyen, B. *Solid State Ionics* **2006**, *177*, 1033.
- (36) Shao-Horn, Y.; Middaugh, R. *Solid State Ionics* **2001**, *139*, 13.
- (37) Fey, G. T.-K.; Lu, C.-Z.; Kumar, T. P. *Journal of Power Sources* **2003**, *115*, 332.
- (38) Wei, Y. J.; Yan, L. Y.; Wang, C. Z.; Xu, X. G.; Wu, F.; Chen, G. *The Journal of Physical Chemistry B* **2004**, *108*, 18547.
- (39) Ein-Eli, Y.; Wen, W.; Mukerjee, S. *Electrochemical and Solid-State Letters* **2005**, *8*, A141.
- (40) Thirunakaran, R.; Sivashanmugam, A.; Gopukumar, S.; Rajalakshmi, R. *Journal of Power Sources* **2009**, *187*, 565.
- (41) Capsoni, D.; Bini, M.; Chiodelli, G.; Massarotti, V.; Mozzati, M. C.; Azzoni, C. B. *Solid State Communications* **2003**, *125*, 179.
- (42) Robertson, A. D. *Journal of Electrochemical Society* **1997**, *144*.
- (43) Thirunakaran, R.; Sivashanmugam, A.; Gopukumar, S.; Dunnill, C. W.; Gregory, D. H. *Journal of Materials Processing Technology* **2008**, *208*, 520.
- (44) Kalaiselvi, N. *Portugaliae Electrochimica Acta* **2005**, *23*.
- (45) Tarascon, J. M. *Journal of Electrochemical Society* **1991**, *138*.
- (46) Guo, S.; Zhang, S.; He, X.; Pu, W.; Jiang, C.; Wan, C. *Journal of the Electrochemical Society* **2008**, *155*, A760.
- (47) Yoon, C. S.; Kim, C. K.; Sun, Y. K. *Journal of Power Sources* **2002**, *109*, 234.
- (48) Colbow, K. M.; Dahn, J. R.; Haering, R. R. *Journal of Power Sources* **1989**, *26*, 397.
- (49) Palacín, M. R.; Le Cras, F.; Seguin, L.; Anne, M.; Chabre, Y.; Tarascon, J. M.; Amatucci, G.; Vaughan, G.; Strobel, P. *Journal of Solid State Chemistry* **1999**, *144*, 361.
- (50) He, X.; Li, J.; Cai, Y.; Wang, Y.; Ying, J.; Jiang, C.; Wan, C. *Solid State Ionics* **2005**, *176*, 2571.
- (51) Yi, T.; Hu, X.; Wang, D.; Huo, H. *Journal of University of Science and Technology Beijing, Mineral, Metallurgy, Material* **2008**, *15*, 182.
- (52) Bao, S.-J.; Liang, Y.-Y.; Zhou, W.-J.; He, B.-L.; Li, H.-L. *Journal of Colloid and Interface Science* **2005**, *291*, 433.
- (53) Chen, M.; Li, S.; Yang, C. *Journal of University of Science and Technology Beijing, Mineral, Metallurgy, Material* **2008**, *15*, 468.
- (54) Luo, Q.; Manthiram, A. *Journal of the Electrochemical Society* **2009**, *156*, A84.

- (55) Park, S. H.; Park, K. S.; Sun, Y. K.; Nahm, K. S. *Journal of The Electrochemical Society* **2000**, *147*, 2116.
- (56) Hwang, B. J.; Santhanam, R.; Huang, C. P.; Tsai, Y. W.; Lee, J. F. *Journal of the Electrochemical Society* **2002**, *149*, A694.
- (57) Yuan, Y. F.; Wu, H. M.; Guo, S. Y.; Wu, J. B.; Yang, J. L.; Wang, X. L.; Tu, J. P. *Applied Surface Science* **2008**, *255*, 2225.
- (58) Chung, K. Y.; Yoon, W.-S.; Lee, H. S.; Yang, X.-Q.; McBreen, J.; Deng, B. H.; Wang, X. Q.; Yoshio, M.; Wang, R.; Gui, J.; Okada, M. *Journal of Power Sources* **2005**, *146*, 226.
- (59) Deng, B.; Nakamura, H.; Zhang, Q.; Yoshio, M.; Xia, Y. *Electrochimica Acta* **2004**, *49*, 1823.
- (60) Ohzuku, T.; Ueda, A.; Nagayama, M.; Iwakoshi, Y.; Komori, H. *Electrochimica Acta* **1993**, *38*, 1159.
- (61) Goodenough, J. B.; Kim, Y. *Chemistry of Materials* **2009**, *22*, 587.
- (62) Martha, S.; Markevich, E.; Burgel, V.; Salitra, G.; Zinigrad, E.; Markovsky, B.; Sclar, H.; Pramovich, Z.; Heik, O.; Aurbach, D. *Journal of Power Sources* **2009**, *189*, 288.
- (63) Ammundsen, B.; Paulsen, J.; Davidson, I.; Liu, R.-S.; Shen, C.-H.; Chen, J.-M.; Jang, L.-Y.; Lee, J.-F. *Journal of the Electrochemical Society* **2002**, *149*, A431.
- (64) Storey, C.; Kargina, I.; Grincourt, Y.; Davidson, I. J.; Yoo, Y. C.; Seung, D. Y. *Journal of Power Sources* **2001**, *97-98*, 541.
- (65) Lu, Z.; Chen, Z.; Dahn, J. R. *Chemistry of Materials* **2003**, *15*, 3214.
- (66) Lu, Z.; Dahn, J. *Journal of the Electrochemical Society* **2002**, *149*, A1454.
- (67) Lu, Z.; MacNeil, D. D.; Dahn, J. R. *Electrochemical and Solid-State Letters* **2001**, *4*, A200.
- (68) Liu, Z.; Yu, A.; Lee, J. Y. *Journal of Power Sources* **1999**, *81-82*, 416.
- (69) Yoshio, M.; Noguchi, H.; Itoh, J.-i.; Okada, M.; Mouri, T. *Journal of Power Sources* **2000**, *90*, 176.
- (70) Paulsen, J. M.; Larcher, D.; Dahn, J. R. *Journal of the Electrochemical Society* **2000**, *147*, 2862.
- (71) Park, S. H.; Kang, S. H.; Johnson, C. S.; Amine, K.; Thackeray, M. M. *Electrochemistry Communications* **2007**, *9*, 262.
- (72) Johnson, C.; Li, N.; Vaughey, J.; Hackney, S.; Thackeray, M. *Electrochemistry Communications* **2005**, *7*, 528.
- (73) Paulsen, J. M.; Dahn, J. R. *Chemistry of Materials* **1999**, *11*, 3065.
- (74) Armstrong, A. R.; Bruce, P. G. *Nature* **1996**, *381*, 499.
- (75) Predoană, L.; Barău, A.; Zaharescu, M.; Vassilchina, H.; Velinova, N.; Banov, B.; Momchilov, A. *Journal of the European Ceramic Society* **2007**, *27*, 1137.
- (76) Sun, Y.-K. *Journal of Power Sources* **1999**, *83*, 223.
- (77) Shaju, K. M.; Subba Rao, G. V.; Chowdari, B. V. R. *Electrochimica Acta* **2002**, *48*, 145.
- (78) Shaju, K. M.; Subba Rao, G. V.; Chowdari, B. V. R. *Electrochimica Acta* **2003**, *48*, 1505.
- (79) Dollé, M. *Chemistry of Materials* **2005**, *17*, 1036.
- (80) Cabana, J. *Journal of the Electrochemical Society* **2009**, *156*, A730.
- (81) Toby, B. H. *Powder diffraction* **2006**, *21*, 67.
- (82) Hollander, J. M.; Jolly, W. L. *Accounts of Chemical Research* **1970**, *3*, 193.

- (83) He, X.; Li, J.; Cai, Y.; Jiang, C.; Wan, C. *Materials Chemistry and Physics* **2006**, 95, 105.
- (84) Marks, T. *Journal of the Electrochemical Society* **2011**, 158, A51.
- (85) Barker, J., Colorado State University, 2009.
- (86) Faulkner, L. *Electrochemical Methods Fundamental and Applications*; Wiley India Pvt. Ltd., 2006.
- (87) Dahn, H. M. *Journal of the Electrochemical Society* **2012**, 159, A1405.
- (88) Smith, A.; Burns, J.; Dahn, J. *Electrochemical and Solid-State Letters* **2011**, 14, A39.
- (89) Meza, E.; Ortiz, J.; Ruíz-León, D.; Marco, J.; Gautier, J. *Materials Letters* **2012**, 70, 189.
- (90) Rougier, A.; Saadoune, I.; Gravereau, P.; Willmann, P.; Delmas, C. *Solid State Ionics* **1996**, 90, 83.
- (91) Schlapbach, L.; Züttel, A. *Nature* **2001**, 414, 353.
- (92) Sandrock, G. *Journal of Alloys and Compounds* **1999**, 293–295, 877.
- (93) Gross, K.; Carrington, K.; Barcelo, S.; Karkamkar, A.; Purewal, J.; Parilla, P.; December: 2008.
- (94) *National Hydrogen Energy Roadmap*, United States Department of Energy, 2002.
- (95) Jensen, C. M.; Gross, K. J. *Appl Phys A* **2001**, 72, 213.
- (96) Burke, A.; Gardiner, M. 2005.
- (97) N. L. Rosi; J. Eckert; M. Eddaoudi; D. T. Vodak; J. Kim; M. O' Keefe; Yaghi, O. *M. Science* **2003**, 300, 1127.
- (98) Dillon, A.; Heben, M. *Applied Physics A: Materials Science & Processing* **2001**, 72, 133.
- (99) Norberg, N. S.; Arthur, T. S.; Fredrick, S. J.; Prieto, A. L. *Journal of the American Chemical Society* **2011**, 133, 10679.
- (100) Lovvik, O.; Swang, O.; Opalka, S. *J. Mater. Res* **2005**, 20, 3200.
- (101) Dilts, J. A.; Ashby, E. C. *Inorganic Chemistry* **1972**, 11, 1230.
- (102) Andreasen, A.; Vegge, T.; Pedersen, A. S. *Journal of Solid State Chemistry* **2005**, 178, 3672.
- (103) Sakintuna, B.; Lamari-Darkrim, F.; Hirscher, M. *International Journal of Hydrogen Energy* **2007**, 32, 1121.
- (104) Zaluski, L.; Zaluska, A.; Ström-Olsen, J. O. *Journal of Alloys and Compounds* **1999**, 290, 71.
- (105) Xueping, Z.; Ping, L.; Xuanhui, Q. *Rare Metal Materials and Engineering* **2009**, 38, 766.
- (106) Chen, J.; Kuriyama, N.; Xu, Q.; Takeshita, H. T.; Sakai, T. *The Journal of Physical Chemistry B* **2001**, 105, 11214.
- (107) Resan, M.; Hampton, M. D.; Lomness, J. K.; Slattery, D. K. *International Journal of Hydrogen Energy* **2005**, 30, 1417.
- (108) Wang, J.; Ebner, A. D.; Ritter, J. A. *Journal of the American Chemical Society* **2006**, 128, 5949.
- (109) Xueping, Z.; Shenglin, L. *Rare Metal Materials and Engineering* **2009**, 38, 1328.
- (110) Shim, J.-H.; Lee, G.-J.; Cho, Y. W. *Journal of Alloys and Compounds* **2006**, 419, 176.
- (111) Lee, G.-J.; Shim, J.-H.; Cho, Y. *Journal of Materials Science* **2007**, 42, 6302.

- (112) Shim, J.-H.; Lee, G.-J.; Lee, B.-J.; Oh, Y.-J.; Cho, Y. W. *Catalysis Today* **2007**, *120*, 292.
- (113) Jang, J.-W.; Shim, J.-H.; Cho, Y. W.; Lee, B.-J. *Journal of Alloys and Compounds* **2006**, *420*, 286.
- (114) Kang, X. D.; Wang, P.; Song, X. P.; Yao, X. D.; Lu, G. Q.; Cheng, H. M. *Journal of Alloys and Compounds* **2006**, *424*, 365.
- (115) Marashdeh, A.; Olsen, R. A.; Løvvik, O. M.; Kroes, G.-J. *The Journal of Physical Chemistry C* **2008**, *112*, 15759.
- (116) Gupta, B. K.; Srivastava, O. N. *International Journal of Hydrogen Energy* **2007**, *32*, 1080.
- (117) Zidan, R. A.; Takara, S.; Hee, A. G.; Jensen, C. M. *Journal of Alloys and Compounds* **1999**, *285*, 119.
- (118) Kang, X.-D.; Wang, P.; Cheng, H.-M. *Scripta Materialia* **2007**, *56*, 361.
- (119) Huot, J.; Boily, S.; Güther, V.; Schulz, R. *Journal of Alloys and Compounds* **1999**, *283*, 304.
- (120) Ares, J. R.; Aguey-Zinsou, K. F.; Porcu, M.; Sykes, J. M.; Dornheim, M.; Klassen, T.; Bormann, R. *Materials Research Bulletin* **2008**, *43*, 1263.
- (121) Bogdanović, B.; Schwickardi, M. *Journal of Alloys and Compounds* **1997**, *253–254*, 1.

Appendix 1: Lithium-ion battery reference figures

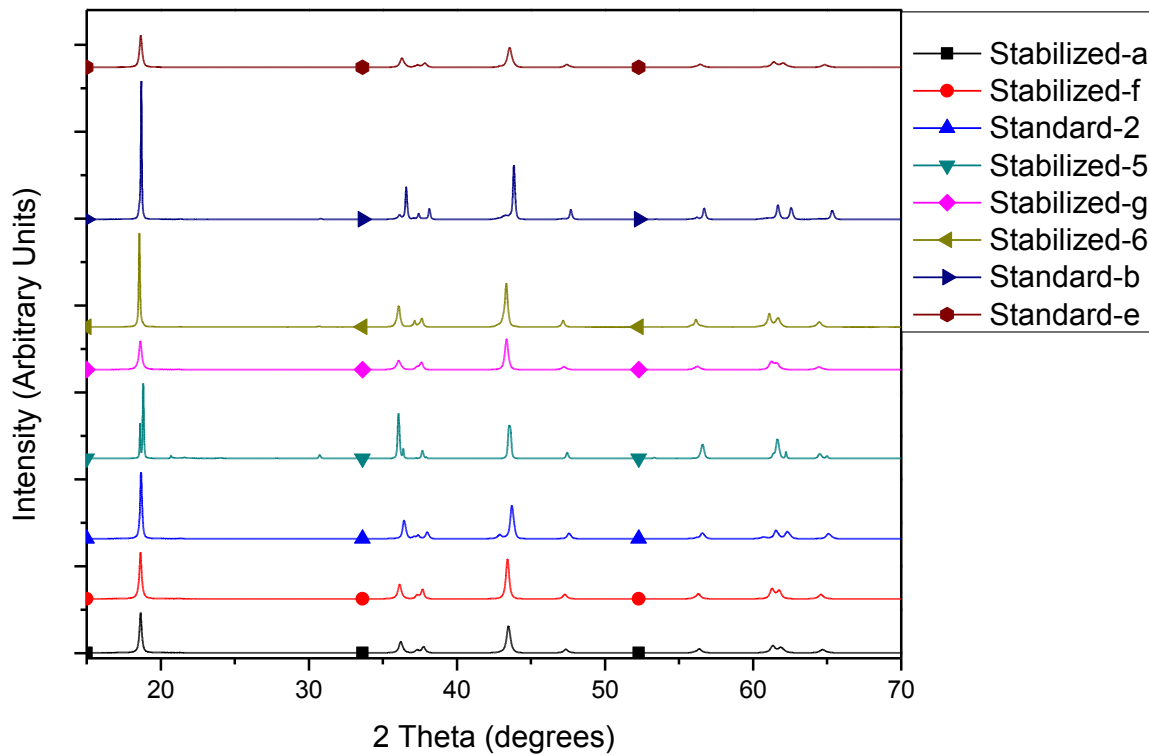


Figure 40: Synchrotron XRD Patterns of Samples Sent to ANLAPS, Converted to CuK α Wavelength

Table 4: Cell Specific Capacities

Composition	Specific Capacity (mAh/g)
Standard 1	149.38
Standard 2	162.17
Standard 3	67.98
Standard 4	149.57
Standard 5	60.43
Standard 6	148.69
Standard 7	85.47
Standard 8	116.5
Standard b	179.14
Standard c	136.26
Standard e	175.56
Standard d	148.35
Standard h	105.10
Stabilized 1	149.59
Stabilized 2	161.14

Stabilized 3	54.1
Stabilized 4	146.91
Stabilized 5	50.89
Stabilized 6	162.81
Stabilized 7	99.59
Stabilized 8	69.76
Stabilized a	173.64
Stabilized b	166.44
Stabilized c	117.09
Stabilized d	106.23
Stabilized e	138.51
Stabilized f	181.58
Stabilized g	174.18
Stabilized h	91.08

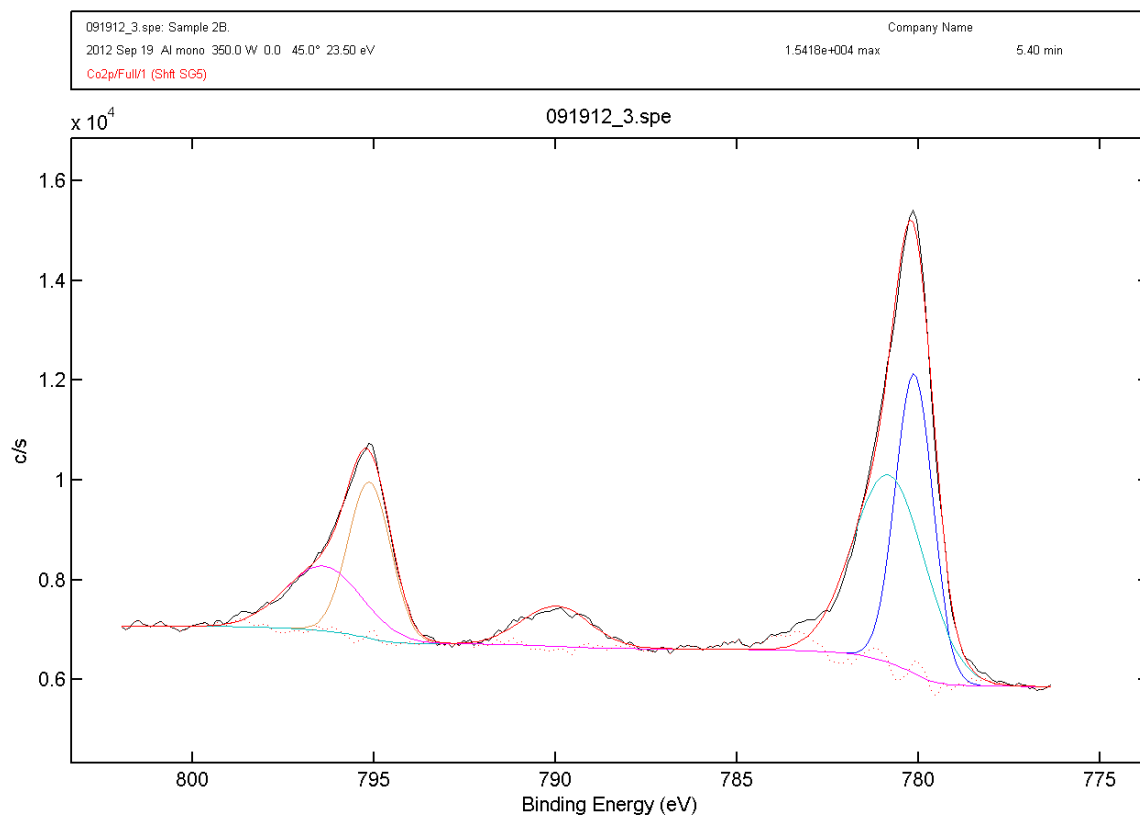


Figure 41: Cobalt Fit for Standard Composition b

091912_5.spe: Sample 3F.
2012 Sep 19 Al mono 350.0 W 0.0 45.0° 23.50 eV
Co2p/Full1 (Shift SGS)
Company Name
1.0015e+004 max
5.40 min

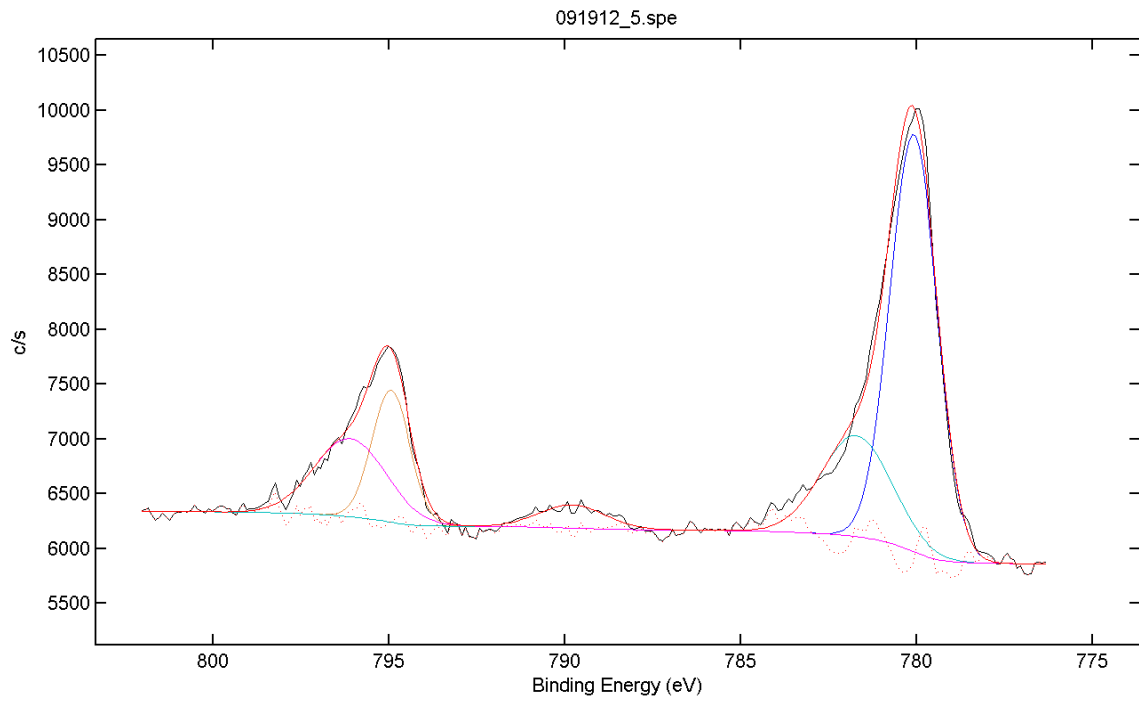


Figure 42: Cobalt Fit for Stabilized Composition f

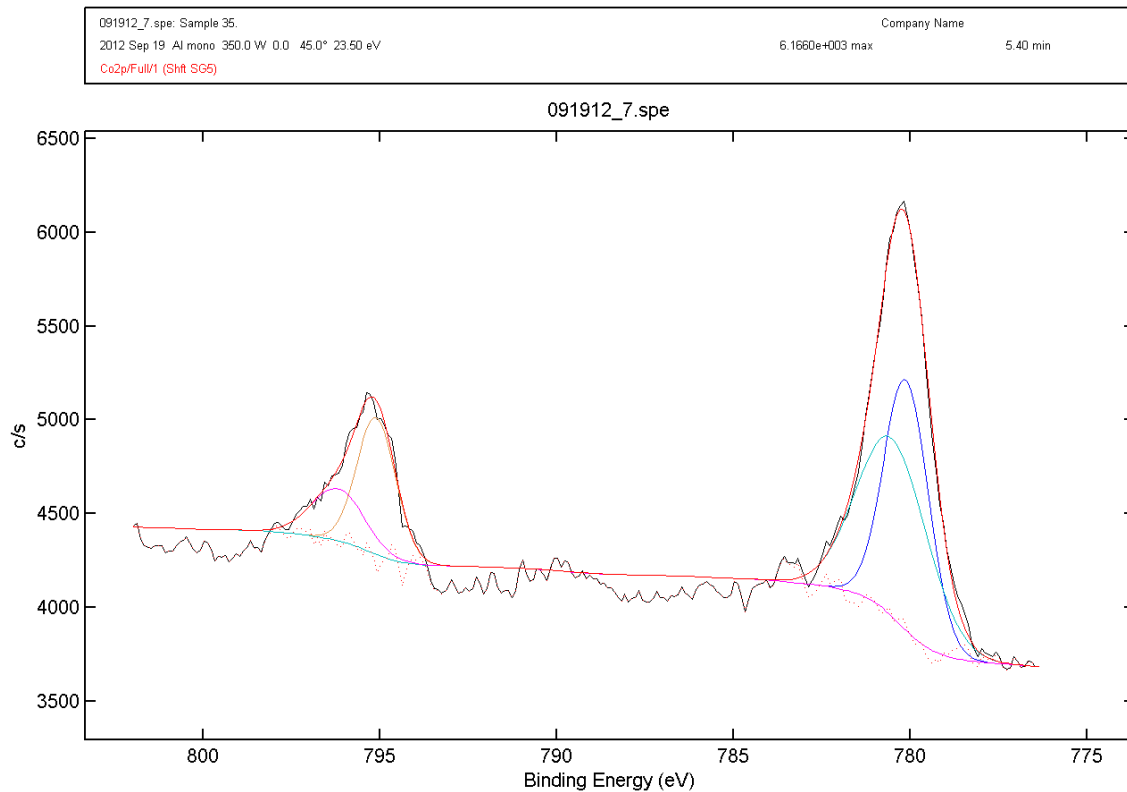


Figure 43: Cobalt Fit for Stabilized Composition 5

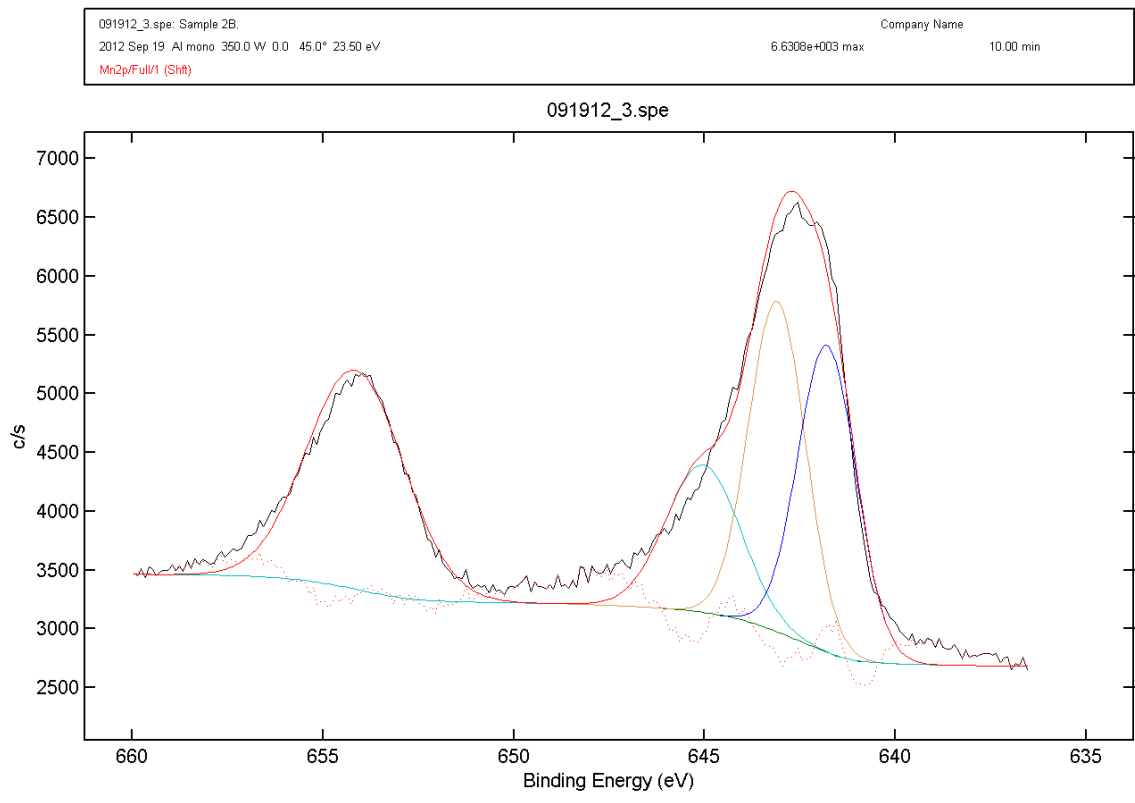


Figure 44: Manganese Fit for Standard Composition b

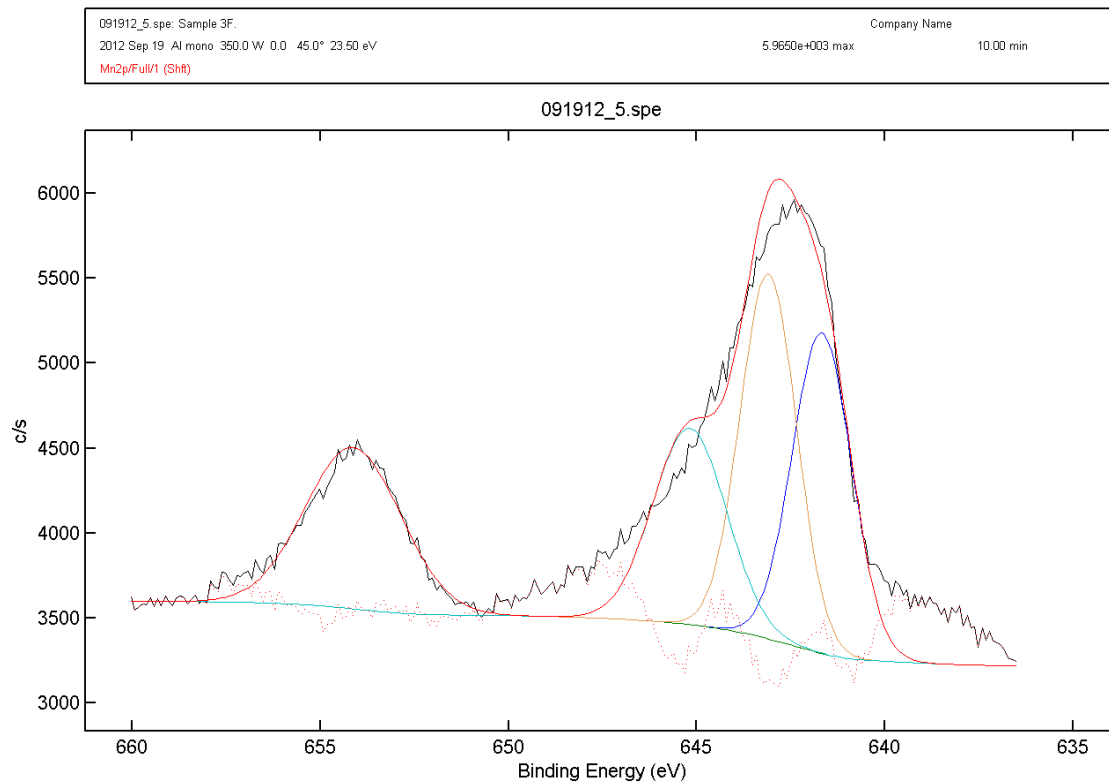


Figure 45: Manganese Fit for Stabilized Composition f

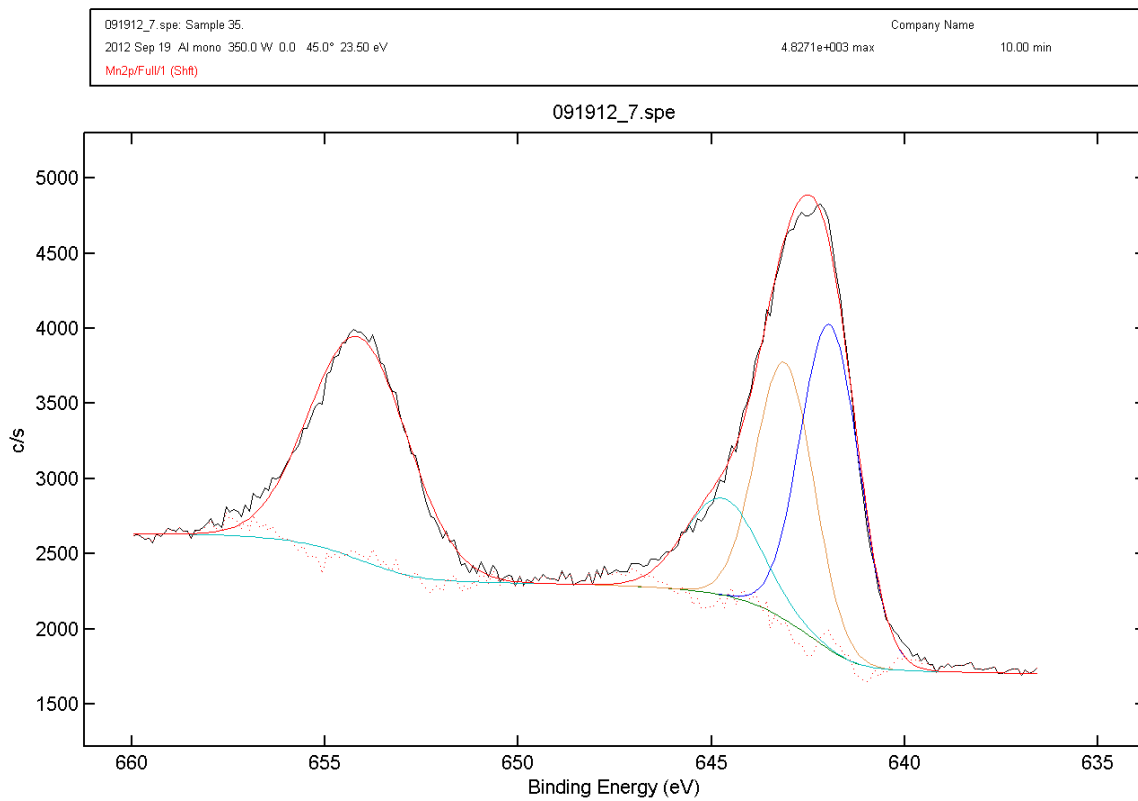


Figure 46: Manganese Fit for Stabilized Composition 5

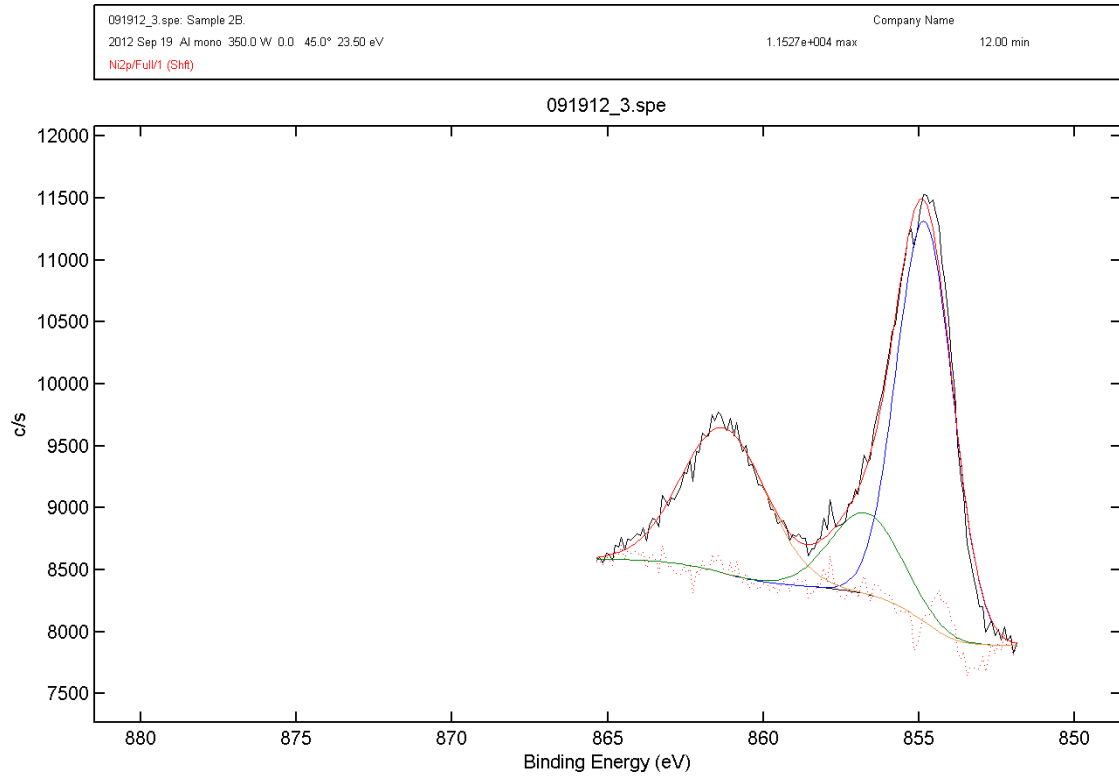


Figure 47: Nickel Fit for Standard Composition b

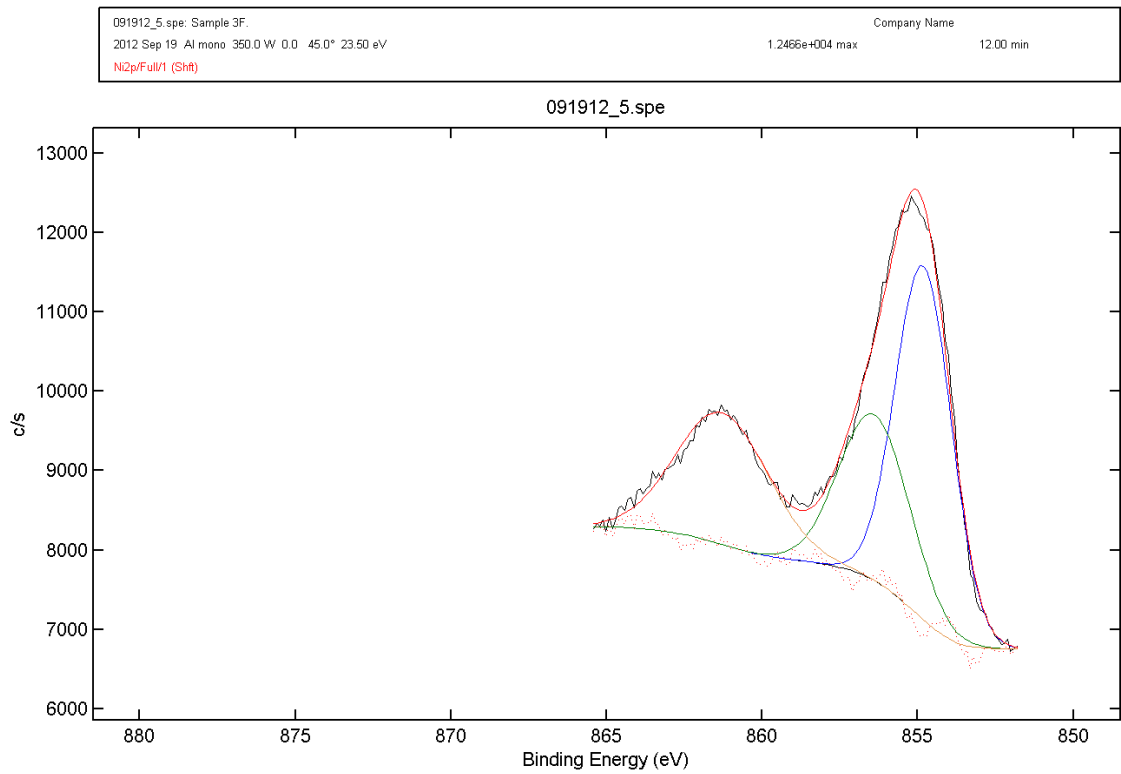


Figure 48: Nickel Fit for Stabilized Composition f

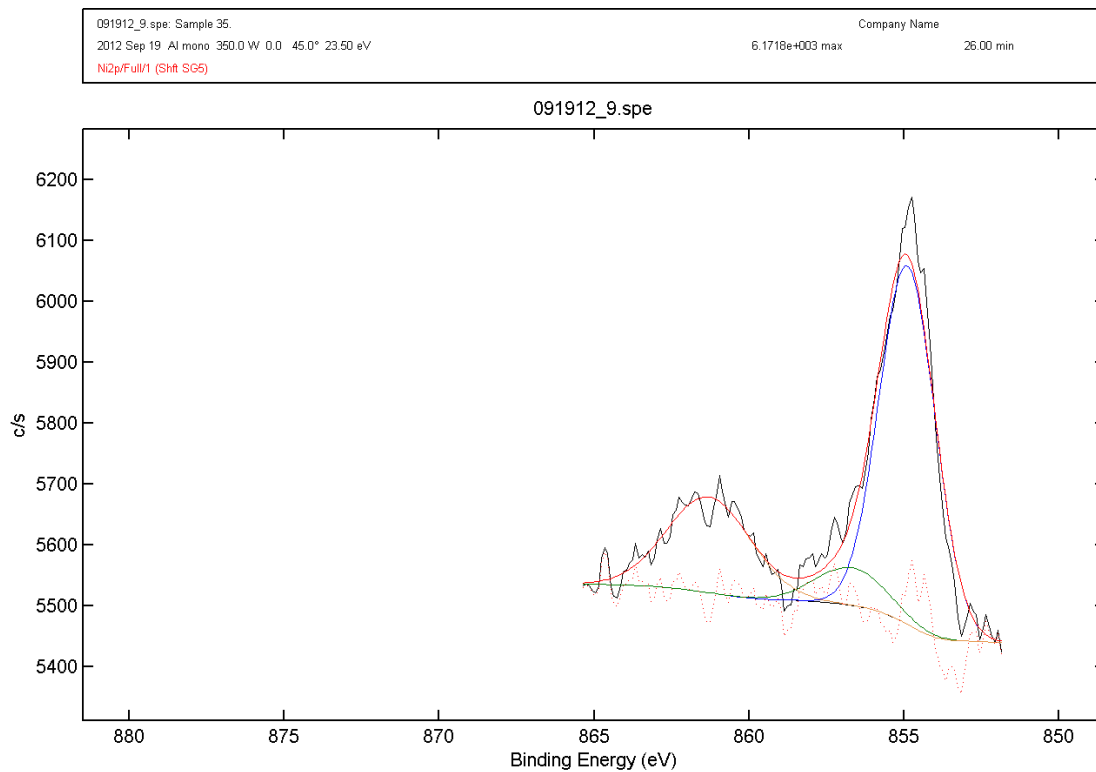
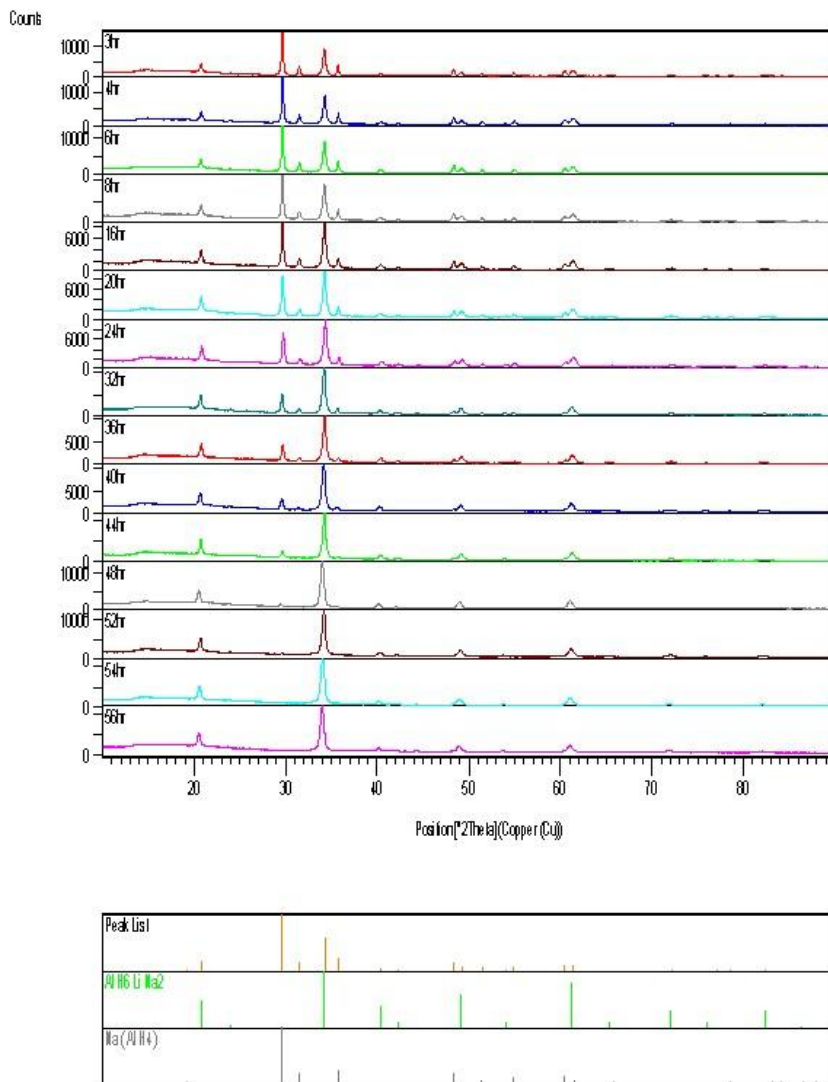


Figure 49: Nickel Fit for Stabilized Composition 5

The above XPS deconvolutions have peaks inserted that represent the different oxidation states of each element. With a variety of binding environments and oxidation states available for each compound, only very slight shifts in binding energies were seen.

Appendix 2: Hydrogen storage reference figures

Date: 8/2/2010 Time: 1:53:26 PM File: 3hr User: PANalytical XRAY



Page: 1 of 1

Figure 50: Sequential formation of $\text{LiNa}_2\text{AlH}_6$

Table 5: Ammonolysis results

Sample	Volume measured (ml)	Dead Volume (ml)	Volume H ₂ (ml)	Water temp (°C)	Water Vapor pressure H ₂ O (mmHg)	Atm pressure (mmHg)	Mass Hydride (g)	Mw sample (g/mol)	nH (mol)	nHydride (mol)	nH theoretical (mol)	nH/nHydride	Yield (%)
Li ₃ AlH ₆	105	42	63	19.5	17.00	586	0.100	53.85	0.00196	0.0019	0.01111	1.06	17.68
Li ₃ AlH ₆ + Al	98	39	59	16.5	14.08	587	0.102	53.31	0.00187	0.0019	0.01119	0.98	16.72
Li ₃ AlH ₆ + Zn	59	39	20	15.9	13.54	587	0.103	54.08	0.00064	0.0019	0.01124	0.33	5.66
Li ₃ AlH ₆ + LaCl ₃	114	42	72	17.8	15.20	587	0.100	57.68	0.00227	0.0017	0.01017	1.31	22.30
Li ₃ AlH ₆ + CeCl ₃	95	42	53	17.6	15.30	589	0.104	57.70	0.00168	0.0018	0.01059	0.93	15.84
Li ₃ AlH ₆ + NdCl ₃	66	42	24	19.1	16.58	587	0.101	57.79	0.00075	0.0017	0.01024	0.43	7.34
Li ₃ AlH ₆ + PrCl ₃	53	42	11	19.5	17.00	587	0.101	57.72	0.00034	0.0017	0.01047	0.20	3.28
Li ₃ AlH ₆ + YCl ₃	56	42	14	19.6	17.11	587	0.100	56.68	0.00044	0.0018	0.01061	0.25	4.12
Li ₃ AlH ₆ + AlCl ₃	98	42	56	19.3	16.79	586	0.101	55.44	0.00175	0.0018	0.01091	0.96	16.02
Li ₃ AlH ₆ + ZnCl ₂	48	42	6	19.6	17.11	586	0.100	55.50	0.00019	0.0018	0.01079	0.10	1.73
Li ₃ AlH ₆ + FeCl ₂	113	42	71	19.5	17.00	591	0.104	55.31	0.00223	0.0019	0.01133	1.18	19.72
Li ₃ AlH ₆ + FeCl ₃	56	42	14	19.6	17.11	591	0.099	56.02	0.00044	0.0018	0.01065	0.25	4.13
LiNa ₂ AlH ₆	152	42	110	18.5	15.97	591	0.104	85.95	0.00348	0.0012	0.00728	2.87	47.76
LiNa ₂ AlH ₆ + LaCl ₃	192	42	150	17	14.53	588	0.102	89.14	0.00475	0.0011	0.00673	4.15	70.65
LiNa ₂ AlH ₆ + FeCl ₂	145	42	103	18.6	16.07	589	0.104	86.77	0.00324	0.0012	0.00707	2.70	45.89

Li₃AlH₆ +2 mol% Al 0600210

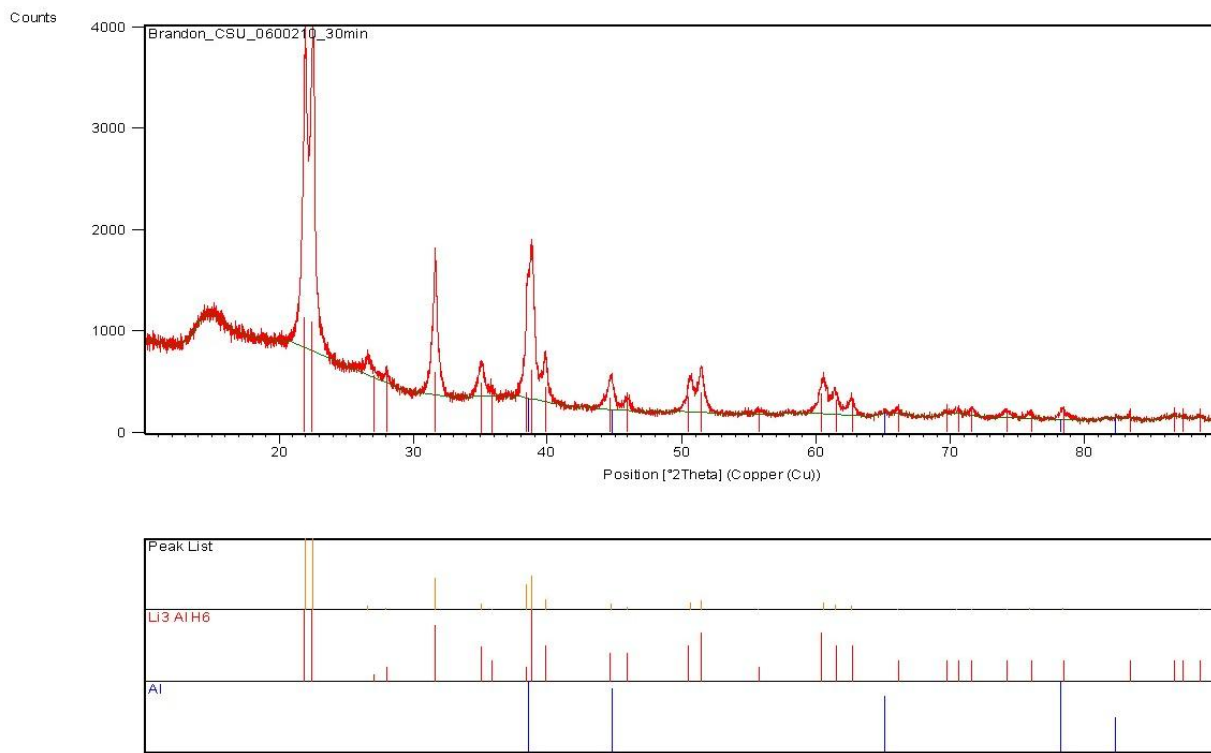


Figure 51: XRD pattern of Li₃AlH₆ +2 mol% Al

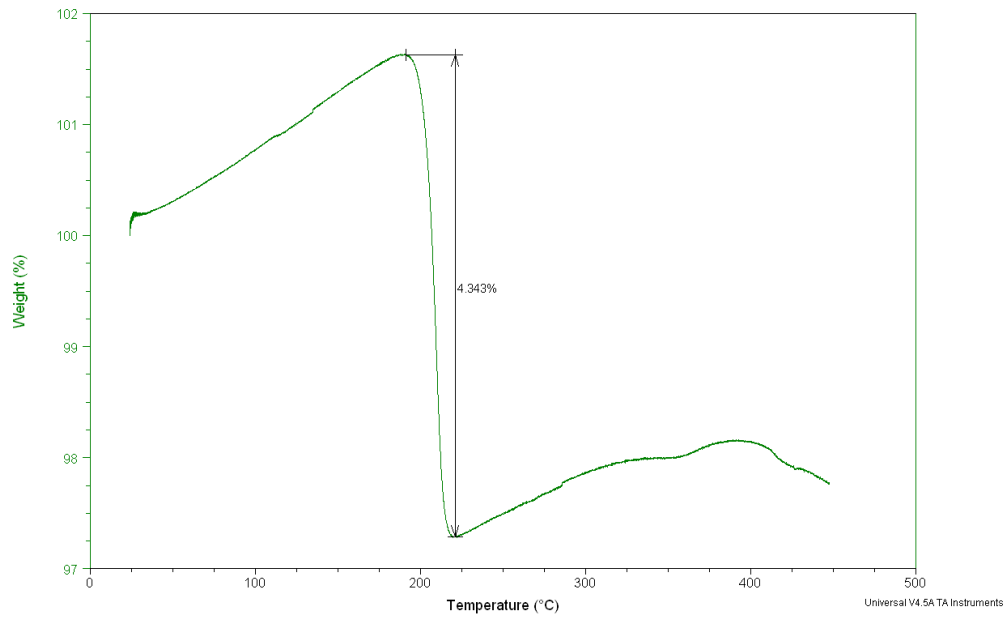


Figure 52: TGA plot of $\text{Li}_3\text{AlH}_6 + 2 \text{ mol\% Al}$

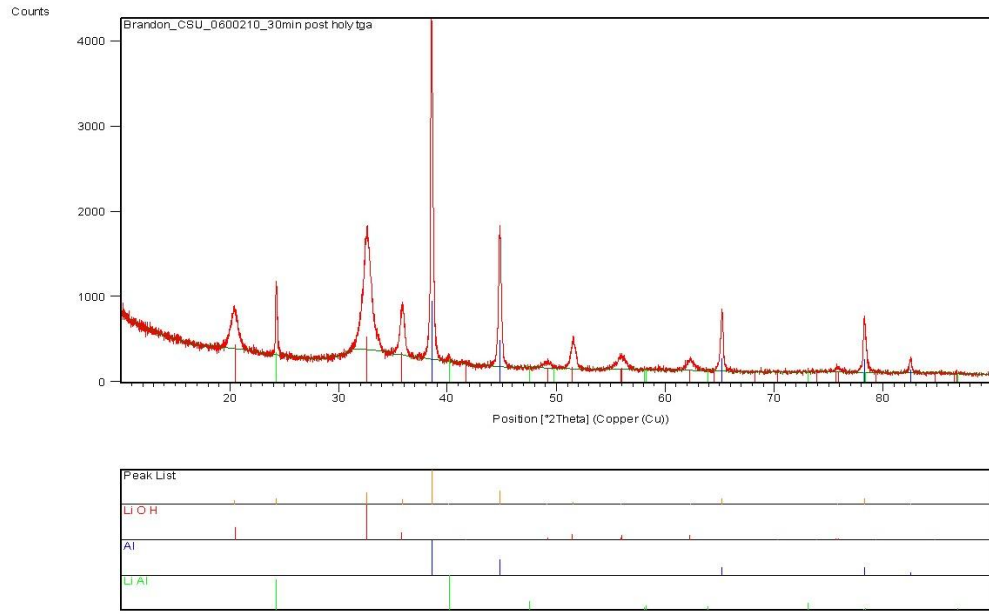


Figure 53: Post TGA XRD pattern of $\text{Li}_3\text{AlH}_6 + 2 \text{ mol\% Al}$

Li₃AlH₆ + 2 mol% AlCl₃ 0500310

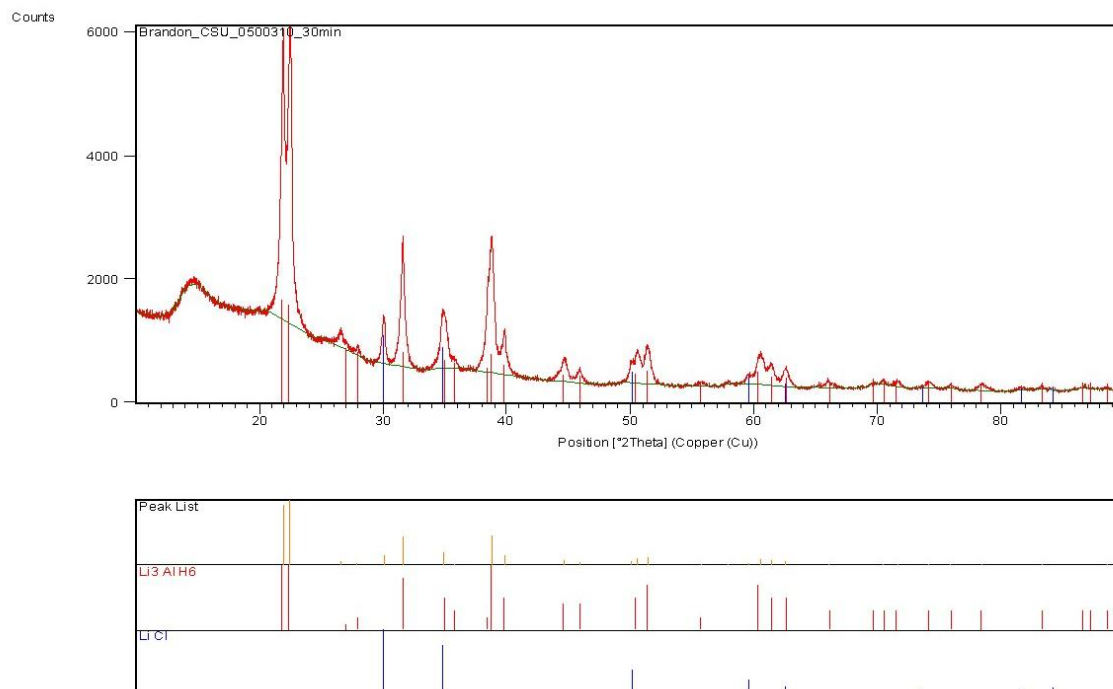


Figure 54: XRD pattern of Li₃AlH₆ + 2 mol% AlCl₃

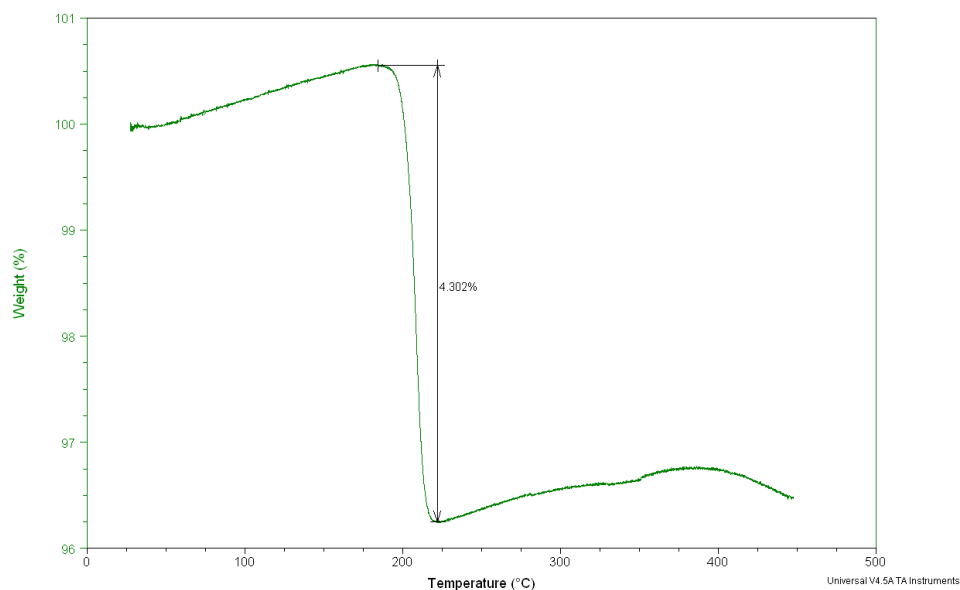


Figure 55: TGA plot of Li₃AlH₆ + 2 mol% AlCl₃

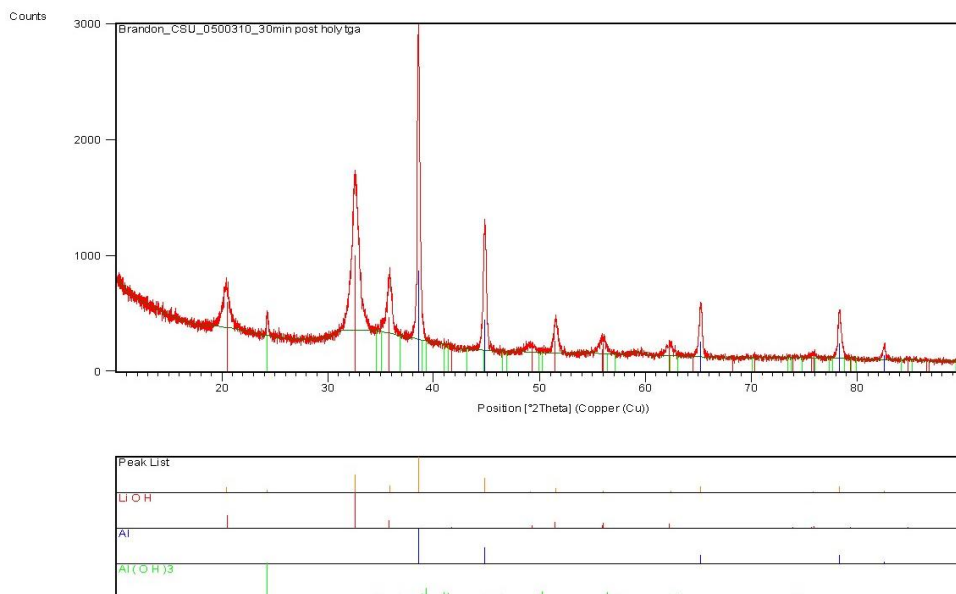


Figure 56: Post TGA XRD pattern of $\text{Li}_3\text{AlH}_6 + 2 \text{ mol\% AlCl}_3$

$\text{Li}_3\text{AlH}_6 + 2 \text{ mol\% AgCl}$ 0500210

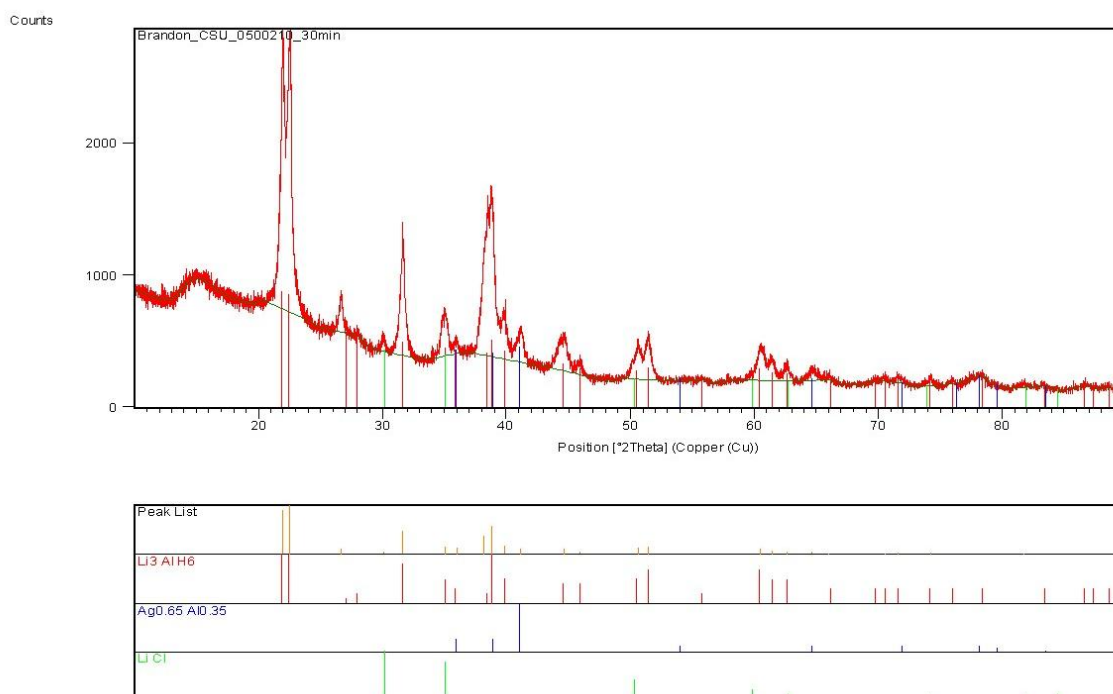


Figure 57: XRD pattern of $\text{Li}_3\text{AlH}_6 + 2 \text{ mol\% AgCl}$

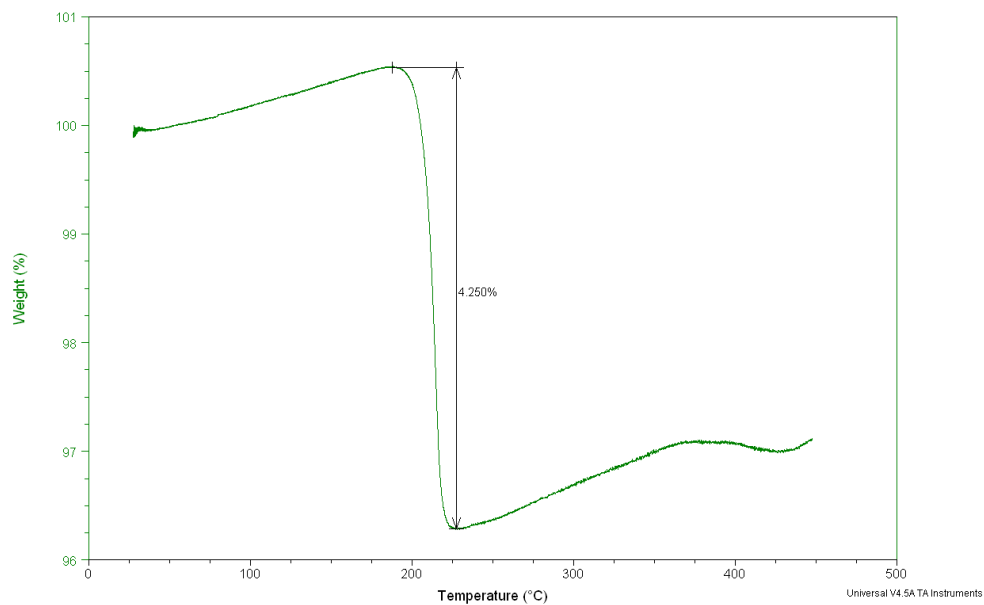


Figure 58: TGA plot of $\text{Li}_3\text{AlH}_6 + 2 \text{ mol\% AgCl}$

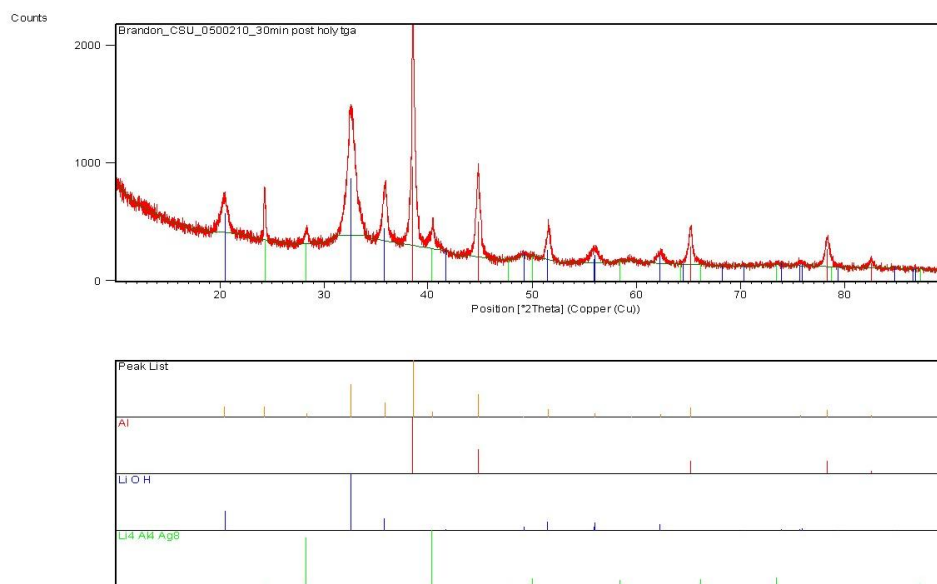


Figure 59: Post TGA XRD pattern of $\text{Li}_3\text{AlH}_6 + 2 \text{ mol\% AgCl}$

Li₃AlH₆ + 2 mol% Zn 0600310

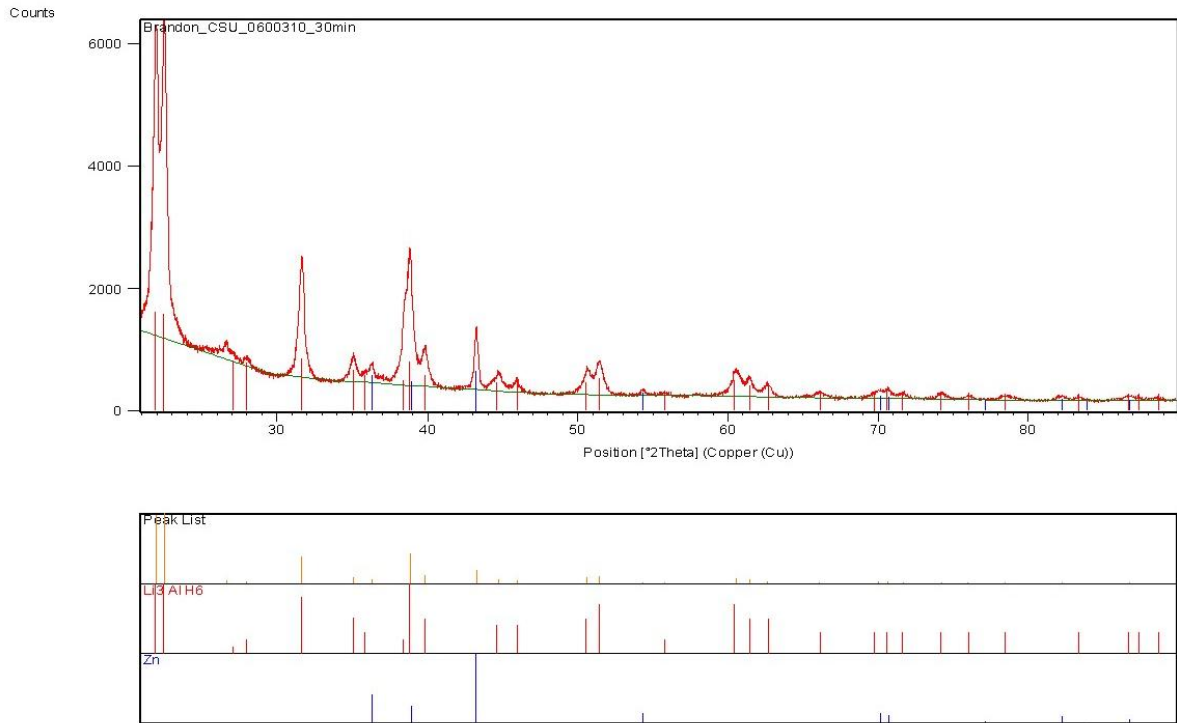


Figure 60: XRD pattern of Li₃AlH₆ + 2 mol% Zn

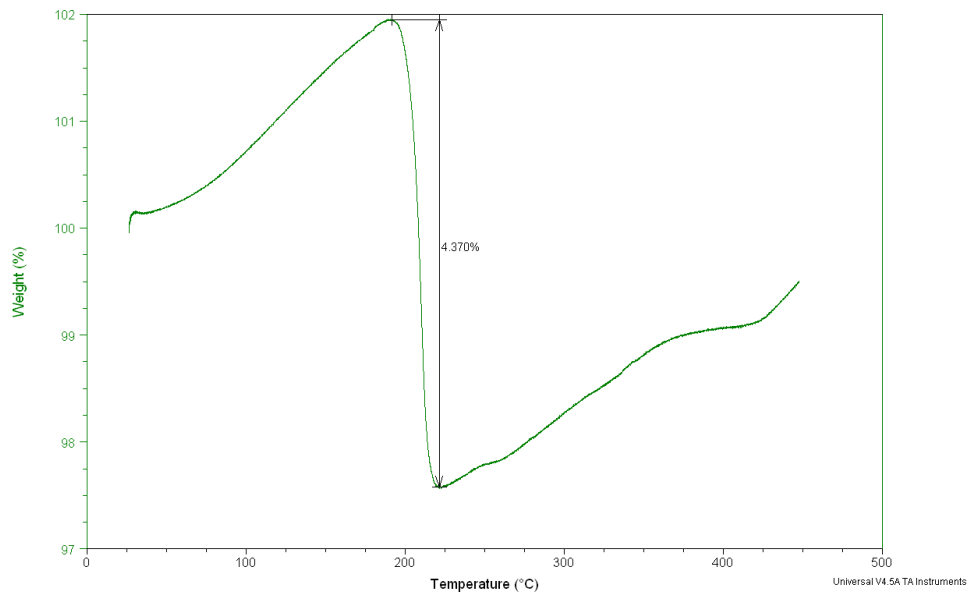


Figure 61: TGA plot of Li₃AlH₆ + 2 mol% Zn

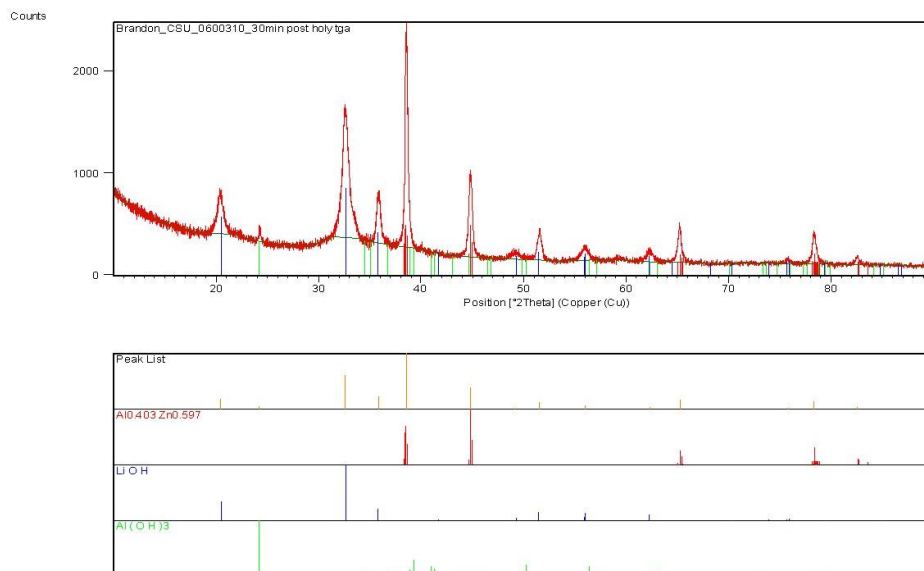


Figure 62: Post TGA XRD pattern of $\text{Li}_3\text{AlH}_6 + 2 \text{ mol\% Zn}$

$\text{Li}_3\text{AlH}_6 + 2 \text{ mol\% ZnCl}_2$ 0600510

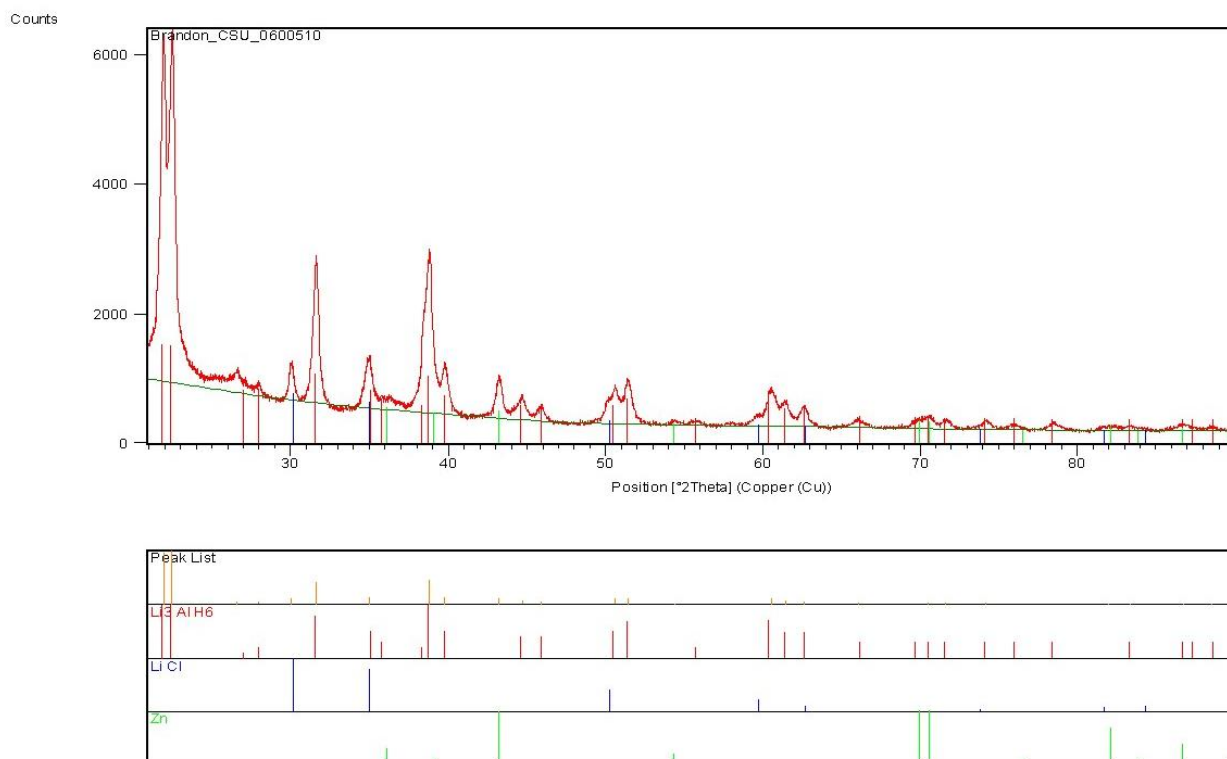


Figure 63: XRD pattern of $\text{Li}_3\text{AlH}_6 + 2 \text{ mol\% ZnCl}_2$

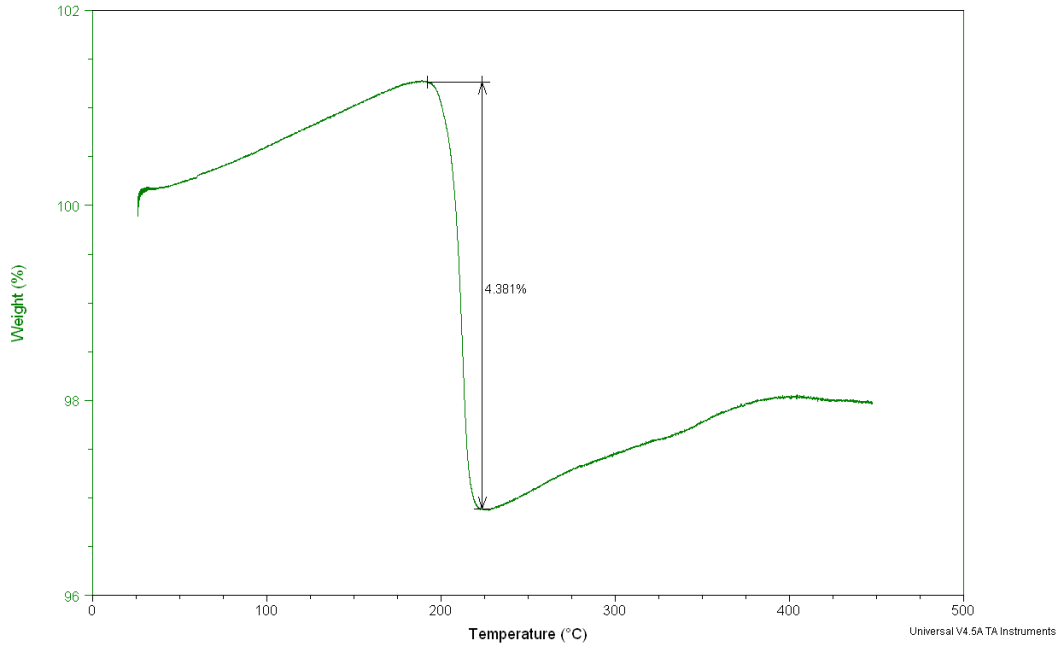


Figure 64: TGA plot of $\text{Li}_3\text{AlH}_6 + 2 \text{ mol\% ZnCl}_2$

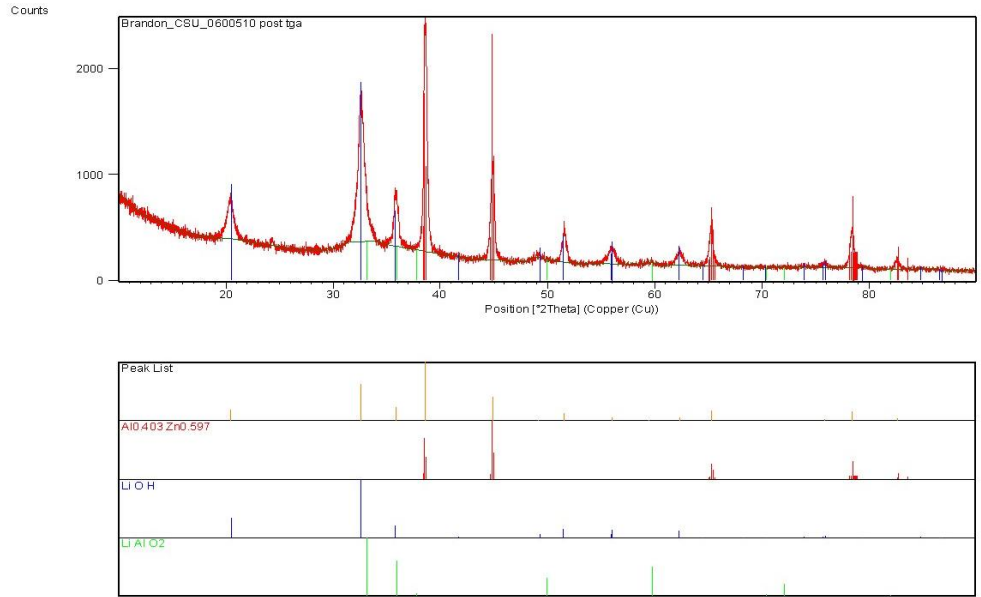


Figure 65: Post TGA XRD plot of $\text{Li}_3\text{AlH}_6 + 2 \text{ mol\% ZnCl}_2$

Li₃AlH₆ + 2 mol% ZnO 0600410

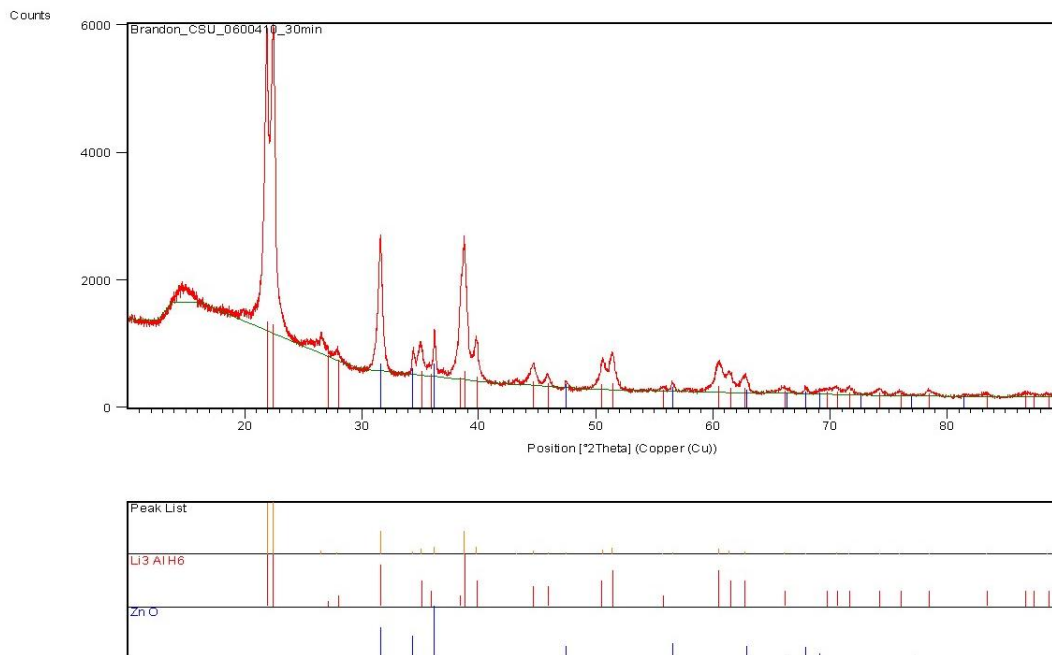


Figure 66: XRD pattern of Li₃AlH₆ + 2 mol% ZnO

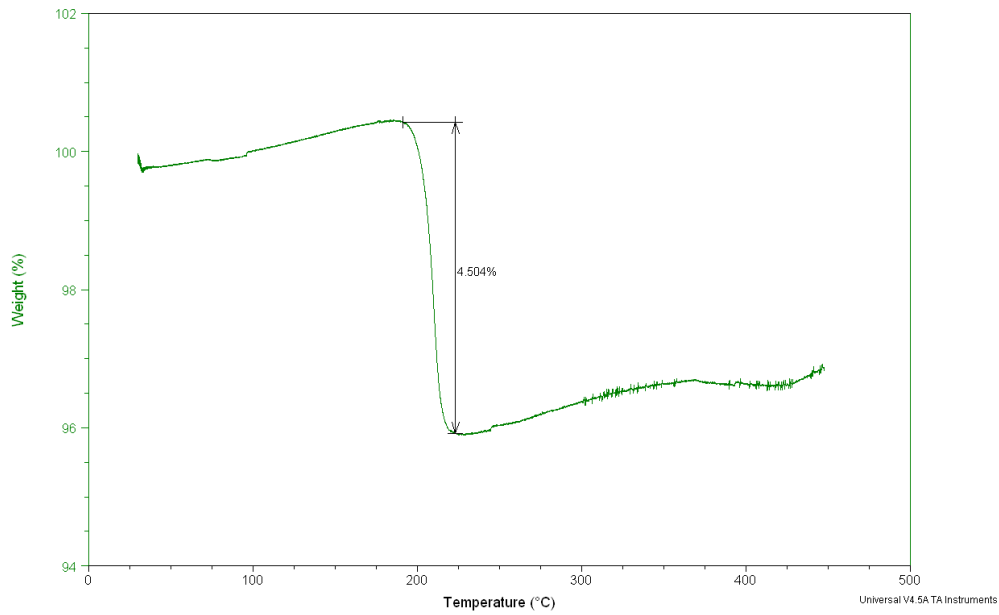


Figure 67: TGA plot of $\text{Li}_3\text{AlH}_6 + 2 \text{ mol\% ZnO}$

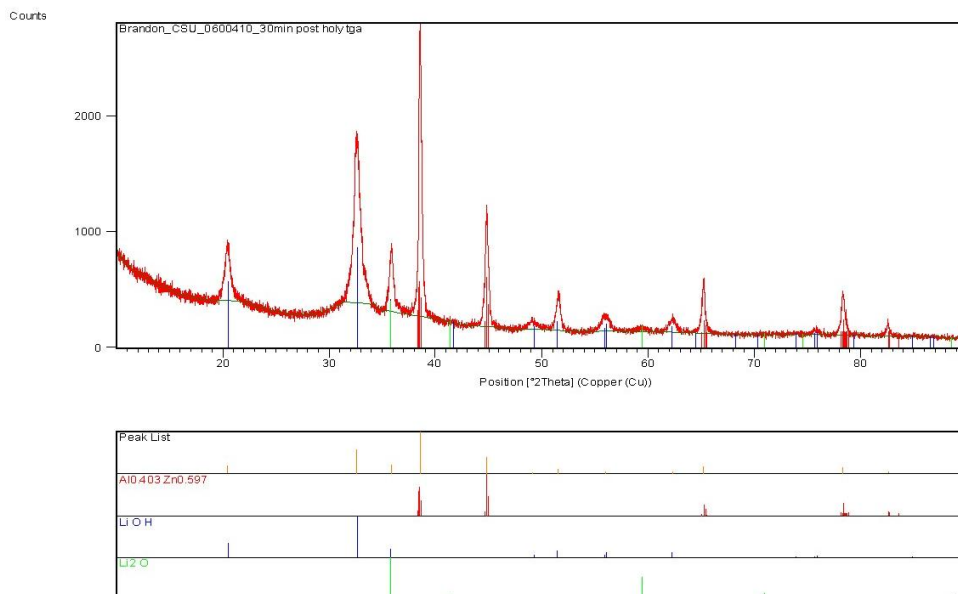


Figure 68: Post TGA XRD pattern of $\text{Li}_3\text{AlH}_6 + 2 \text{ mol\% ZnO}$

Li₃AlH₆ + 2 mol% FeCl₂ 0700510

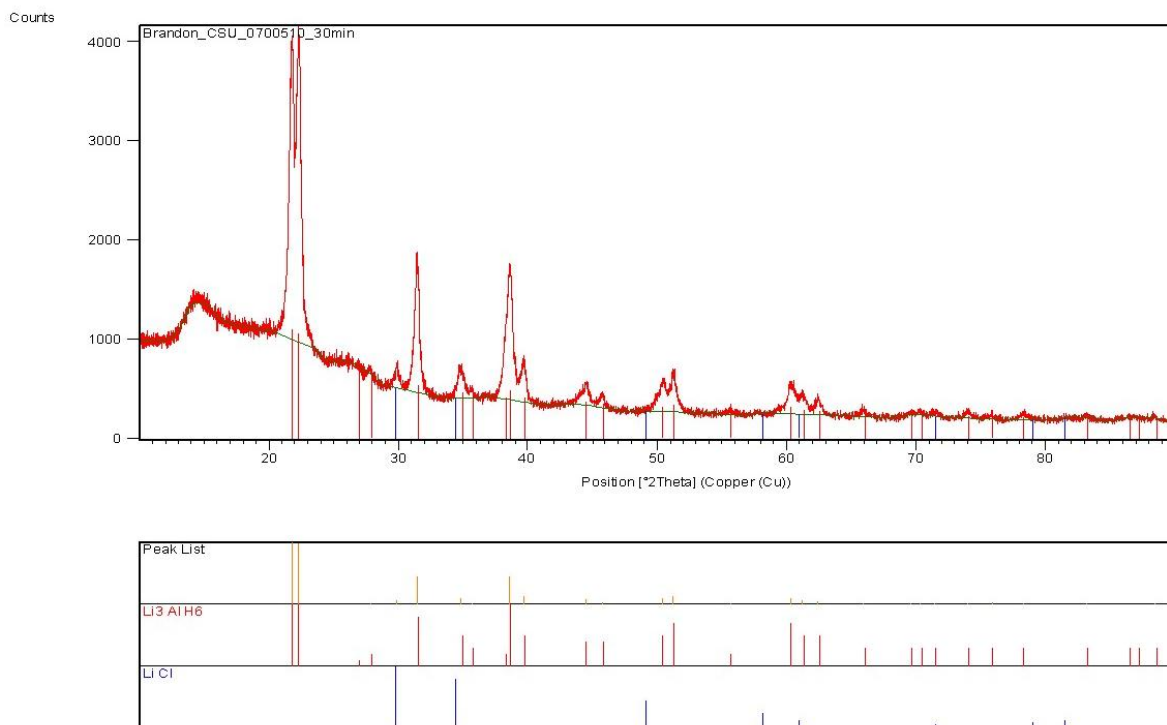


Figure 69: XRD pattern of Li₃AlH₆ + 2 mol% FeCl₂

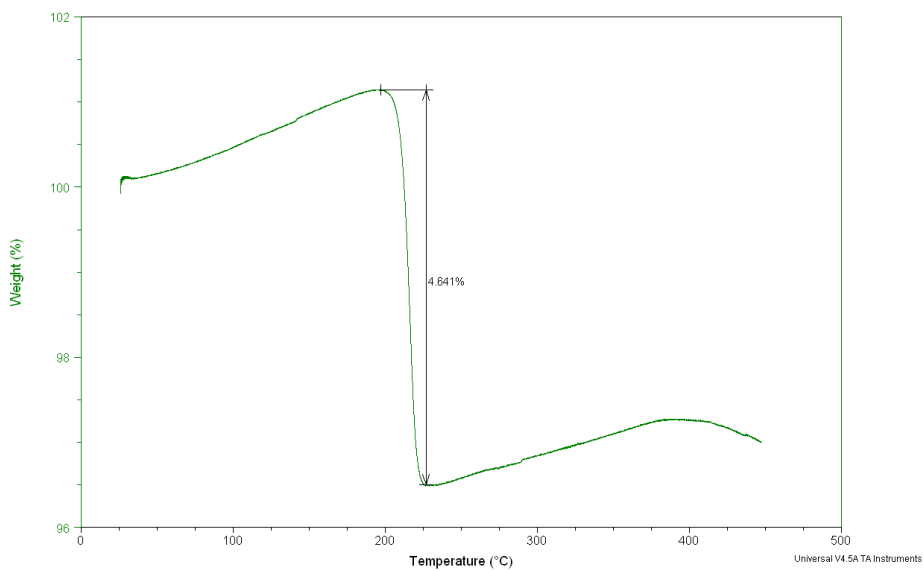


Figure 70: TGA plot of Li₃AlH₆ + 2 mol% FeCl₂

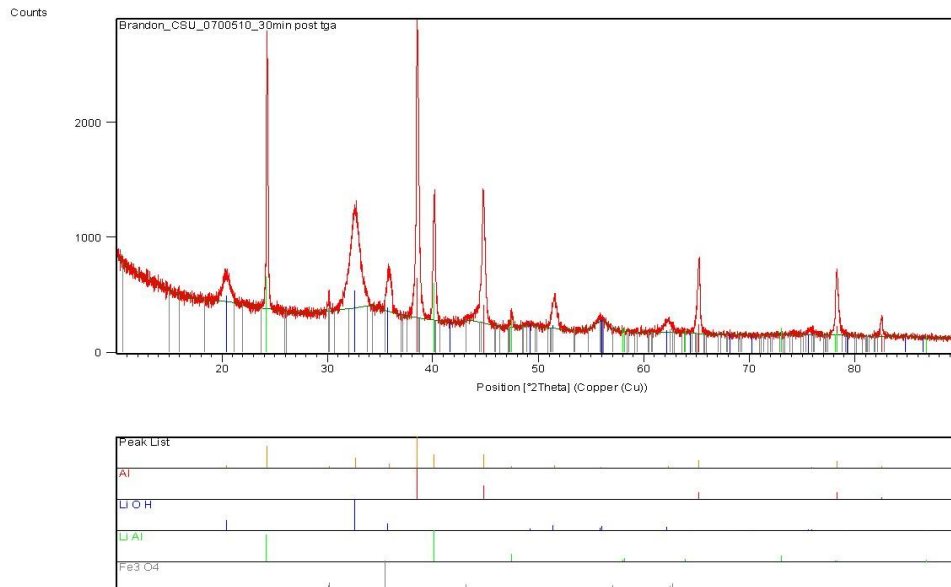


Figure 71: Post TGA XRD of $\text{Li}_3\text{AlH}_6 + 2 \text{ mol\% FeCl}_2$

$\text{Li}_3\text{AlH}_6 + 2 \text{ mol\% FeCl}_3$ 0700610

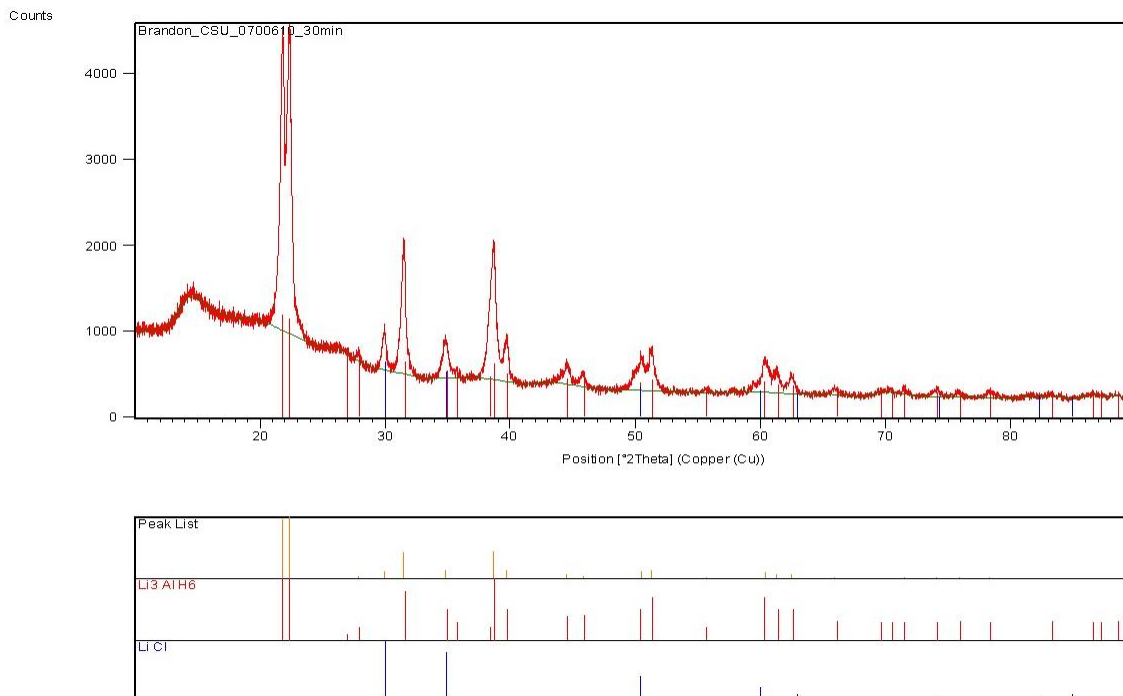


Figure 72: $\text{Li}_3\text{AlH}_6 + 2 \text{ mol\% FeCl}_3$

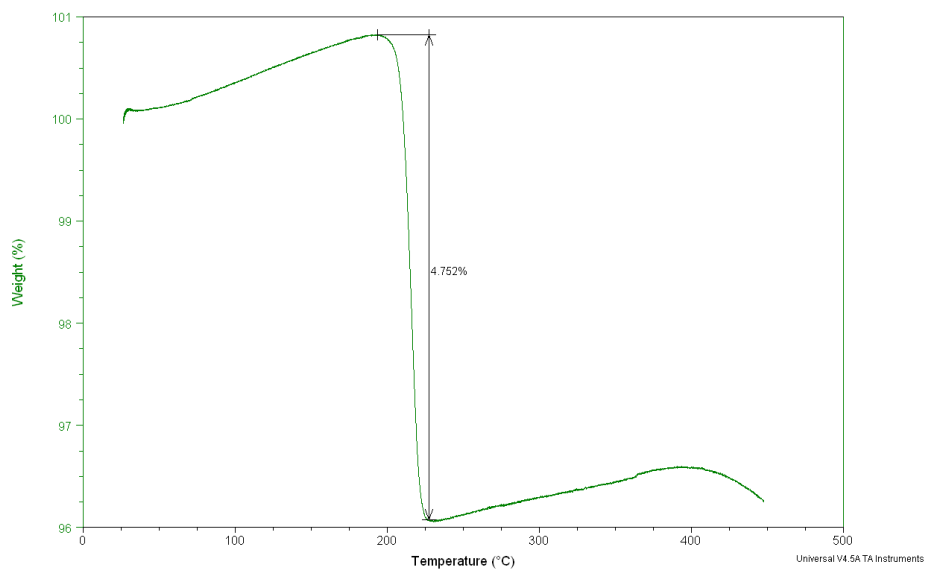


Figure 73: TGA plot of $\text{Li}_3\text{AlH}_6 + 2 \text{ mol\% FeCl}_3$

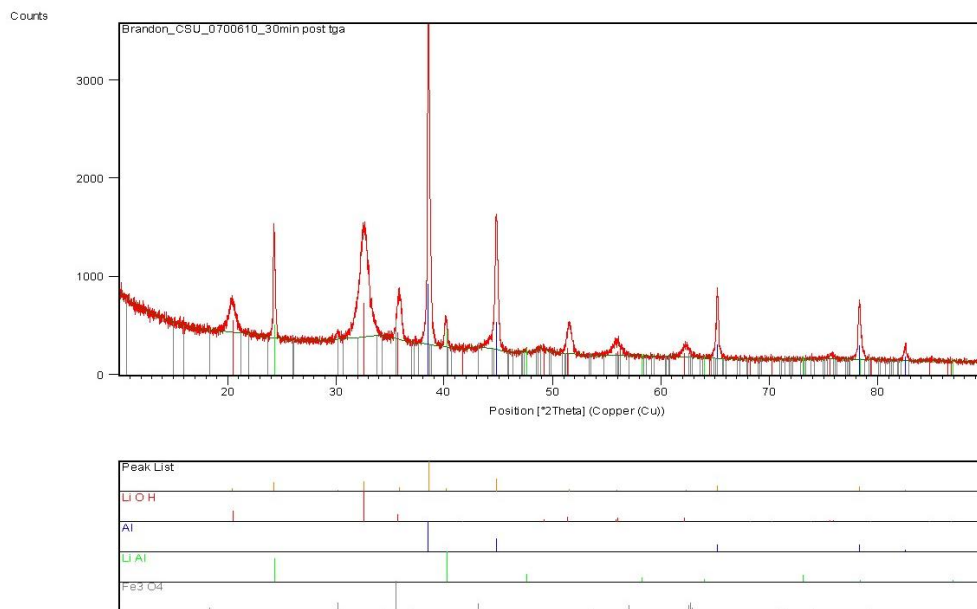


Figure 74: Post TGA XRD pattern of $\text{Li}_3\text{AlH}_6 + 2 \text{ mol\% FeCl}_3$

Li₃AlH₆ +2 mol% LaCl₃ 0600910

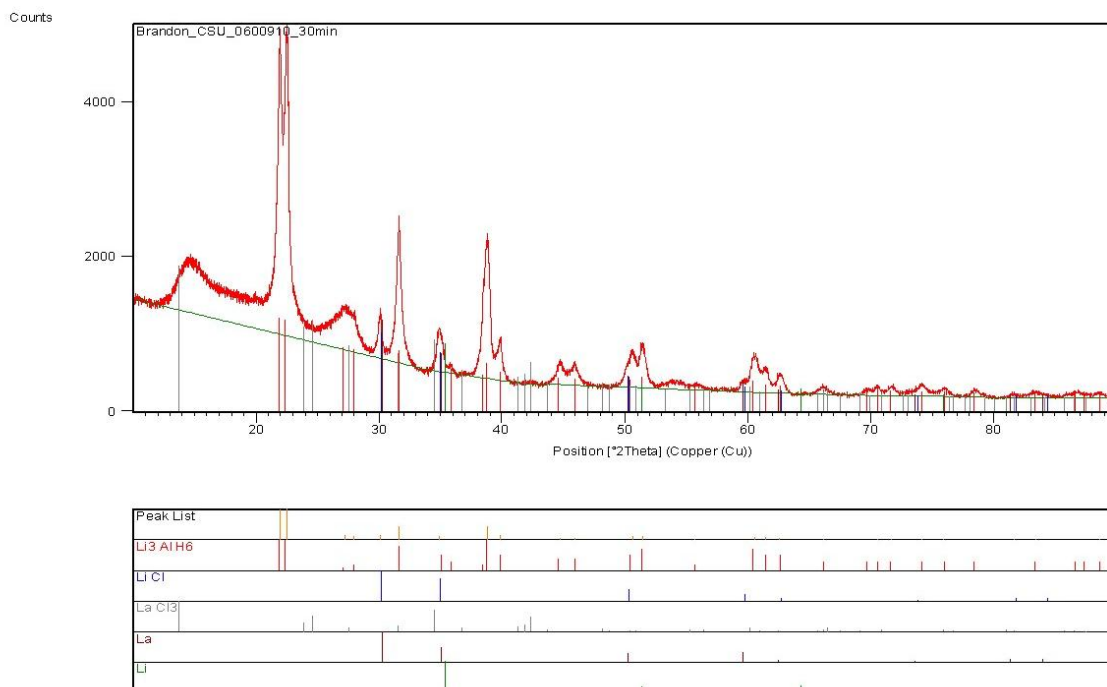


Figure 75: XRD pattern of Li₃AlH₆ +2 mol% LaCl₃

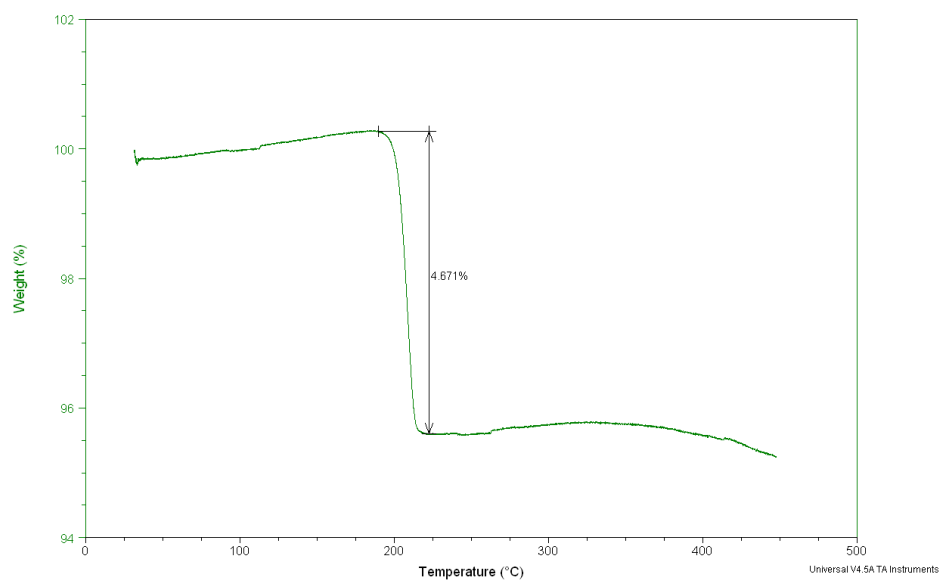


Figure 76: TGA plot of Li₃AlH₆ +2 mol% LaCl₃

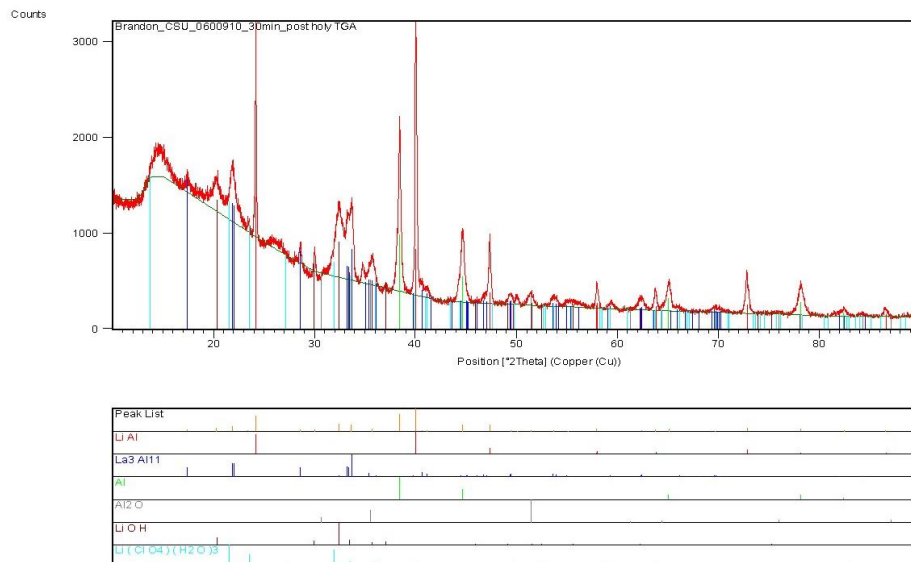


Figure 77: Post TGA XRD pattern of $\text{Li}_3\text{AlH}_6 + 2 \text{ mol}\% \text{ LaCl}_3$

$\text{Li}_3\text{AlH}_6 + 2 \text{ mol}\% \text{ CeCl}_3$ 0601010

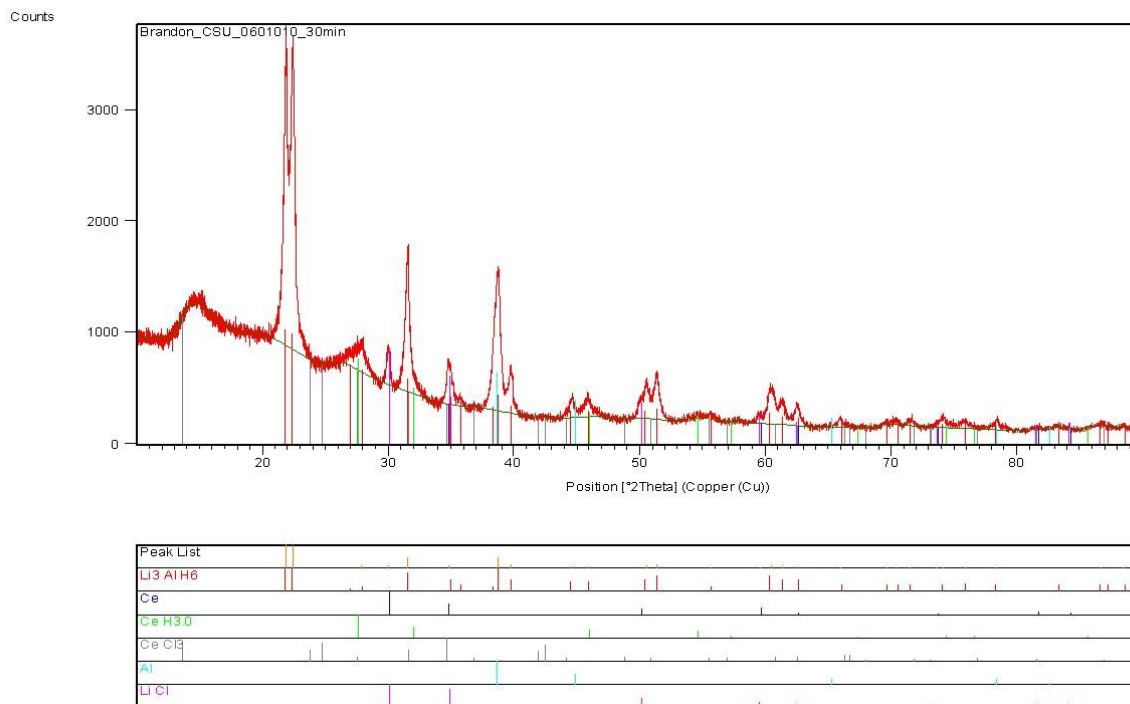


Figure 78: XRD pattern of $\text{Li}_3\text{AlH}_6 + 2 \text{ mol}\% \text{ CeCl}_3$

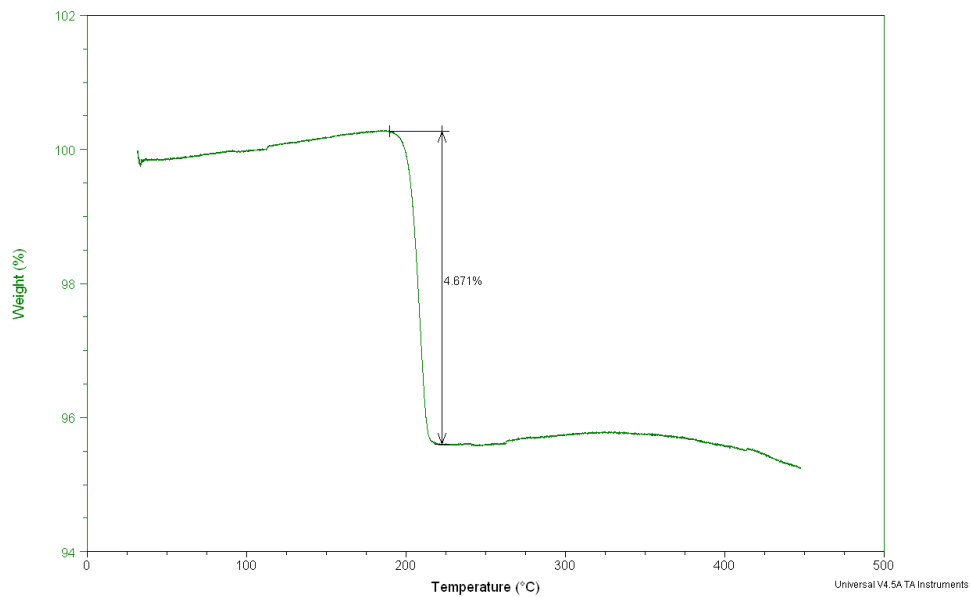


Figure 79: TGA plot of $\text{Li}_3\text{AlH}_6 + 2 \text{ mol\% CeCl}_3$

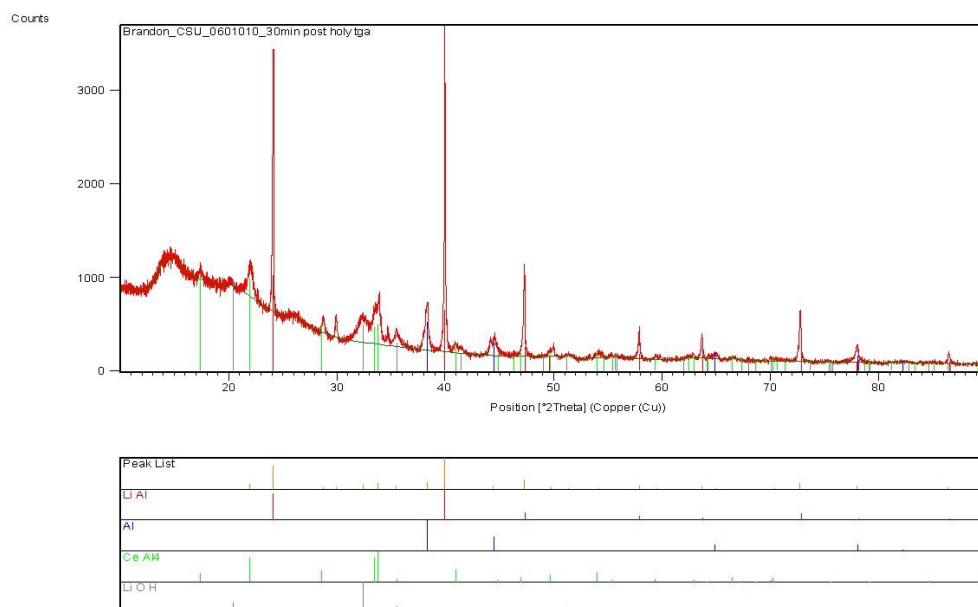


Figure 80: Post TGA XRD pattern of $\text{Li}_3\text{AlH}_6 + 2 \text{ mol\% CeCl}_3$

Li₃AlH₆ + 2 mol% PrCl₃ 0700210

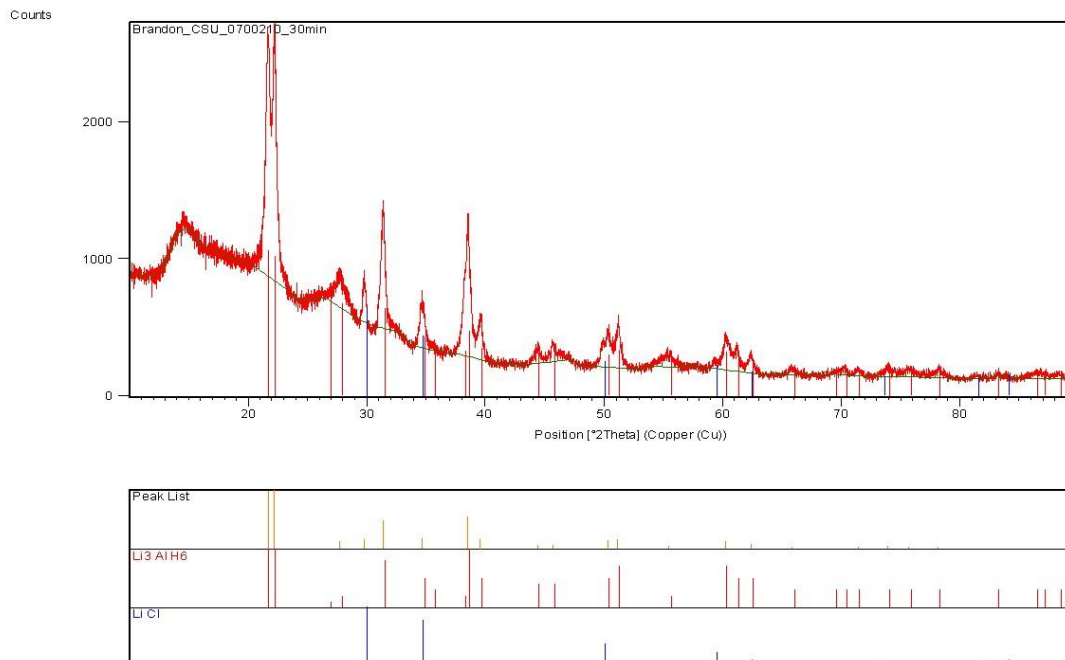


Figure 81: XRD pattern of Li₃AlH₆ + 2 mol% PrCl₃

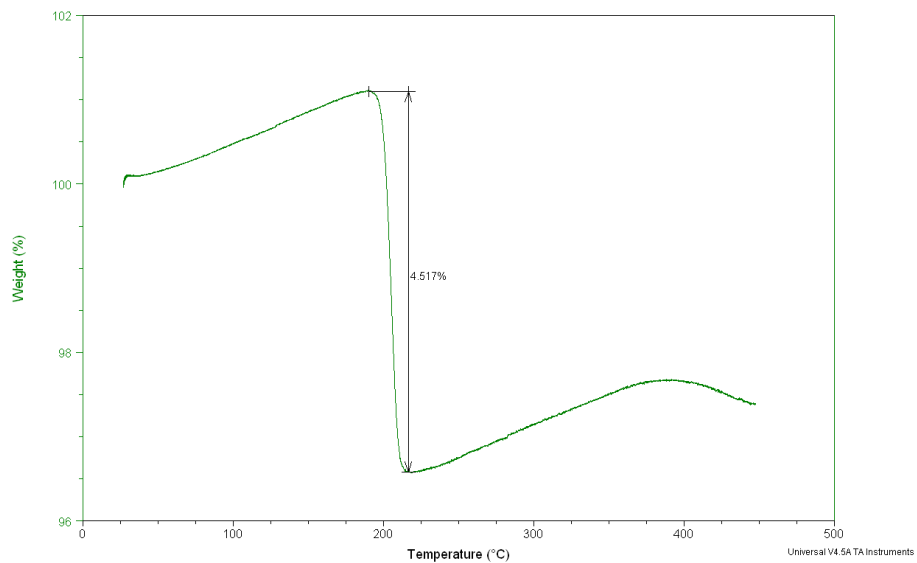


Figure 82: TGA plot of Li₃AlH₆ + 2 mol% PrCl₃

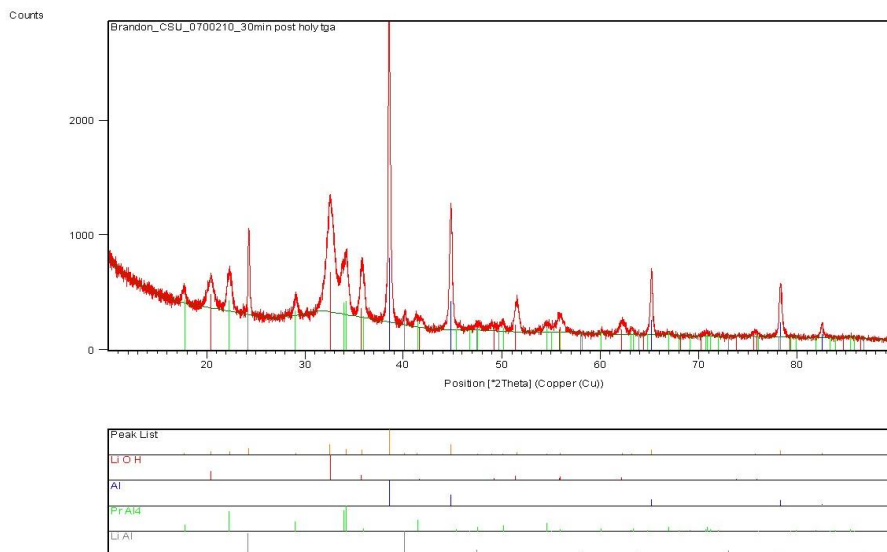


Figure 83: Post TGA XRD pattern of $\text{Li}_3\text{AlH}_6 + 2 \text{ mol\% PrCl}_3$

$\text{Li}_3\text{AlH}_6 + 2 \text{ mol\% NdCl}_3$ 0700410

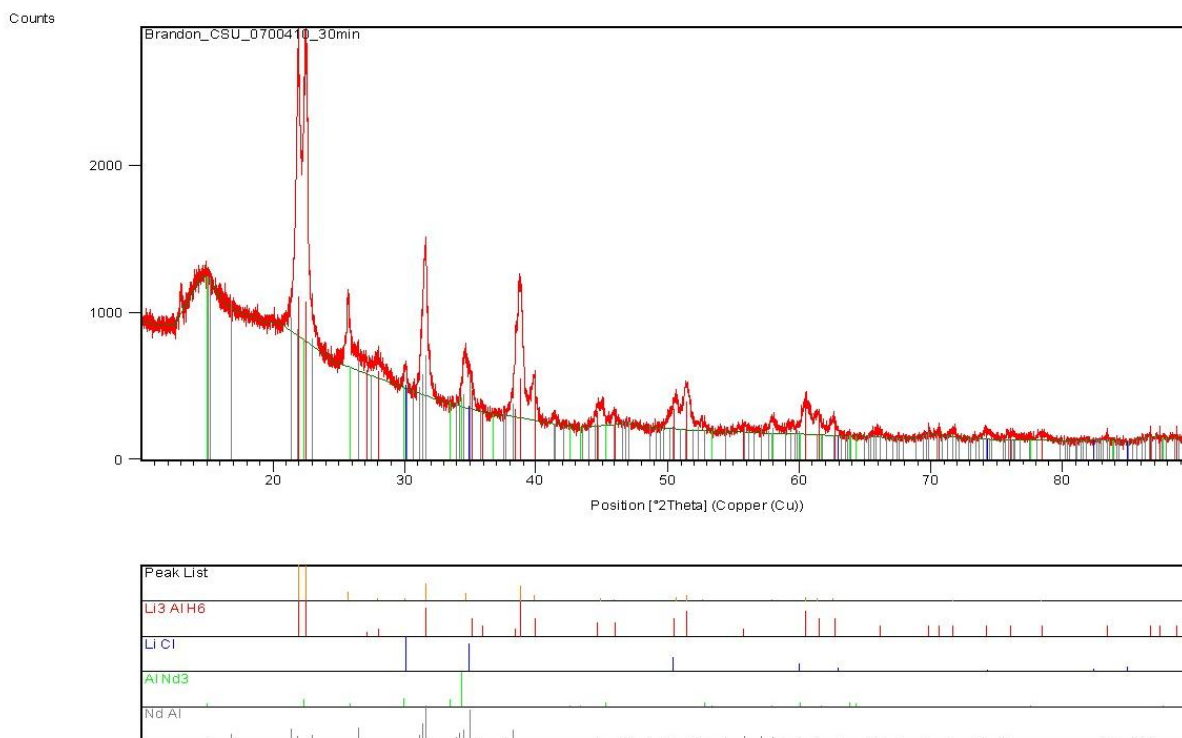


Figure 84: XRD pattern of $\text{Li}_3\text{AlH}_6 + 2 \text{ mol\% NdCl}_3$

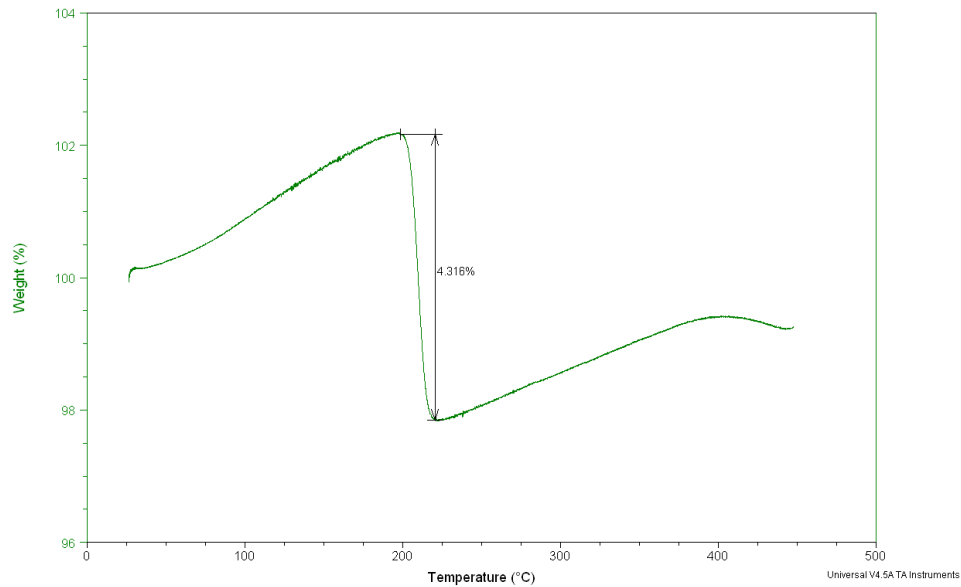


Figure 85: TGA plot of $\text{Li}_3\text{AlH}_6 + 2 \text{ mol\% NdCl}_3$

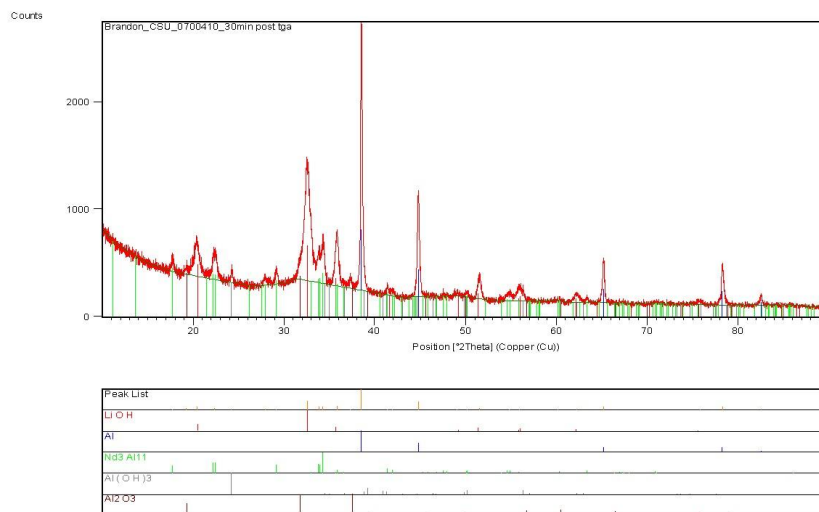


Figure 86: Post TGA XRD pattern of $\text{Li}_3\text{AlH}_6 + 2 \text{ mol\% NdCl}_3$

Li₃AlH₆ + 2 mol% YCl₃ 0700110

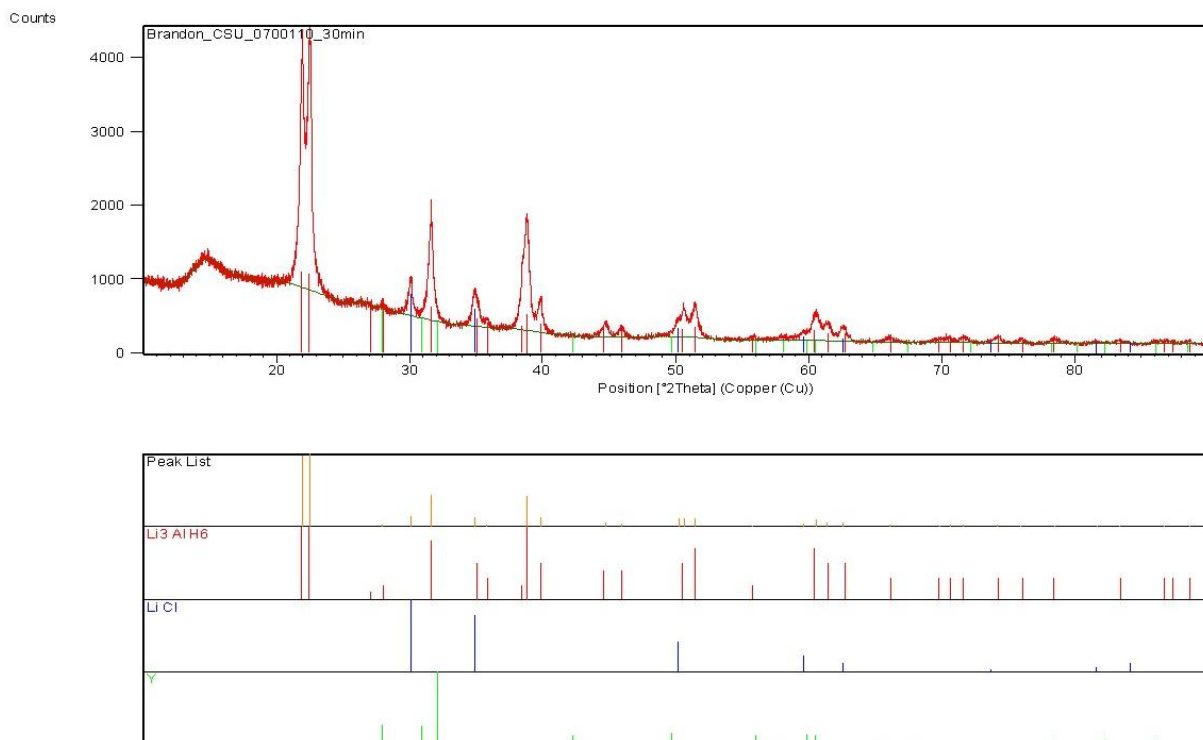


Figure 87: XRD pattern of Li₃AlH₆ + 2 mol% YCl₃

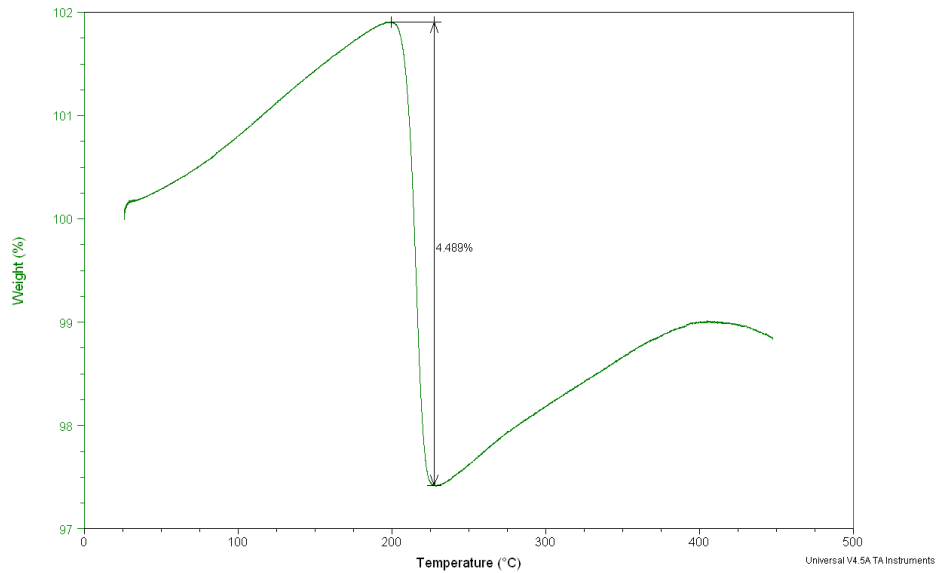


Figure 88: TGA plot of $\text{Li}_3\text{AlH}_6 + 2 \text{ mol\% YCl}_3$

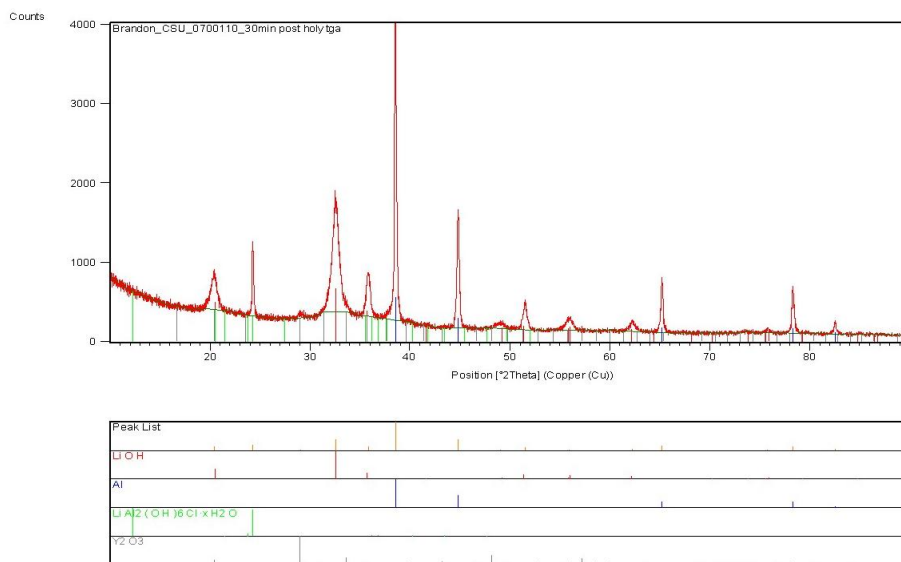


Figure 89: Post TGA XRD of $\text{Li}_3\text{AlH}_6 + 2 \text{ mol\% YCl}_3$

LiNa₂AlH₆ 0600710

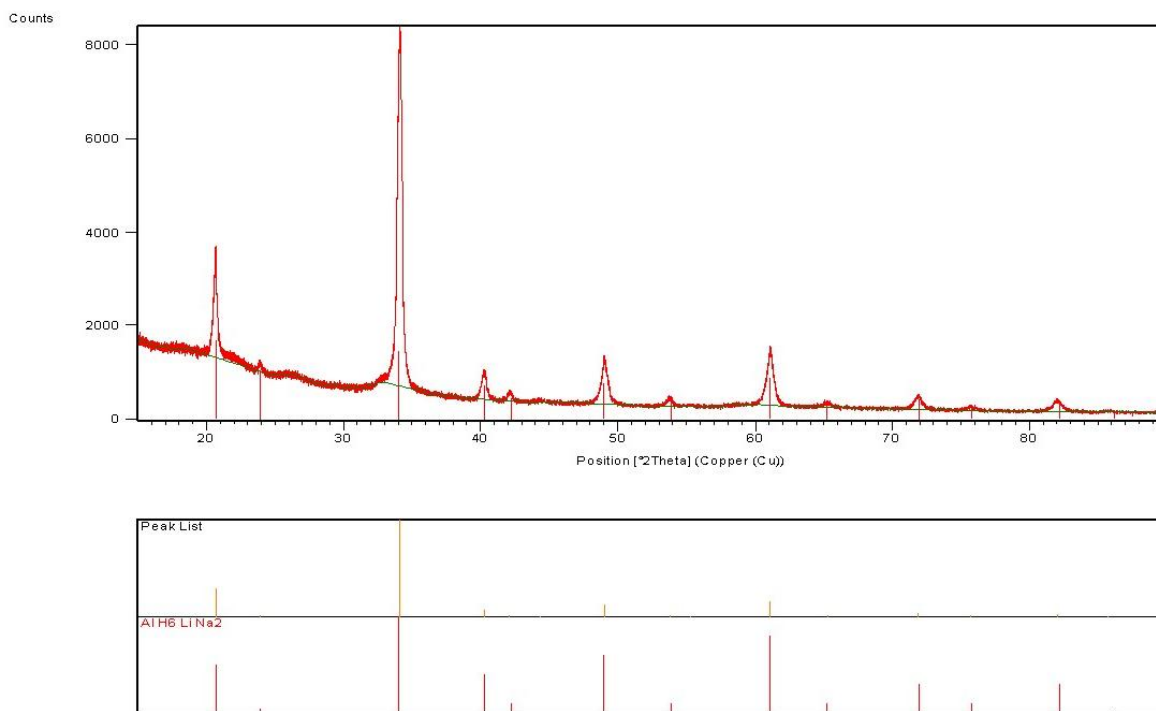


Figure 90: XRD pattern of LiNa₂AlH₆

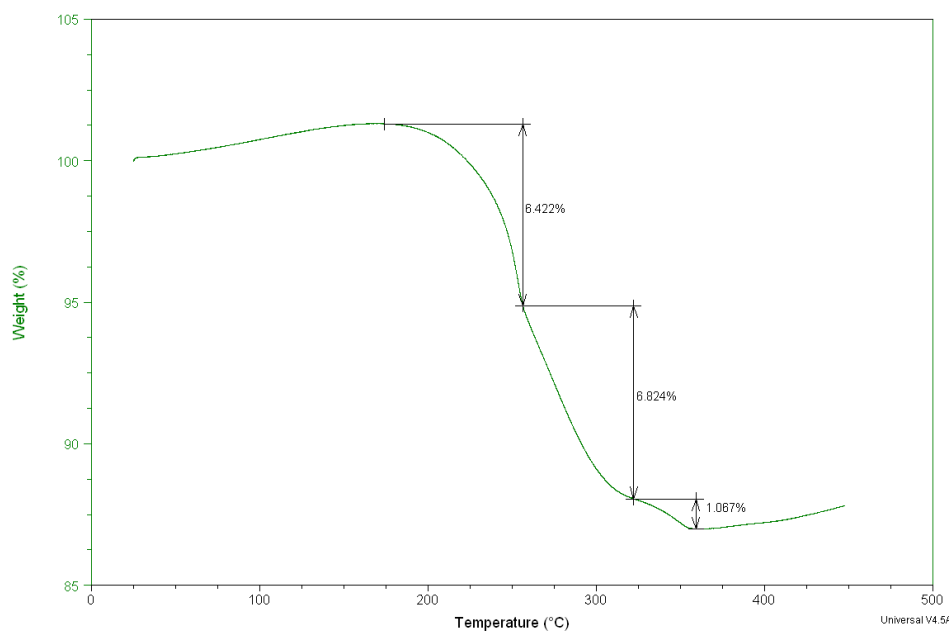


Figure 91: TGA plot of LiNa₂AlH₆